

INFORMATION TO USERS

This manuscript has been reproduced from the microfilm master. UMI films the text directly from the original or copy submitted. Thus, some thesis and dissertation copies are in typewriter face, while others may be from any type of computer printer.

The quality of this reproduction is dependent upon the quality of the copy submitted. Broken or indistinct print, colored or poor quality illustrations and photographs, print bleedthrough, substandard margins, and improper alignment can adversely affect reproduction.

In the unlikely event that the author did not send UMI a complete manuscript and there are missing pages, these will be noted. Also, if unauthorized copyright material had to be removed, a note will indicate the deletion.

Oversize materials (e.g., maps, drawings, charts) are reproduced by sectioning the original, beginning at the upper left-hand corner and continuing from left to right in equal sections with small overlaps. Each original is also photographed in one exposure and is included in reduced form at the back of the book.

Photographs included in the original manuscript have been reproduced xerographically in this copy. Higher quality 6" x 9" black and white photographic prints are available for any photographs or illustrations appearing in this copy for an additional charge. Contact UMI directly to order.

UMI

**A Bell & Howell Information Company
300 North Zeeb Road, Ann Arbor, MI 48106-1346 USA
313/761-4700 800/521-0600**



Order Number 1360247

**Applying information gathering power to the design of a field
lens for a high resolution fiber-fed astronomical spectrograph**

Vaughnn, David, M.S.

The University of Arizona, 1994

Copyright ©1994 by Vaughnn, David. All rights reserved.

U·M·I

**300 N. Zeeb Rd.
Ann Arbor, MI 48106**



**APPLYING INFORMATION GATHERING POWER TO THE DESIGN OF A FIELD LENS
FOR A HIGH RESOLUTION FIBER-FED ASTRONOMICAL SPECTROGRAPH**

David Vaughn

© David Vaughn 1994

**A Thesis Submitted to the Faculty of the
COMMITTEE ON OPTICAL SCIENCES (GRADUATE)**

**In Partial Fulfillment of the Requirements
For the Degree of**

**MASTER OF SCIENCE
In the Graduate College**

THE UNIVERSITY OF ARIZONA

1994

STATEMENT BY AUTHOR

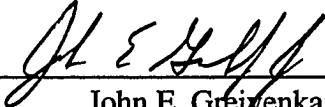
This thesis has been submitted in partial fulfillment of requirements for an advanced degree at the University of Arizona and is deposited in the University Library to be made available to borrowers under rules of the Library.

Brief quotations from this thesis are allowable without special permission, provided that accurate acknowledgment of source is made. Requests for permission for extended quotation from or reproduction of this manuscript in whole or in part may be granted by the copyright holder.

SIGNED:  11/19/94

APPROVAL BY THESIS DIRECTOR

This thesis has been approved on the date shown below:



John E. Greivenkamp
Professor of Optical Sciences

11/21/94

Date

ACKNOWLEDGMENT

This work was done under the auspices of the National Optical Astronomy Observatories (NOAO), unto which the author is indebted for its support. NOAO is operated by the Association of Universities for Research in Astronomy, Inc. (AURA) under cooperative agreement with the National Science Foundation.

Appreciation is extended to all of my fellow workers who have shared in the vision of providing world class instrumentation to the greater scientific community. Special note is made to G. Muller who prepared the line drawing figures, T. Armandroff and S. Barden for their scientific guidance, and R. Reed and L. Daggert for their unwavering faith in me.

This work could not have been accomplished without the love and encouragement of my wife, Lisa, our friends the Albertsons, Davidsons, Grimes, and Turchettos, and the spiritual support of our local church, the Bible Chapel.

DEDICATION

This work is dedicated to the self-existent creator of the universe.

Πίστει νοοῦμεν κατηρτίσθαι τοὺς αἰῶνας* ῥήματι θεοῦ,
By faith we understand having been prepared the universe by a word of God,

εἰς τὸ μὴ ἐκ φαινομένων τὸ βλεπόμενον γεγονέναι.
so that not out of phenomena the things observed came into existence.

By faith we understand that the universe was prepared by an act of God,
so that which is observable did not come into existence by physical phenomena.

From the anonymous letter to the Hebrew Christians
living in the Diaspora, ca. 64-68 (Hebrews 11:3)

* Lit. "eternity" or "æons", metonymical representation of the contained for the container.

TABLE OF CONTENTS

1. LIST OF FIGURES.....	7
2. LIST OF TABLES.....	9
3. ABSTRACT.....	11
4. INTRODUCTION.....	12
5. FIGURES OF MERIT	16
5.1 BACKGROUND.....	16
5.2 PROBLEMS WITH TRADITIONAL FIGURES OF MERIT.....	20
5.3 POTENTIAL INFORMATION GATHERING POWER	22
5.3.1 Per Resolution Element.....	24
5.3.2 Application to the 2-D System.....	25
6. FORMULATION OF THE TASK	31
6.1 DESCRIPTION OF THE SPECTROGRAPH.....	31
6.1.1 Module Details.....	34
6.1.2 Grating/Diffraction Principles	39
6.1.3 The High Resolution Mode.....	43
6.2 THE PROBLEM.....	45
6.2.1 Possible Solutions	52
6.2.2 Summary of “Free” Variables.....	54
6.3 THE TASK.....	55
7. GRATING EFFICIENCY.....	57
7.1 THEORETICAL TREATMENT	58
7.1.1 Scalar Diffraction Theory	59
7.1.2 New Developments.....	65
7.1.3 Milton Roy Data.....	67
7.2 BENCH SPECTROGRAPH DATA	71
7.2.1 Description.....	71
7.2.2 Data Reduction.....	73
7.2.3 Polarization	81
7.2.4 Conical Diffraction	85
7.2.5 Results.....	91

TABLE OF CONTENTS - *Continued*

7.3 FITTING THE DATA.....	98
8. MODELING	103
8.1 DETERMINATION OF THE SET-UP	103
8.2 ANALYSIS.....	112
8.2.1 Effects Which are Not Modeled.....	112
8.2.2 Assembling the Relative Information Gathering Power	114
8.2.3 The Ray Trace Model	115
8.2.4 The Transmission Term	127
8.2.5 The Image Width Term.....	128
8.2.6 The Noise Term	138
8.3 OPTIMIZING.....	142
9. ANALYSIS.....	147
9.1 RESULTS.....	147
9.2 FIELD LENS MATERIAL	149
9.3 OPTIMIZING ACROSS THE ENTIRE WAVELENGTH RANGE.....	151
9.4 FINAL DESIGN	153
10. CONCLUSION	155
11. APPENDIX A, GLOSSARY OF SYMBOLS.....	157
12. APPENDIX B, AREA-WEIGHTED WIDTH	162
13. APPENDIX C, SOFTWARE MODEL OF THE SPECTROGRAPH	163
14. REFERENCES.....	171

1. LIST OF FIGURES

Figure 1, The Bench Spectrograph.....	12
Figure 2, Gaussian Widths and Resolvability	27
Figure 3, Spectrograph Layout.....	33
Figure 4, Intrinsic Warp of the CCD.....	38
Figure 5, Diffraction Geometry.....	39
Figure 6, Grating Geometry	43
Figure 7, Diffraction Orders for $\varphi_C = 11^\circ$	48
Figure 8, Diffraction Orders for $\varphi_C = 15^\circ$	49
Figure 9, Diffraction Orders for $\varphi_C = 19^\circ$	49
Figure 10, L_1 Geometry.....	50
Figure 11, $L_1(\varphi_C)$	52
Figure 12, Scalar Efficiency Map.....	63
Figure 13, Scalar Efficiency Profile.....	64
Figure 14, Average Scalar Efficiency	65
Figure 15, Processed Milton Roy Efficiency Data for $\lambda = .4416 \mu\text{m}$	69
Figure 16, Average Grating Efficiency From Milton Roy Data	70
Figure 17, Row Plot for $\varphi_C = 14^\circ$, Mid Region, s Polarization.....	74
Figure 18, Typical Flat Field Spectrum.....	75
Figure 19, Region to Region Vignetting Deviation	78
Figure 20, Red to Blue Side Vignetting Deviation	79
Figure 21, Bench Spectrograph Unpolarized Efficiency Function	81
Figure 22, Bench Spectrograph s Polarization Efficiency Trend.....	82
Figure 23, Bench Spectrograph p Polarization Efficiency Trend	83
Figure 24, Bench Spectrograph, Unpolarized Efficiency Trend.....	84

LIST OF FIGURES - *Continued*

Figure 25, Average Efficiency for Three Fields, Not Normalized.....	87
Figure 26, Average Efficiency for Three Fields, Normalized.....	88
Figure 27, Typical Numerical Fit to Vignetting Function Along y	89
Figure 28, Efficiency, Experimental Vignetting Normalization	90
Figure 29, Integrated Fiber Radiance	92
Figure 30, Fiber Modal Diffusion	93
Figure 31, Flat Field Distribution.....	95
Figure 32, Irradiance Bias as a Function of ϕ	96
Figure 33, Effect of Dispersion on Efficiency	97
Figure 34, Theoretical Models of Average Grating Efficiency	99
Figure 35, Various Numerical Fits Displayed.....	100
Figure 36, Best Estimate of Average Grating Efficiency.....	102
Figure 37, Unfolded Spatial Geometry, No Field Lens	106
Figure 38, Unfolded Spatial Geometry, With Field Lens	108
Figure 39, Modified Spatial Pupil and Chief Rays	109
Figure 40, Spatial Pupil Dependence on Vignetting.....	110
Figure 41, Image Centroids for $9 \times 9 \lambda$ Sampling	122
Figure 42, Typical $w_{\text{PSF}}(y, \lambda)$	125
Figure 43, Typical $\epsilon_v(y, \lambda)$	126
Figure 44, Model of Circular Object (Fiber) From 25^2 Grid.....	132
Figure 45, Final Design of the Field Lens.....	154
Figure 46, Area-Weighted Width	162

2. LIST OF TABLES

Table 1, Available Diffraction Gratings.....	36
Table 2, Representative Order for Scalar Theory.....	60
Table 3, Summary of Milton Roy Data.....	69
Table 4, Wavelength Regions	73
Table 5, Selected Wavelengths	76
Table 6, Typical Normalized Flux Calculation	80
Table 7, Field Position Summary	86
Table 8, Summary Data for 6 Line Plots.....	88
Table 9, Data Set of Camera-Collimator Angles	95
Table 10, Various Numerical Fits For Average Grating Efficiency	100
Table 11, Determination of Best Estimate of Grating Efficiency	102
Table 12, Configuration Summary with Wavelengths	104
Table 13, Vignetting Summary for Original Configuration ($\varphi_C = 11^\circ$)	107
Table 14, Melt Fitting Summary	118
Table 15, Fictitious Sellmeier Coefficients for Vacuum.....	120
Table 17, \pm Field Comparison, w_{PSF}	124
Table 16, \pm Field Comparison, ε_V	124
Table 18, Validation of the Model for w_{IMG}	133
Table 19, Validation of the Model for w_{PIX}	134
Table 20, Summary of Diffraction Effects.....	138
Table 21, Summary of Free Parameters	144
Table 22, Summary of Field Lens Parameters	145
Table 23, Summary of \mathcal{P}_{REL}	147
Table 24, Comparison of Field Lens Material	150

LIST OF TABLES - *Continued*

Table 25, Three Wavelength Regions	152
Table 26, Free Parameters for Each Region.....	152
Table 27, Final Design Free Parameters and \mathcal{P}_{REL}	153

3. ABSTRACT

A new figure of merit, the potential information gathering power, \mathcal{P} , is developed for use in evaluating the performance of spectrographs. It is based on the premise that it is desirable to maximize the product of the SNR at each resolution element in the reduced data by the number of resolution elements. Because of this general intent, it places no *a priori* emphasis on any particular scientific use. This figure is then applied to the task of improving the performance of a real fiber-fed astronomical spectrograph when it is operated in its high-resolution mode. It is shown that the optimum configuration corresponds to adding a new field lens, changing the focal length and size of the collimator, and arranging the camera and collimator axes to the narrowest allowable geometry. An approximate gain of between 15% to 18% may be realized.

4. INTRODUCTION

The subject of this thesis, improvement of a fiber-fed astronomical spectrograph, is an on going project at the National Optical Astronomy Observatories (NOAO). The instrument is currently being implemented at a new 3.5 m telescope, the WIYN, on Kitt Peak and is known simply as the Bench Spectrograph¹. This reflects that rather than being mounted directly to one of the telescope ports, it is located on a stable isolated optical bench some distance away and fed via a fiber optical cable from one of the telescope's Nasmyth ports^{*2}.

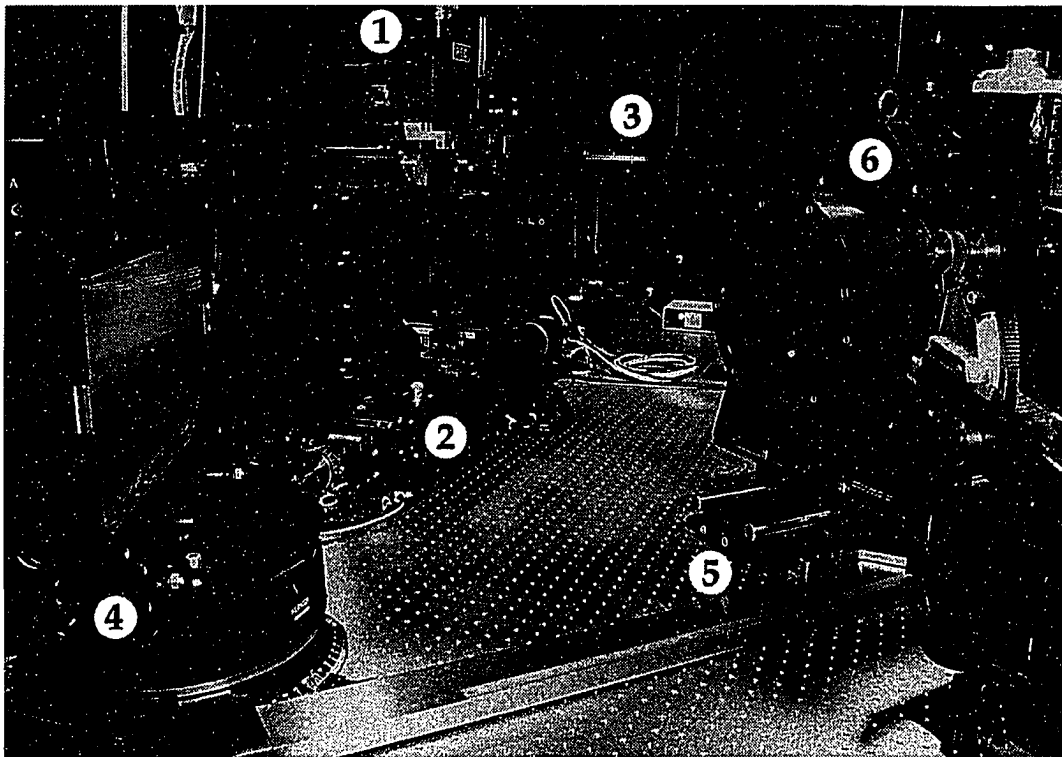


Figure 1, The Bench Spectrograph

* A Nasmyth port is a Cassegrain or modified Cassegrain focus folded 90° out the center of an altitude journal bearing.

In Figure 1, the principal modules which constitute the spectrograph are identified numerically:

1. The fiber optic cable coming from the telescope enters the spectrograph environment from above.
2. A Fiber Module accepts the fiber array, provides post “slit” optics and a focusing mechanism, and directs the light toward the collimator.
3. The reflective collimator forms a set of beams which propagate back through the fiber array toward the grating.
4. The Grating Mount (shown here with the Echelle^{*}) provides an accurate mechanism for housing and rotating diffraction gratings.
5. The Camera-Axis Mount provides a stable platform to hold the camera objective and detector assembly. It has manual adjustments for translating along the camera axis and for setting the included angle from the collimator axis.
6. The current Simmons Camera objective is shown. A dewar with a CCD array detector is behind the objective.

The Bench Spectrograph is a general purpose multi-object spectrograph. As such, it is intended to be utilized for a wide range of astronomical applications where it

^{*} An Echelle grating, or simply Echelle, is a grating designed to operate at large angles of incidence (see Section 6.1.3).

is desirable to record spectra simultaneously from multiple sources over the relatively large corrected field of view of the telescope (apx. 1°). In order to meet the demands of being a general purpose instrument, it must offer a wide range of available dispersions (or wavelength resolutions) over the entire extended visible wavelength region. This is roughly defined as going from atmospheric “cut-off” at approximately $.350 \mu\text{m}$ in the “blue”^{*} out to $1.0 \mu\text{m}$ in the “red”, where the sensitivity of currently available visible CCD detector arrays (hereafter referred to simply as CCDs or detectors) drops off.

This thesis considers the challenge of improving the performance of a high resolution mode. The high resolution mode utilizes an Echelle grating to achieve sub-Ångstrom resolutions. In this configuration, the angle between the camera and collimator axes, φ_c , is set to a very narrow value ($\varphi_c \gtrsim 11^\circ$). The camera objective must be far removed from the grating to prevent interference between the collimator and camera beams. This is an inefficient geometry which “throws away” about half the light. The performance can be improved by designing a new optical sub-module, a field lens, which can be inserted into the spectrograph optical system, changing parameters of the collimator, and selecting the optimum camera-collimator angle, φ_c .

However, before one can improve the performance, a quantitative description of performance must be made. As it turns out, this is not a simple matter. A new figure of merit is first developed which gauges a spectrograph’s capacity to collect or gather information. It is the *potential information gathering power* and is

* “Blue” and “red” are used throughout this work to connote shortward and longward with respect to wavelength.

denoted by \mathcal{P} . This figure of merit is based on the premise that it is desirable to maximize the product of the SNR at each resolution element in the reduced data by the number of resolution elements. As such, \mathcal{P} is unbiased towards any scientific preference. For example, one system which has a large number of resolution elements (or multiplex) and with relatively low SNR can have the same potential information gathering power as another system having a low multiplex, but with a higher overall SNR. This new measure of performance is then applied to the task of optimizing the high resolution mode of the instrument.

An accurate model of the Bench Spectrograph is presented and a method for evaluating the potential information gathering power as a function of various parameters of the instrument is developed. Based on the results, a design is selected and perfected, yielding an average improvement of 15% to 18%, depending on the relative amount of sky background noise (a measure of the amount of non-source flux entering the system from the sky).

A complete glossary of all the symbols employed may be found in Appendix A, where the reader is encouraged to refer to when needed.

5. FIGURES OF MERIT

5.1 BACKGROUND

The optical designer has as his or her mission the goal to create a spectrometer that, given a set of parameters, is *best*. However, due to the wide variety of astronomical programs/interests, it is difficult to agree upon a definition of what exactly this is. Various figures of merit have been proposed which attempt to quantify this term. As astronomy and astronomical instrumentation develop, science and technology have driven reconsideration of these merit figures. The fiber-fed spectrograph (following Schroeder³, a *spectrograph* is a spectrometer employing an area detector with multiple resolution elements) differs from a traditional spectrograph in the way resolution and light-collecting capacity is traded off and in the significance of spatial information.

When one has an *a priori* knowledge of the scientific application for a spectrograph, the design can be tailored to collect information specific to the region under consideration. Unfortunately, it is more often the case that the instrument is to be used for a variety of scientific programs, some of which may even be unknown. In this case, the best instrument is the one that, in the widest range of configurations, provides the potential to collect the most information.

Here, *information* is defined to maximize the product of, “The signal to noise ratio (SNR) [that can be achieved in each spatial and spectral element of the source]”⁴ and the number of resolution elements. The spatial elements of the source should be expressed in terms of a true numerical multiplex reduced from the recorded data, not as a measure of solid angle subtended on the sky. Likewise, the spectral elements of the source should be similarly expressed. The product of these

multiplex values represent the unitless number of reduced resolution elements. This definition, then, links the performance of a spectrograph to that of the telescope and its seeing environment. The key is to define the performance of the system in terms of measurable quantities at the focal surface.

An example of this definition is to note that the information content of one resolution element from which data is reduced with a SNR of 100 can be doubled by either doubling the SNR to 200 or doubling the number of resolution elements to two, each having a SNR of 100. The former case represents a doubling of the information quality and the latter case represents a doubling of the information quantity, or multiplex. The information content, therefore, of a single resolution element with a SNR of 200 and two elements with a SNR of 100 is equivalent since the quality-quantity information product is the same.

Historically, the quantification of a spectrometer's performance began in 1954 when Jacquinot introduced $A\Omega R$.⁵ The argument was made that the effective resolving power of a spectrometer is given as R , the Rayleigh resolution, which is inversely proportional to the slit width (w_{SLIT}). The flux collecting capacity he called *luminosity*, which is stated to be proportional to the dimensions of the dispersive system ($A\Omega$, which is referred to here as *throughput*). The product of these two terms is the throughput-resolution product and was shown to be independent of w_{SLIT} . Sometimes the transmission (T) of the spectrograph is lumped together with $A\Omega$ or $A\Omega R$ and some have chosen to call the former quantity ($TA\Omega$) the *étendue*. Some have recognized that while $A\Omega R$ (or $TA\Omega R$) provides some correlation with the goal to quantify the SNR of the spectra, this correlation is admitted to be that often a larger $A\Omega R$ implies a larger SNR⁶.

The following “first order” equations summarize how the throughput-resolution product may be figured from the parameters of a spectrometer. The first order smallest resolvable wavelength is $\delta\lambda$. The grating angle is α , which is measured from the direction of incident light to the grating normal (a plane grating is assumed). The focal length of the collimator is f_{COL} . The length of the slit is l_{SLIT} . A_{COL} is the area of the collimated beam from a point source. The incident flux on the detector is Φ , and L_λ is the spectral radiance of the astronomical source.

Summary of First Order Equations

$$R = \frac{\lambda}{\delta\lambda} \quad [1]$$

$$= \frac{f_{\text{COL}}}{w_{\text{SLIT}}} \cdot \frac{\sin(\alpha - \varphi_c) + \sin(\alpha)}{\cos(\alpha)} \quad [2]$$

$$A\Omega = A_{\text{SLIT}} \cdot \Omega_{\text{COL,SLIT}} \quad [3]$$

$$\cong l_{\text{SLIT}} w_{\text{SLIT}} \cdot \frac{A_{\text{COL}}}{f_{\text{COL}}^2} \quad [4]$$

$$A\Omega R \cong \frac{\pi l_{\text{SLIT}} f_{\text{COL}}}{4(f/\#)_{\text{COL}}^2} \cdot \frac{\sin(\alpha - \varphi_c) + \sin(\alpha)}{\cos(\alpha)} \quad [5]$$

$$\Phi \cong TL_\lambda A\Omega \quad [6]$$

We see then from Equation 5, that in the first order case (*i.e.*, aberration and diffraction free, with a uniform source filling the slit, and ignoring higher order terms associated with the radiometry), $TA\Omega R$, can be improved by:

1. Increasing the system transmission (T). For example, a great deal of effort is still expended in the development of more efficient A/R (anti-reflection) coatings.
2. Increasing the slit length (l_{SLIT}). This is the driving force behind image slicers.
3. Employing larger optics. For a given collimator (telescope) $f/\#$, f_{COL} is a measure of the system geometry. This is driving force behind Coudé spectrographs. Note that with the fiber-fed spectrograph, $(f/\#)_{\text{TEL}} \neq (f/\#)_{\text{COL}}$ since the fiber throughput is not invariant (see Section 7.2.5).
4. Increasing the grating angle (α). This is the driving force behind Echelle gratings.
5. Minimizing the camera-collimator angle (φ_c). This is the first reason why it is desirable to work as closely to the Littrow case as possible. The Littrow condition occurs when the camera axis is folded back on the collimator axis ($\varphi_c = 0^\circ$).

Another development in the evolution of a figure of merit for a spectrometer came with the advent of *spectrographs*, namely that spectra may be recorded simultaneously across wavelength⁷ and (later) spatial extent of the slit. This multiplexing is referred to as spectral and spatial simultaneity gain and is denoted by the unitless M_λ and M_s . Historically, there has not been a universally adopted definition for these terms, though combining these factors with TAΩR, Meaburn presented the following potential figure of merit⁸:

$$Z_{\text{POT}} = M_y A \Omega R M_\lambda T \quad [7]$$

He noted that while this quantity has some use in comparisons made between spectrometers, it is related to the SNR (the true indication of merit) achieved for each resolution element in a very complex and variable way.

5.2 PROBLEMS WITH TRADITIONAL FIGURES OF MERIT

The five above mentioned principles apply in general to spectrometer design. With spectrographs, the principle of maximizing the simultaneity gains applies as well. However, there are a number of assumptions that have been made and which are now stated:

1. Due to diffraction/grating efficiency, the transmission of the system may have a strong dependence on the grating diffraction angles and, as such, be field dependent.
2. The transmission of the system must include vignetting factors that are field dependent and which tend to push the design **away** from the Littrow condition.
3. Astronomical sources are not extended. In other words, opening up the slit to increase the flux at the expense of resolution can only be pushed so far. While some have argued that there are astronomical sources, such as nebulae, which are extended, a comparative figure of merit should not be based on this specific application.

4. Astronomical sources are not uniform. The angular radiance distribution is the result of atmospheric distortion of a virtual point source. It follows an $e^{-(5/3)\xi}$ dependence in the Fourier domain⁹. This is much better approximated as a Gaussian distribution. While some have felt that a uniform distribution is a valid approximation over a limited region, $A\Omega R$ is clearly not a step function out to the diameter of a rectangular “seeing disk”.
5. The lower limit of slit width does not infer resolutions approaching theoretical values for the grating. In fact, with the notable exception of larger Coudé spectrographs, aberrations, detector sampling, and sometimes camera objective diffraction determine the useful lower limit.
6. The noise per unit resolution element at the detector is *inter alia* a function of both the imaged area on the detector and the slit area. Since these variables factor into $A\Omega R$, it cannot be assumed that the SNR will remain constant as these variables change. Here, noise will be denoted by \bar{n} , which represents the true RMS noise from all sources. It is assumed that a DC bias associated with any of the sources of noise can be perfectly subtracted out.
7. The definition of R is given either in terms of the local minimum of a diffraction limited image with respect to the maximum of another of equal size or by virtue of assuming that the imagery is geometrical. Both of these methods reflect ideal imagery.

Actual images are rarely diffraction limited and may change drastically **within** any given system. As a result, the resolution R will vary across the field.

8. A perfect system is useless unless one can properly extract and reduce the data, *i.e.*, effects from the detector and data analyses must be accounted for.¹⁰

5.3 POTENTIAL INFORMATION GATHERING POWER

A solution that addresses these problems may be found by revisiting the goal of the original figure of merit, $A\Omega R$, namely to measure the product of the instrument's ability to collect the largest fraction of the source incident light and its resolution.

The following two changes are made:

1. The light-collecting capacity is determined as the fraction of transmitted light from the image of the source through the entrance aperture of the spectrometer rather than as a simplification of the radiometric transfer law. The quantity ϕ will represent the relative flux from a normalized Gaussian image having an RMS full-width of 2σ that enters the spectrometer. It is unitless and has maximum value of 1. In the case of the fiber-fed spectrograph, the transmission of the fiber system (*e.g.*, may include prisms and micro lenses in addition to absorption losses) can be lumped together with the transmission parameter T, and not ϕ .

2. The resolution will be determined as the inverse RMS full-width recorded in the instrument focal plane, w , rather than based upon the Rayleigh criteria. The units of resolution may be either linear dimension in the x or spectral direction of the detector or wavelength as related by the reciprocal linear dispersion (see Section 6.1.2). The primary reason for choosing RMS full-width as the measure of resolution is its simplicity. It is the most meaningful single description of the quality of an image. Other candidates are the FWHM and widths associated with fractions of the encircled energy. Furthermore, experience dictates that images tend to be Gaussian like. If the images were products of processes imparting true Gaussian profiles (imaging, pixel sampling, aberrations, and diffraction), they also would be Gaussian. More importantly, the final image distribution can be readily determined since the convolution of these processes is merely the adding of the constituent RMS full-widths in quadrature. However, it is not the shape (distribution) of the acquired image that is important, rather, it is the accurate measure of the width. This is evident in the calculation of the simultaneity gain (*q.v.* below).

For a given resolution element, the new figure of merit analogous to AQR is then:

$$\frac{\phi}{w} \quad [8]$$

However, this term implies nothing about the SNR. Recognizing the numerator as a measure of potential signal, the extrapolation to SNR is found by adding the noise to the denominator. The result is the SNR of a resolution element per unit width w in the focal plane. This is the principal unit figure of merit:

$$\frac{\phi}{w \bar{n}} \quad [9]$$

Some scientific programs are concerned with narrow wavelength regions of interest. These require little or no M_λ and will instead choose to simply maximize the SNR at a specific wavelength. Here, the appropriate unitary term to maximize would be:

$$\frac{\phi}{\bar{n}} \quad [10]$$

These kinds of programs are unconcerned with information outside their region of interest. The goal of this thesis is not to optimize for this type of program.

5.3.1 Per Resolution Element

The potential information gathering power of a system may be maximized by evaluating Term 9 just immediately after the source light passes the aperture of the spectrograph^{11,12}. At this juncture, the light has not been dispersed and certainly has not been imaged onto the detector. Yet, by making some judicious assumptions about the nature of the spectrograph, the trade off between light collecting power and resolution may be evaluated. More importantly, the potential information gathering power, which includes the noise term, can be optimized.

In a traditional spectrograph, this action is accomplished by adjusting the slit width (in the spectral direction). As the slit is enlarged, the light collecting power is increased and the resolution diminished. As discussed earlier (under Section 5.2), the product of these two quantities is not constant, neither are their relationships with the slit width linear. Furthermore, the noise associated with a resolution element is likewise increased as the slit opens. This evaluation, then, allows optimal selection of a slit width based on the spectrograph parameters, imagery delivered from the telescope and seeing environment, and the amount of sky background noise. The latter is function strongly dependent on the phase of the moon. An advantage to the traditional spectrograph is the ability to adjust this slit width as conditions, such as seeing, dictate.

The fiber-fed spectrograph may be analyzed as well. Though, here it is not a physical slit width that is optimized, but rather the diameter of the optical fibers themselves. In the case when there are other optical elements placed before the fibers, such as prisms or micro lenses, it is the image of the fibers which is important. Unlike the traditional (slit) spectrograph, the fiber diameters can not be readily adjusted, for example, to compensate for temporal seeing fluctuations. The fiber-fed spectrograph, however, has the advantage of being able to more efficiently exclude the radially symmetric low flux, hence low SNR, regions of the image by clipping it with a circular aperture as opposed to a rectangular one, typical of slit spectrographs¹³.

5.3.2 Application to the 2-D System

Having fixed the aperture size, the impetus to maximize the potential information gathering power shifts to the spectrograph itself. To evaluate design parameters

for the system, such as whether to minimize aberrations at the expense of transmission, Term 9 must be integrated over wavelength (x) and spatial extent (y). An advantage to defining resolution as w^{-1} is that the integral yields the spatial and spectral simultaneity gain factors. Assume a similarly defined width in the y direction, w_y , as has been done for w (which is also denoted w_x). For the most general case:

$$M_y M_\lambda = \iint_{x,y} \frac{dx dy}{w_x(x,y) w_y(x,y)} \quad [11]$$

The integral is performed over the usable extent of the detector. It should be noted that care must be taken in defining x and y , for the spectra will typically be distorted (curved). The simultaneity gain may be considered as the number of just resolved Gaussians having RMS full-widths of w_x and w_y that can fit on the 2 dimensional detector (array). The integral allows this correspondence to be valid though the widths themselves vary over the extent of the CCD. Figure 2 illustrates the combination of two 1-dimensional Gaussian distributions having the same RMS full-width and amplitude. In case **A**, they are separated by 10% less than their RMS full-width and it is evident that they are clearly resolved. In case **B**, the separation is equal to the RMS full-width. Here, the combination is at the critical juncture where the central depression just disappears. In case **C**, the separation is reduced to 10% less than the RMS full-width and the combination is clearly unresolved.

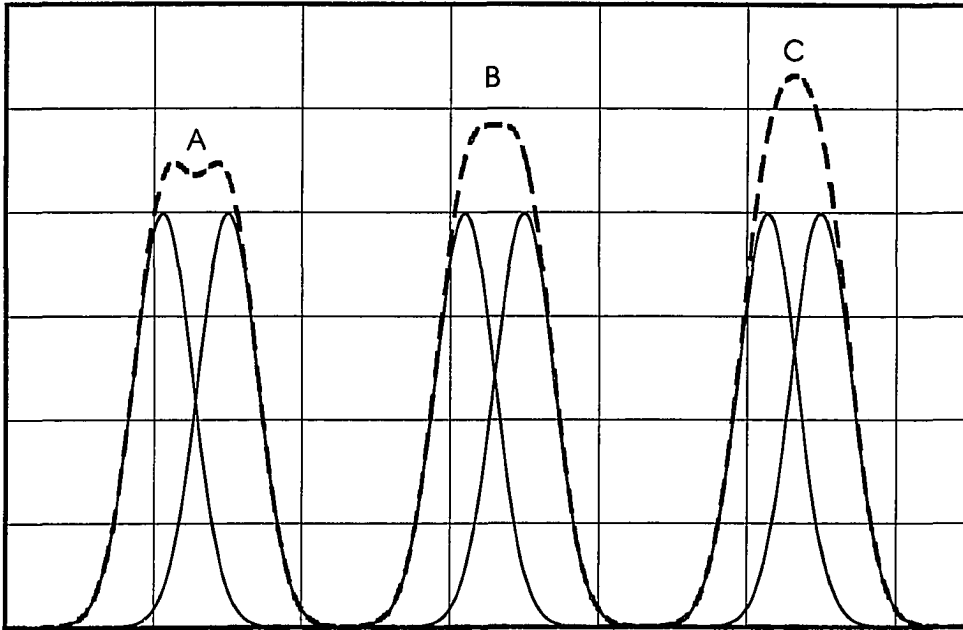


Figure 2, Gaussian Widths and Resolvability

Integrating Term 9 over the usable extent of the detector yields a general figure of merit that represents the SNR-weighted simultaneity gain:

$$\mathcal{P} \equiv \phi \iint_{x,y} \frac{T(x,y)}{\bar{\Pi}(x,y) w_x(x,y) w_y(x,y)} dx dy \quad [12]$$

This is the potential information gathering power. It is *potential* since no degree of value has been placed on the data (information). In other words, very often a researcher will be concerned with a subset of the data recorded on the detector or will assign a preference to a region of interest. Also, nothing has yet been assumed as to the kind of instrument with which the data is being evaluated. This

term merely represents the quality-quantity product of information in the focal plane. And, in fact it can be applied to a non-spectroscopic imaging system. As an example of this, assume that this figure of merit is being applied to a 2-dimensional astronomical imaging system and that the extent of the detector subtends a region of the sky much larger than the source. Much of the *potential* information is then unrealized.

Note the inclusion of the field dependent transmission, $T(x, n_y)$. For the spectrograph, the transmission term includes losses due to absorption, media interfaces such as Fresnel reflections and mirrors (ϵ_r), vignetting (ϵ_v), and grating efficiency (ϵ_g):

$$T(x, y) = \epsilon_r(x, y)\epsilon_v(x, y)\epsilon_g(x, y) \quad [13]$$

For a fiber-fed spectrograph, provided the fibers are indeed separated (or if any overlap is appropriately modeled as noise), the integral over spatial extent becomes a sum over the fibers, where N_{FIB} is the total number of fibers:

$$\mathcal{P} = \phi \sum_{n_y=1}^{N_{\text{FIB}}} \int_x \frac{T(x, n_y)}{\bar{n}(x, n_y)w(x, n_y)} dx \quad [14]$$

The assumption made here is that the imagery changes little over the spatial dimension of the fiber. In practice, it is necessary either to measure or model the transmission (T), noise term (\bar{n}), and RMS full-width (w) over the field. When this is done for two or more configurations, a direct comparison is made of the potential information gathering power. Since this work is concerned with an

improvement of this quantity, as opposed to calculating an absolute number, the modeling of \mathcal{P} will be normalized to the original unmodified spectrograph configuration.

The principal advantage of the traditional slit spectrograph over the fiber-fed version is in the number of additional spatial resolution elements. The principal disadvantage is the limitation of where in the telescope field of view they must come from (normally, along a linear slit). Because of this, the traditional slit spectrograph will provide a greater potential information gathering power over the fiber-fed version. Consider that a typical astronomical fiber-fed spectrograph has between 30 to 200 fibers. If a typical slit spectrograph can sufficiently image the field (spatial extent of the slit) onto a CCD having approximately 1000 pixels in the spatial direction, and assuming spectrograph properties such that the spatial RMS full-width (w_y) is an average of 3 pixels, the spatial simultaneity gain (M_y) is roughly 330, a factor of 1.5 to 7 better than the fiber-fed spectrograph. All other factors being the same, the potential information gathering power would be similarly greater.

However, the fiber-fed spectrograph will still have a greater information gathering power (*potential* is absent). This is because with the notable exception of long slit spectroscopy of extended sources, the average number of useful objects that can be placed along the slit is less than 2. While, within a 1° field of view, it is not unreasonable to expect on the order of 100 objects with enough separation to image onto a fiber-feed. Ingerson has accounted for this in his figure of merit, the *realizable multiplex advantage*¹⁴. Realizable multiplex advantage considers the task of quantifying the “all things considered” advantage of using the fiber-fed

spectrograph in lieu of the traditional spectrograph for certain astronomical observing programs, a comparison across 2 types of spectrographs. Potential information gathering power is not intended be used as a comparison across instrument classes, but rather as a tool for evaluating performance and performance options within a class. Examples of the kinds of design options which can be evaluated by \mathcal{P} are:

1. Selecting an optimal camera objective (*e.g.*, lossy and low aberrations versus highly transmissive with worse imagery).
2. Modular additions such as evaluating the merits of adding a field lens.
3. Whether or not and how much to vignette the system.
4. Optimal camera-collimator angle (φ_c).
5. Selecting an optimal detector (*e.g.*, larger format with higher noise properties versus a lower noise smaller format version).

6. FORMULATION OF THE TASK

6.1 DESCRIPTION OF THE SPECTROGRAPH

As already stated, the Bench Spectrograph employs a two dimensional CCD detector array at the focal surface to simultaneously record data in wavelength and spatial extent (multiple spectra). The light enters the spectrograph via one of two currently available fiber optic cables. One is comprised of fibers optimized for the blue (.350 to .550 μm). The fibers in this cable have nominal diameters of 310 μm . The other cable is optimized for the red (.450 to 1.0 μm) with fibers having a nominal diameter of 200 μm . Each cable contains 96 individual fibers. There is a robotic fiber positioner at the Nasmyth focus of the telescope which can pick and place each fiber to the arbitrary coordinates of any astronomical source within the two dimensional field of view of the telescope.

By choosing the appropriate optical cable, selecting one of 6 available gratings, selecting a diffraction order, adding an order separating filter, and picking one of two available camera objectives, a host of wavelength regions and dispersions may be achieved (approximately .06 to 2.6 $\text{\AA}/\text{pixel}$). Furthermore, the camera axis mount is constructed so that it may rotated about the center of the grating, allowing the camera-collimator angle, ϕ_c , to be set to any value in the range of 11° to 80° . It is the physical size of the instrument and the need to keep the collimator and camera axes beams separated which dictates the low end of this range.

The following figure shows top and side views of the layout of the spectrograph. It is schematic, intended to be used to identify parameters and relate concepts. Not all of the components are shown. The local coordinates are x , y , and z , where z is the direction of the propagating wavefront for the "no field" case (the central fiber

where $y = 0$) at the chief wavelength. The chief wavelength is defined as the wavelength which exactly diffracts down the center of the camera axis ($x = 0$) for no field. The spatial direction is y , which is always perpendicular to the plane containing the camera and collimator axis. The spectral direction lies in x . Note that due to the conical diffraction distortion (spectra curvature), a strict identification of x and y with the spectral and spatial directions is not possible.

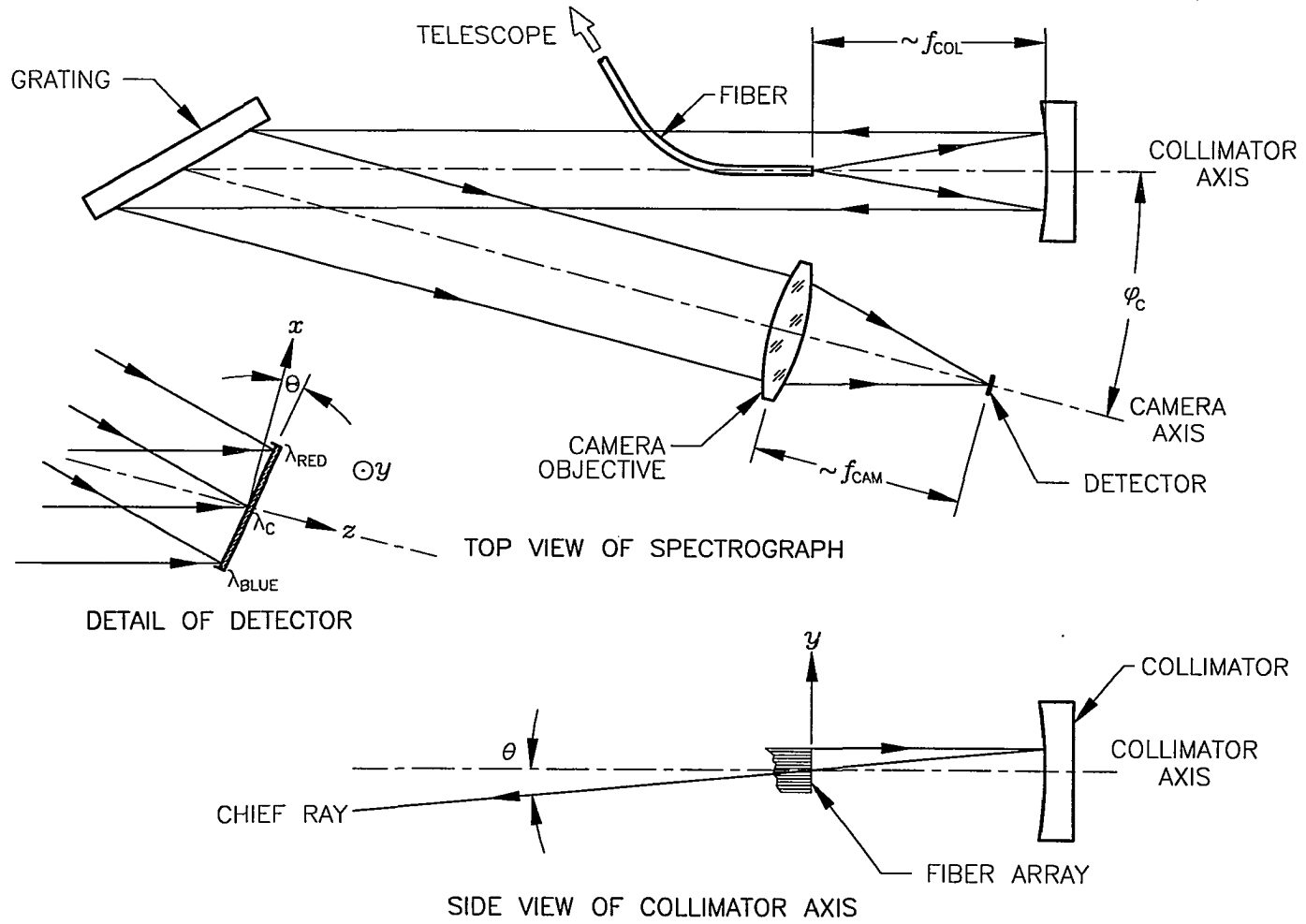


Figure 3, Spectrograph Layout

6.1.1 Module Details

The spectrograph design is modular. That is to say that there are several stand-alone electro-opto-mechanical components that are independently positioned and aligned on a 5' x 8' optical table. Each of these modules has various functions and adjustments, many of which can be controlled automatically.

The Fiber Module takes an optical cable and arrays the fibers accurately into a 76 mm long "slit". The axes of the fibers are parallel with respect to each other, the surface of the optical table, and the plane containing the collimator and camera axes. As such, the fibers are said to be telecentric since the chief rays* of all the fibers are parallel. The spatial dimension is into/out-of the table and this is the direction in which fibers are stacked one on top of the other. The central fiber lies on the collimator axes with half of the field being below and the other half above it. The system is almost symmetrical with respect to field ($\pm y$). The reason it is not exact has to do with the central obscuration of this module. The fibers lie in the center of the return beam from the collimator. In fact, this is the location of the unmodified spatial pupil. The obscuration from the mechanical "foot" which holds the fibers is made as thin as possible (13 mm) to reduce the obscuration (vignetting) of the return beam. This foot extends above the fiber array toward the direction from which the fiber cable comes from the fiber positioner, hence the lack of spatial symmetry.

* In a strict sense, there is only one chief ray for an optical system. Here, "chief rays" refer to the axes of the emitted light from which the radiance patterns are radially symmetric.

The entire Fiber Module translates along the collimator axis, allowing focusing of the collimator, which is stationary. The Fiber Module also has mechanisms for placing filters directly in front of the fiber array. The high-resolution mode utilizes an interference filter to perform order separation. The pass bands for an extant set of filters have been designed for a camera-collimator angle of 11° . The mechanism for placing the field lens in front of the fibers will be part of the Fiber Module as well. The distance between the fiber array and the collimator is nominally the focal length of the collimator, but is modified to compensate for the reduced thickness of refractive elements placed in front of the fibers (filters and a field lens) and power in the optional field lens. In addition, the focus may be allowed to vary slightly from the nominal value to allow balancing of the field aberrations.

The original collimator is a parabolic reflector centered on the collimator axis. It has a focal length of 1021 mm and produces a nominal 170 mm diameter circular beam (per fiber), assuming that the fiber radiance pattern is an $f/6$ uniform distribution. The collimator is coated with aluminum (oxide). The diameter of the blank is 254 mm, 242 mm of which is usable (due to edge effects from the manufacturing processes).

The Grating Mount is built on top of a rotary stage with a resolution of approximately 10 arc-seconds and an absolute accuracy of about twice that. It is designed so that grating cells may be freely interchanged while maintaining the alignment of the system. There are currently four low order ($m \leq 3$) gratings and an Echelle, designed to operate at $6 \leq m \leq 16$. All gratings are aluminized.

Frequency	316 l/mm	400 l/mm	600 l/mm	860 l/mm	1200 l/mm	316 l/mm
Blaze Angle	6.7°	4.8°	13.9°	30.9°	28.7°	63.4°
Useful Orders	1,2	1	1,2	1-3	1,2	6-16
Notes		Planned				Echelle

Table 1, Available Diffraction Gratings

There are two available camera objectives, each of which has an integral large sliding shutter. The first is called the Simmons Camera. It is a catadioptric design, having a focal length of 381 mm and an entrance aperture of 211 mm. The refractive elements are made of fused silica. It has seen service at Kitt Peak National Observatory for many years and has been modified for use on the Bench Spectrograph. The catadioptric design lends itself well to traditional astronomical spectrographs since the shadow from the telescope's secondary mirror is preserved in the spectrograph beam. Hence, the central obscuration from the camera objective's secondary mirror adds little vignetting. However, with a fiber-fed spectrograph this is not the case. The mode-diffusing properties of the fibers spread the light so that the beam exiting the fiber is flatter and more uniform than that entering the fiber and, to some degree, the telescope's secondary shadow is lost. In this case, a catadioptric design is not preferred.

A second camera objective is now being constructed for the spectrograph. It is called the Bench Spectrograph Camera. It has a median focal length of 285 mm and an entrance aperture of 206 mm. It is an all-refractive modified Petzval design¹⁵. The air-glass interfaces have complex extreme wide-band A/R coatings that are good from about .400 to 1.0 μm . Due to its lack of any central obscuration and shorter focal length, most regular use of the instrument will be with this objective. Because the optical glasses employed have greater dispersions than the

fused silica of the Simmons Camera, the focal length has a stronger dependence upon wavelength.

The detector is a SITE 2048² large format CCD with 24 μm pixels. The imaging area measures 49.15 mm on a side. Roughly half of the pixels in the spatial direction are used. This depends on which camera objective is employed due to the change in spatial magnification:

$$m_y = \frac{f_{\text{CAM}}}{f_{\text{COL}}} \quad [15]$$

The detector is housed in an LN₂ cooled dewar. The azimuth of the dewar with respect to the camera axis is adjustable, allowing for good compensation of the longitudinal chromatic aberration of the Bench Spectrograph Camera. The CCD is a thinned back-side illuminated device which yields good spectral response from atmospheric “cut-off” in the UV (.350 μm) to the cut-off wavelength associated with the band gap energy of Si (approximately 1.0 μm). However, the CCD has one major flaw. It is intrinsically warped due to the fabrication process of the wafer. Furthermore, it is convex, which opposes the field curvature of the camera objective. There is an effort underway, which is not covered in this work, to compensate for this warp by re-designing either the rear element of the Bench Spectrograph Camera or the normally plano-plano dewar window.

The shape of the CCD was measured by the manufacturer (SITE) at room temperature and found to be rotationally symmetric. However, the way in which the warp is produced is a thermal process which is exacerbated when the CCD is cooled. This change was measured optically with a traveling microscope and

found to be a linear scale increase of 34%, meaning that the z distance from the vertex as a function of radial position, r , is approximately 34% greater than measured by the manufacturer*. A conic was fit to this scaled data and was found to be that of a hyperboloid having a radius of 1365 mm and constant (k) of -1682. It is shown below:

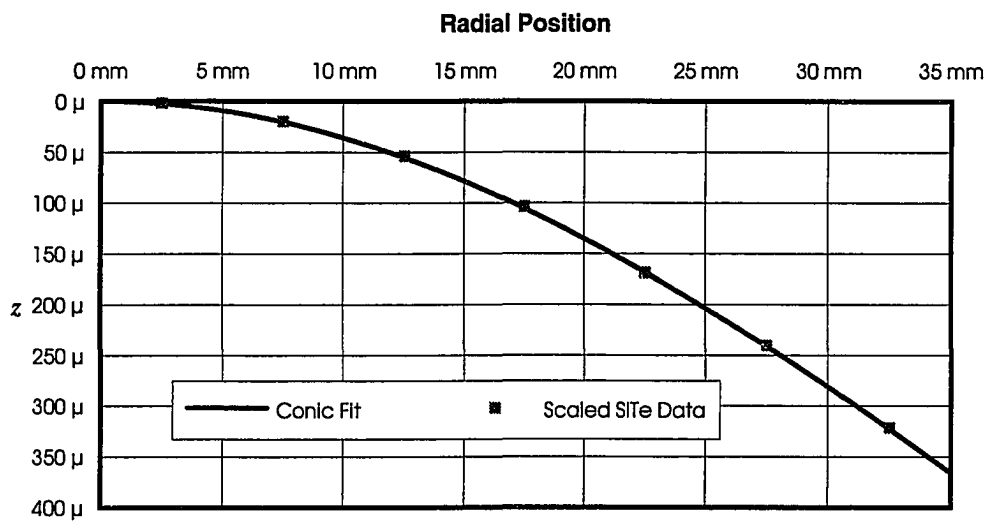


Figure 4, Intrinsic Warp of the CCD

* Subsequent to this analysis, the cold warped shape was more accurately measured and found to be equivalent to a 12% (not 34%) increase of $z(r)$.

6.1.2 Grating/Diffraction Principles

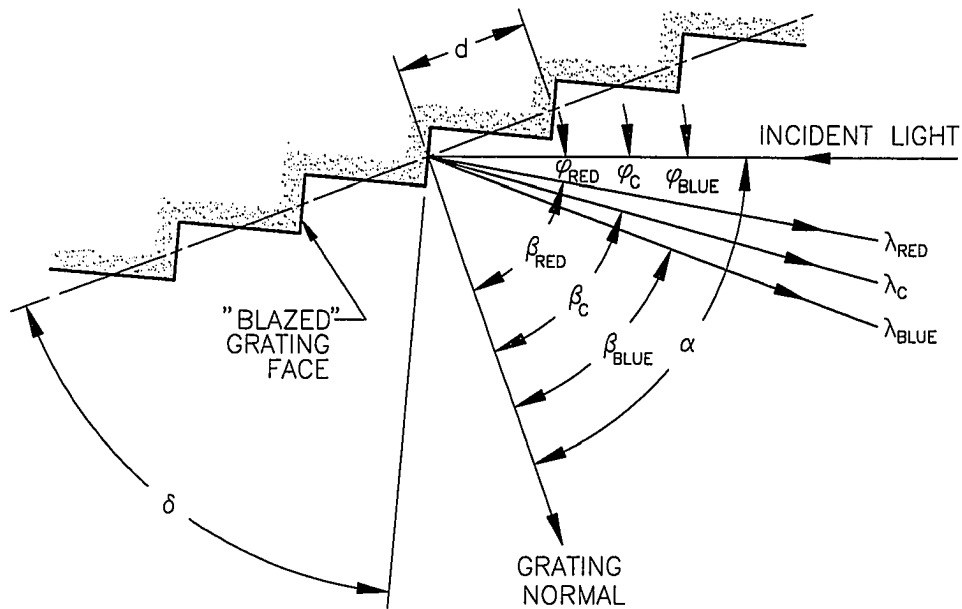


Figure 5, Diffraction Geometry

The following fundamental equations are based on the Physics of diffraction and constructive interference. Here, a choice has been made to solve these in terms of ϕ rather than β (a measurement with respect to the incident angle as opposed to the grating normal) because the camera-collimator angle, ϕ_C , is an independent parameter of the spectrograph. Note as well the sign convention adopted for α , β , and ϕ . All quantities are positive when $\alpha > \beta$, the normal condition for a spectrograph of this type. The groove spacing is denoted d and the diffraction order is m . A summary of the grating Physics relationships for these terms follows:

Summary of Grating Physics Relationships

$$\varphi = \alpha - \sin^{-1} \left[\frac{m\lambda}{d} - \sin(\alpha) \right] \quad [16]$$

$$\alpha = \sin^{-1} \left[\frac{m\lambda}{2d \cos(\varphi/2)} \right] + \frac{\varphi}{2} \quad [17]$$

$$\lambda = \frac{d}{m} [\sin(\alpha - \varphi) + \sin(\alpha)] \quad [18]$$

$$\varphi = \alpha - \beta \quad [19]$$

There are three concepts of interest to the spectroscopist which go with these fundamental equations: resolution, dispersion, and the free spectral range. Resolution, $\delta\lambda$, is now defined as the measured RMS full-width in the spectral direction, w , given in units of wavelength. It must include all the processes required to obtain and reduce the spectra. Normally, w is computed or measured in units of physical linear dimension on the detector (or in number of pixels). These units are converted to wavelength by multiplying by the reciprocal linear dispersion ($d\lambda/dx$), which is also loosely called “dispersion”.

$$\delta\lambda = w \frac{d\lambda}{dx} \quad [20]$$

The term $d\lambda/dx$ may be derived by differentiating Equation 18 and assuming no 3rd order distortion (more correctly, that the image centroid with field position maintains the linear relationship given by first order optics) so that:

$$\tan(\varphi - \varphi_c) = \frac{-x}{f_{CAM}} \quad [21]$$

The sense of x is positive in the direction of decreasing φ , as shown in Figure 3.

Combining Equations 18 and 21 and differentiating yields:

$$\lambda = \frac{d}{m} \left\{ \sin \left[\alpha - \tan^{-1} \left(\frac{-x}{f_{CAM}} \right) - \varphi_C \right] + \sin(\alpha) \right\} \quad [22]$$

$$\frac{d\lambda}{dx} = \left\{ \cos \left[\alpha - \tan^{-1} \left(\frac{-x}{f_{CAM}} \right) - \varphi_C \right] \cdot \left[\frac{-1}{1 + \left(\frac{x}{f_{CAM}} \right)^2} \right] \cdot \frac{-1}{f_{CAM}} \right\} \quad [23]$$

$$= \frac{d}{m f_{CAM}} \cos(\alpha - \varphi) \left[\frac{1}{1 + \tan^2(\varphi - \varphi_C)} \right] \quad [24]$$

$$= \left(\frac{d\lambda}{dx} \right)_{NOM} \left[\frac{1}{1 + \tan^2(\varphi - \varphi_C)} \right] \quad [25]$$

Where NOM represents the nominal value at $\varphi = \varphi_C$,

$$\left(\frac{d\lambda}{dx} \right)_{NOM} = \frac{d}{m f_{CAM}} \cos(\alpha - \varphi) \quad [26]$$

The sense of Equation 24 is such that as x is increased from zero at the center of the CCD toward the collimator axis (decreasing φ), λ increases or gets “redder”. Note also that the last term (in the brackets) represents the change from the nominal reciprocal linear dispersion at the center of the detector. For small spectral field angles ($|\varphi - \varphi_C| \leq 5^\circ$, *cf.* Equation 40), this term reduces the nominal value by less than a percent at the edges and is normally ignored.

Another diffraction property that should be defined is free spectral range, $\Delta\lambda$. It is a measure of the usable width of a diffraction order (in wavelength). For a given set of diffraction parameters (d and α), there are a finite number of potential orders

which will diffract in the same direction φ . These will be approximately separated by:

$$\Delta\lambda = \frac{\lambda}{m} \quad [27]$$

Actually, the separation to the next higher (bluer) order will be slightly less than and the separation to the next lower (redder) order will be slightly greater than the free spectral range. However, the harmonic mean of the two separations will exactly be the free spectral range. In practical terms, attempting to simultaneously image more than a free spectral range on to the detector without cross-dispersing is not viable.

Finally, the first order imaging properties of a plane grating spectrograph will be altered in the spectral direction by the anamorphic factor. The anamorphic factor, r , is the ratio of the width of a collimated beam incident on the grating to the unvignetted width of the beam diffracted from the grating:

$$r = \frac{D_{\text{COL}}}{W_{\text{CAM}}} \quad [28]$$

$$= \frac{\cos(\alpha)}{\cos(\alpha - \varphi)} \quad [29]$$

The collimator beam shape is circular so the width is written as a diameter. Provided there is no vignetting at the grating (a.k.a. underfilling) the diffracted beam will be elliptical. For this spectrograph $\alpha > \varphi$ and $r < 1$, so W_{CAM} is the major axis of the ellipse.

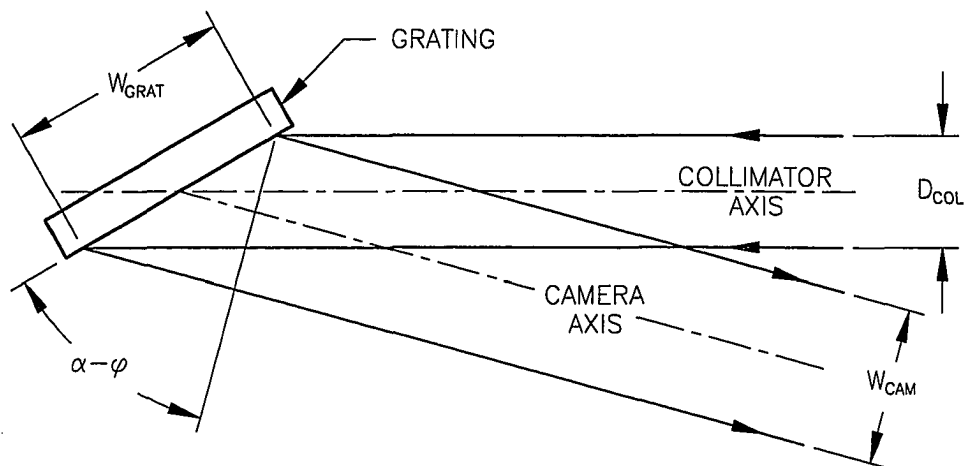


Figure 6, Grating Geometry

The magnification in the spectral direction, m_λ , is equal to the regular (or spatial) magnification altered by this anamorphic factor.

$$m_\lambda = m_y \cdot r \quad [30]$$

$$= \frac{f_{\text{CAM}}}{f_{\text{COL}}} \cdot \frac{\cos(\alpha)}{\cos(\alpha - \varphi)} \quad [31]$$

A simple rationalization of this effect is to consider the grating expanding the collimated beam by r^{-1} . The same expansion can be accomplished by increasing the focal length of the collimator, $f_{\text{COL}} \rightarrow f_{\text{COL}}/r$, which would decrease the magnification by r .

6.1.3 The High Resolution Mode

Angular dispersion is usually given as $d\beta/d\lambda$. "Higher" or "more" resolution is taken to imply a smaller $\delta\lambda$. For a fixed w , this in turn implies a greater angular

dispersion and a smaller reciprocal linear dispersion. The units of the latter are usually given as either $\text{\AA}/\text{mm}$ or $\text{\AA}/\text{pixel}$. So, for astronomers who want to do science at high resolution, one or more of the following must occur (see Equation 26):

1. Use a longer focal length camera objective. The problem with this is that unless the system is pixel sampling limited, increasing f_{CAM} similarly increases w .
2. Use a grating with a high groove frequency (smaller inter-groove spacing, d). However, there is a practical limit of about 1000 $//\text{mm}$ for making large gratings.
3. Use a higher order. The problem here is that with standard gratings, any order higher than about 2-3 produces spectra too "blue" to be useful.
4. Operate at a higher grating angle, α . Unfortunately, most standard gratings are not blazed to be efficient in this respect. Also, this requires gratings that are much wider since the size presented to the collimator axis is proportional to $\cos(\alpha)$.

Echelle gratings are a special type designed for high resolution work. Typically, they operate at orders from about 5 up to 100. They have moderate groove frequencies but derive their dispersive power from the inherent high blaze angle, δ , which is tipped back toward the collimator axis at a large angle so that β (or $\alpha - \phi$) and m are large. They are designed to be used at grating angles in the

range of $60^\circ \lesssim \alpha \lesssim 80^\circ$ (cf., standard gratings typically operate in the range $20^\circ \lesssim \alpha \lesssim 45^\circ$).

In order to operate at these high grating angles, the gratings must be very wide. There is an accepted designation that identifies the ratio of an Echelle's width (perpendicular to the grooves) to its height (along the grooves). An R2 Echelle, such as the one used on the Bench Spectrograph, implies that the width to height ratio is 2. Its ruled area measures 406 mm x 206 mm. A typical realizable resolution available with this Echelle is $.25 \text{ \AA}$, roughly a factor of 5 better (finer) than the 860 //mm grating operating in second order.

6.2 THE PROBLEM

In order to utilize Echelle gratings efficiently, the following conditions should be met:

1. To maintain high resolutions, β (or $\alpha - \varphi$) should be kept as large as possible. This tends to push φ as low as possible.
2. To minimize vignetting, α must be kept low enough so that beam coming from the collimator does not appreciably overfill the grating. The Bench Spectrograph has a 406 mm wide Echelle and approximately a 170 mm wide collimator beam. In this case, the grating angle should be preferably kept to $\alpha \lesssim 70^\circ$.
3. The grating efficiency should not be compromised as a result of the configuration (choosing φ_c). This is a very complicated

issue that will be described in detail in Chapter 7. However, some general rules of thumb are:

- A. A significant fraction of the incident light should not hit the back (unintended) side of the blazed facet. This occurs at $\alpha \leq \delta$.
- B. The setup should be within half an order of being “on-blaze”.

The last condition above (3B) requires some explanation. The “on-blaze” or Ebert configuration corresponds to the case when the diffraction is specular with respect to the facet normal. This is met when:

$$\alpha = \frac{\varphi}{2} + \delta \quad [32]$$

Here, the angles of incidence and diffraction for a given wavelength are symmetrical about the facet normal. In terms of scalar diffraction theory, this is equivalent to the wavefront coming from a facet remaining in-phase in the far-field (*i.e.* in the given direction of φ). Substituting Equation 32 into Equations 16 and 18 yields:

$$\varphi_{\text{BL}} = 2\cos^{-1}\left[\frac{m\lambda}{2d\sin(\delta)}\right] \quad [33]$$

$$\lambda_{\text{BL}} = \frac{2d}{m}\sin(\delta)\cos\left(\frac{\varphi}{2}\right) \quad [34]$$

Where, the subscripts BL have been added to show the on-blaze condition. Solving the last equation for order number gives a measure of how far off-blaze an actual configuration is:

$$m_{\text{OFF}} = \frac{2d}{\lambda} \sin(\delta) \cos\left(\frac{\varphi}{2}\right) \quad [35]$$

The diffraction order, m_{OFF} , will no longer be an integer. If m_{OFF} is more than half an order ($\pm 1/2$) different from the actual order, m , there will be some other order, m' , which is closer to being on-blaze. The diffracted light will, of course, be directed in another direction φ' . And, there is a reasonable chance that this other order will be more efficient.

The result of the three conditions is that as far as grating efficiency is concerned, the ideal camera-collimator angle is the lowest allowable value. This is the second reason why it is desirable to work as closely to Littrow as possible. This is shown graphically in the following three figures, where the combinations of m and α required to yield the wavelengths in the visible range are shown for three increasing values of φ_c . The curved lines are the values of α which yield the particular wavelength for the given orders. Some of the order numbers are shown below these curves. These unitarily increase to the blue (left) and decrease to the red (right).

Three horizontal lines are shown as well. The top line shows the value of $\alpha = 75^\circ$, above which the vignetting is unacceptable. The middle, or dashed line, represents the on-blaze condition (which is a function of φ_c). And, the lowest horizontal line is for a value of $\alpha = 60.5^\circ$, which is the point at which 10% of the incident light

strikes the back side of the blazed facet. Below this, it is expected that the efficiency will be unacceptable. An analysis of the grating geometry yields the following equation for computing this fraction, designated F_{BACK} :

$$F_{\text{BACK}} = \tan(\delta)\tan(\delta - \alpha) \quad [36]$$

Finally, squares show the position on each order where $m_{\text{OFF}} = m \pm 1/2$. Above the upper squares and below the lower squares, adjacent orders will be closer to the on-blaze condition. Notice how the squares from adjacent orders line up vertically.

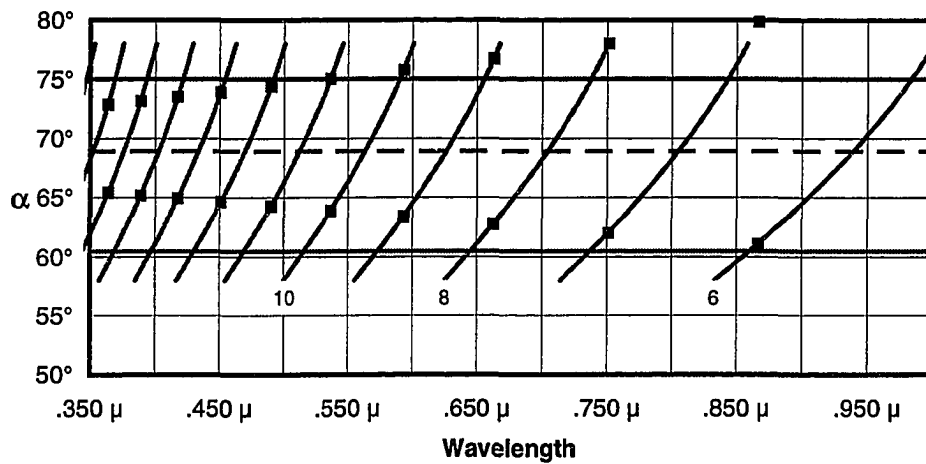
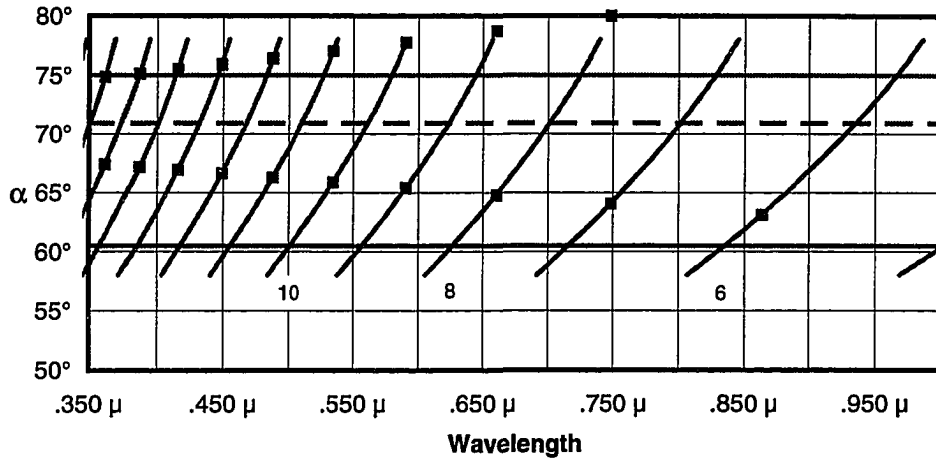
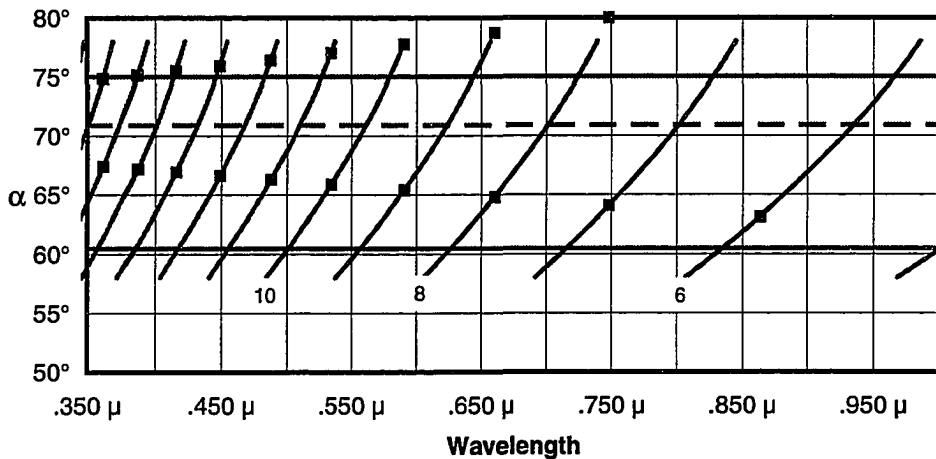


Figure 7, Diffraction Orders for $\phi_c = 11^\circ$

Figure 8, Diffraction Orders for $\phi_c = 15^\circ$ Figure 9, Diffraction Orders for $\phi_c = 19^\circ$

As can readily be seen, as ϕ_c is increased, it becomes more difficult to meet these three ideal conditions for all wavelengths. The blaze condition progressively shifts upward, making it difficult (in fact, impossible for some wavelengths) to simultaneously remain within half an order of being on-blaze and satisfy the

vignetting requirement ($\alpha \leq 75^\circ$). The consequence is that the camera-collimator angle, φ_c , should be minimized. A quantification of this rule of thumb is presented in Chapter 7.

Herein lies the difficulty. The narrower the angle between the camera and collimator axes is, the farther the camera objective must be removed from the grating, worsening the vignetting in both the spatial and spectral senses. Standard low-order gratings may be employed with a camera-collimator angle of $\alpha \cong 30^\circ$, allowing the camera aperture to be close to the grating, which is the spectral stop*. This in turn keeps vignetting in the camera down to a manageable level. The situation is not as fortunate for the high-resolution mode.

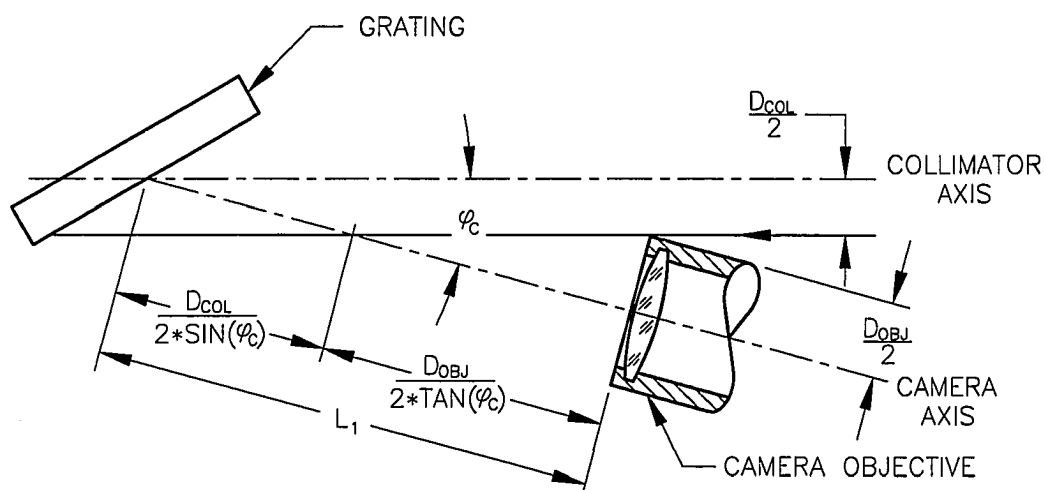


Figure 10, L_1 Geometry

* The classical definitions for stops and pupils are strained for spectrographs. Does the grating "limit" the amount of light passing through (diffracting from) it in the spectral sense? Worse yet is the significance of the spatial pupil for the fiber-fed spectrograph, for it has no physical stop!

The variable L_1 represents the minimum distance between the grating and camera aperture necessary to keep the beam coming from the collimator unvignetted by the camera objective. With a fiber radiance pattern given by $(f/\#)_{\text{FIB}}$, a physical camera aperture given by D_{OBJ} , and assuming no vignetting (perpendicular to y) at the grating, L_1 can be computed:

$$D_{\text{COL}} = \frac{f_{\text{COL}}}{(f/\#)_{\text{FIB}}} \quad [37]$$

$$L_1 = \frac{D_{\text{COL}}}{2 \sin(\varphi_c)} + \frac{D_{\text{OBJ}}}{2 \tan(\varphi_c)} \quad [38]$$

The radiance pattern emitted from the fibers is not entirely known (see Section 7.2.4), though it is assumed that it may be approximated by that of a uniform radiance distribution equivalent to $f/6$. This is where Barden has interpolated 90% of the incident light from an $f/6.3$ (the telescope beam speed) input distribution to fall within¹⁶. With $f_{\text{COL}} = 1021$ mm and $D_{\text{OBJ}}/2 = 115$ mm (as with the Bench Spectrograph Camera), $L_1(\varphi_c)$ is then:

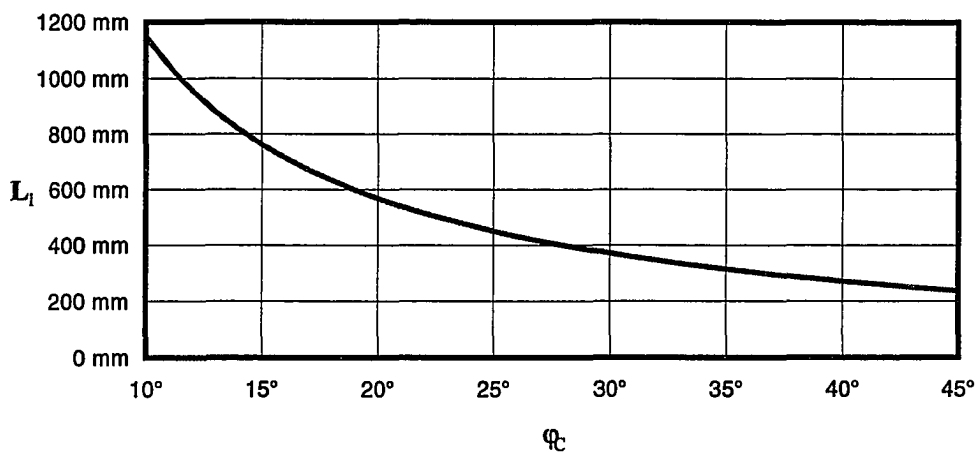


Figure 11, $L_1(\phi_c)$

Because the distance from the grating to the camera aperture for the Echelle operating at $\phi_c = 11^\circ$ is three times that for the standard grating ($\phi_c = 30^\circ$), about half of the light is lost (vignetting). This is an average amount over all of the utilized two dimensional field. The vignetting at the center of the field is not effected by increasing ϕ_c , but the corners of the field see almost a four-fold reduction in their irradiance. The particular problem with the high-resolution mode is the inability to simultaneously maintain good grating efficiency and keep the vignetting as low as possible.

6.2.1 Possible Solutions

There are several possible solutions to this dilemma. These may be combined to produce the overall best result (here defined as maximizing the potential information gathering power):

1. Finding the optimal φ_c by modeling and balancing the parameters which constitute \mathcal{P} , (such as the average grating efficiency, vignetting, and imagery) as a function of φ_c .
2. Re-imaging the spatial pupil into the location that minimizes the overall vignetting. Unfortunately, there is no practical way to similarly re-image the spectral pupil. However, at least the vignetting at the corners of the two dimensional field has a chance to be reduced to the levels for the extreme wavelengths for which $y = 0$ (the spectral edges of the field). There are two principal ways to accomplish this:
 - A. "Fanning" the fibers: The fibers can be arrayed to follow any arbitrary function. Other than linearly with equal separation (as is adopted here), the second most common shape is a radial fan pattern about some point on the collimator axis behind from where they emit. The chief rays from the fibers then diverge from a spatial pupil behind the array. The problem with this method is that the spectrograph depends on interference filters to provide order separation, not cross-dispersion (typical of non-fiber-fed spectrographs with much less free-spectral range). Due to the nature of thin films, if the beams are tilted with respect to the filter normal (as fanning would accomplish), the pass bands will unacceptably spread and shift to the blue as a function of field position.

- B. Adding a field lens in front of the fibers: In this case, the field lens may be placed after the interference filter, avoiding the aforementioned problem. The primary independent parameter of this lens is the direction of the chief ray as it leaves the field lens. First order optics relates the curvature of the back surface of the lens (R_2) to the angle of the chief ray, \bar{u} , and this angle to the location of the re-imaged spatial pupil. There are some additional parameters that may be optimized, though these have real constraints. They are the curvature of the front surface (R_1), the separation between the back of the interference filter and the front of the lens (Δz_{SEP}), the thickness of the lens (Δz_{THK}), and the refractive properties of the glass.
3. Changing the parameters of the collimator (focal length and size): A shorter focal length collimator will produce a smaller diameter collimated beam (per fiber) which may manifest reduced vignetting. Although the unmodified collimator does not vignette, if a field lens is incorporated so the chief rays from each fiber diverge, the collimator may need to be enlarged.

6.2.2 Summary of “Free” Variables

“Free” variables are spectrograph parameters which may be changed on a per configuration basis, *i.e.* relatively easily. They are:

1. The camera collimator angle, φ_c .
2. The separation between the fibers and the collimator (a.k.a. the collimator focus).
3. The so called back focal distance (Δz_{BFD}). This is not the last separation in the optical system. The detector is integral to a dewar, which has a fixed distance between a plano-plano window and the CCD. The interspatial media is vacuum. The dewar as a whole is translated along the camera axis to provide focusing of the camera. As a result, Δz_{BFD} is measured from the rear vertex of the last element of the objective to the front of the dewar window.
4. The dewar azimuth, Θ . This is a tilt about y that the dewar may be offset from the camera axis. The primary beneficiary of this free parameter is longitudinal chromatic aberration of the all-refractive Bench Spectrograph Camera. However, due to the limited single-configuration wavelength region of the high-resolution mode, this is not a driving factor anyway.

6.3 THE TASK

In summary, there are two potential major design changes (the addition of a field lens and the revamping of the collimator) and four free variables that can be configured on short order. Simply put, the task at hand is to determine the combination of these parameters which produces the greatest (if any) increase in potential information gathering power for the entire wavelength region over the

range of operational conditions. The one variable operational condition that can impact this evaluation is the degree of sky background noise.

The best design will, at the very least, consider adding a field lens and/or new collimator so that by tweaking the free parameters on a case by case basis, there will be a measurable improvement in the capacity for the spectrograph to collect information. Before these changes can be evaluated, an accurate model of the unmodified system and the information collection process must be formed. It will be evaluated and become the standard by which potential improvements will be judged. This unmodified spectrograph is one with no field lens, the current collimator, the camera-collimator angle set to the minimum ($\varphi_c = 11^\circ$), and the free variables optimized for any wavelength. It will be assumed that the Bench Spectrograph Camera will be utilized.

7. GRATING EFFICIENCY

By a large margin, the most arduous task in modeling the spectrograph has been determination of the grating efficiency as a function of the dependent parameters. As such, an entire chapter will be devoted to its treatment. The goal is to arrive at the best model of the average unpolarized diffraction efficiency as a function of the grating diffraction angle, φ , and field variable, y , for the Echelle grating in use, $\epsilon(\varphi, y)$. Here, average is taken to represent the efficiency for all practical combinations of wavelengths and (diffraction) orders. The efficiency has been modeled two ways and measured *in-situ* as well. A fit of the data from these three methods is made and then incorporated into the complete model for \mathcal{P} .

It is important to note, from the onset, that for any particular m , d , and λ (and assuming for the moment that $y = 0$), there will be, in general, a complex or even anomalous functional dependence of efficiency with φ . With m and d held constant and λ allowed to vary, the shape of this efficiency function will change. This thesis is not concerned with these kinds of changes. It is not concerned with the specific problem of optimizing for any single combination of these variables. Rather, if a representative set of these complex efficiency functions is averaged together, the result will be a function that is much less complex. In fact, the resultant efficiency will typically exhibit a monotonically decreasing dependence upon φ .

This is the larger picture which is important in understanding the average trade off (principally) between grating efficiency and vignetting as a function of φ . Even if it was not necessary to optimize the camera-collimator angle (for example if this were a physically fixed parameter as with most spectrographs), the relationship

between the average grating efficiency and φ would still be required. This is due to the fact that since the detector is two dimensional*, the different wavelengths travel along different φ angles to arrive at different x locations on the detector. As such, they will experience different grating efficiencies. This field dependent efficiency is factored into the transmission function and ultimately \mathcal{P} . The intrinsic $\Delta\varphi$ from the center to the edges of the detector can be computed (for the Bench Spectrograph Camera):

$$\Delta\varphi \cong \pm \tan^{-1} \left(\frac{w_{\text{CCD}}}{2 f_{\text{CAM}}} \right) \quad [39]$$

$$\cong \pm 4.93^\circ \quad [40]$$

So, the change in efficiency from one side of the CCD to other ($2\Delta\varphi$) is greater than that of moving the camera-collimator angle from 11° to 20° for all points on the detector.

7.1 THEORETICAL TREATMENT

The theoretical treatment of grating efficiency has taken great strides in recent years. It is now reasonable to expect that with modern techniques to predict the absolute efficiency at each operating point (given by m , d , α , φ , θ , and the polarization) to an accuracy on the order of 20%. θ is the field angle of the incident light to the grating. It is measured in the yz plane and is the cause of so-called conical diffraction, spectral line curvature, or diffraction distortion. The extreme field angle is found to be:

* Actually, as stated prior, it is 3 dimensional.

$$\theta_{\text{MAX}} = \pm \tan^{-1} \left(\frac{\bar{y}_{\text{FIB}}}{f_{\text{COL}}} \right) \quad [41]$$

$$\cong \pm 2.14^\circ \quad [42]$$

Since this is relatively small for this spectrograph, it is expected that the efficiency will not be field-dependent. The theoretical treatments will be done for $y = 0$ ($\theta = 0^\circ$) only and will then be checked with the experimental results.

7.1.1 Scalar Diffraction Theory

Scalar diffraction theory does not take into account the vector or polarization of the electromagnetic field. It assumes that an in-phase or planar incident wavefront strikes the blazed facets (only) of the grating surface and that the resultant diffracted wavefront may be determined by considering each portion of the blazed facets as a theoretical point source. Integrating the imaginary electric field contributions from all the point sources yields the magnitude of the real electric field which will be some fraction of the incident energy.

The larger the ratio of the facet geometry to the wavelength of light, the greater the expectation that this theory will match the actual performance. Both Bottema¹⁷ and Schroeder¹⁸ have good developments of grating efficiency based on the scalar diffraction theory. It is summarized this way. For the case of $\alpha > \beta$, as is with this spectrograph, the far-field phase difference in the diffracted wavefront, γ , can be found from the geometry to be approximately:

$$\gamma \cong \frac{\pi d}{\lambda} \frac{\cos(\alpha)}{\cos(\alpha - \delta)} [\sin(\alpha - \delta) + \sin(\alpha - \varphi - \delta)] \quad [43]$$

And, the efficiency or “blaze function” can then be found:

$$\epsilon_{G,SDT} \equiv \frac{\cos(\alpha)}{\cos(\alpha - \varphi)} \text{sinc}^2(\gamma) \quad [44]$$

The subscript SDT has been appended to ϵ to identify this as the scalar diffraction theory approximation. Note that no interdependence has been placed on α , λ , φ , δ , and d . This is because the blaze function traces out an envelope under which the peaks of the real orders (for which there are constraints for these variables) will lie. The following table demonstrates that it is reasonable to compute a representative average efficiency for one order only. Here, a linear sample of 10 wavelengths for three orders were chosen for analyses. An order is defined as going between the $m_{\text{OFF}} = m \pm 1/2$ points (see Figures 7-9). Although the spread in wavelength changes for different orders, the efficiency over a given order remains approximately equal, peaking, of course, in the center where $m_{\text{OFF}} = m$.

		φ_c	11.0°										
		d	3.1646 μ										
		δ	63.4°										
		m=7				m=10				m=13			
		λ	α	γ	ϵ	λ	α	γ	ϵ	λ	α	γ	ϵ
↑ One Order ↓		.7511 μ	62.068°	-1.47	34%	.5365 μ	63.883°	-1.42	35%	.4173 μ	64.933°	-1.39	36%
		.7626 μ	63.428°	-1.11	48%	.5421 μ	64.877°	-1.09	48%	.4206 μ	65.718°	-1.07	48%
		.7742 μ	64.842°	-0.77	59%	.5478 μ	65.901°	-0.77	58%	.4239 μ	66.523°	-0.77	57%
		.7858 μ	66.316°	-0.46	66%	.5534 μ	66.958°	-0.48	65%	.4273 μ	67.348°	-0.48	64%
		.7973 μ	67.863°	-0.17	68%	.5591 μ	68.052°	-0.20	68%	.4306 μ	68.197°	-0.21	68%
		.8089 μ	69.493°	0.09	67%	.5647 μ	69.188°	0.06	67%	.4340 μ	69.070°	0.05	67%
		.8204 μ	71.224°	0.32	63%	.5704 μ	70.372°	0.30	64%	.4373 μ	69.971°	0.29	65%
		.8320 μ	73.081°	0.51	57%	.5760 μ	71.610°	0.52	59%	.4406 μ	70.903°	0.52	60%
		.8435 μ	75.096°	0.67	51%	.5817 μ	72.911°	0.71	53%	.4440 μ	71.869°	0.73	53%
		.8551 μ	77.323°	0.77	45%	.5873 μ	74.288°	0.87	46%	.4473 μ	72.873°	0.92	47%
	.8666 μ	79.852°	0.80	39%	.5930 μ	75.757°	1.00	41%	.4507 μ	73.922°	1.08	40%	

Table 2, Representative Order for Scalar Theory

To determine the “average” efficiency over an order (for all wavelengths in the order) one should not simply average the efficiencies for all the (sampled) wavelengths from $m_{\text{OFF}} = m - 1/2$ to $m + 1/2$. There are three selection criteria that should be applied to filter out the impractical operating conditions. These impractical situations will simply never be used and should not influence the determination of average efficiency for all the usable configurations. The criteria are:

1. Situations of extremely high grating angle α will not be used due to the unacceptable vignetting at the grating. Even if the inherent grating (diffraction) efficiency is very good, if no light makes it through the spectrograph, the configuration is still useless. A value of 72° was chosen as this upper limit. The width of the Echelle projected onto a plane perpendicular to the collimator axis, w_{PROJ} , will be about 126 mm. Assuming an $f/6$ uniform fiber radiance pattern, the fraction of unvignetting at the grating, ϵ_v , will be:

$$D_{\text{COL}} = \frac{f_{\text{COL}}}{(f/\#)_{\text{FIB}}} \quad [45]$$

$$= 170 \text{ mm} \quad [46]$$

$$\epsilon_v \cong 1 + \frac{2}{\pi} \left\{ \frac{w_{\text{PROJ}}}{D_{\text{COL}}} \sqrt{1 - \left(\frac{w_{\text{PROJ}}}{D_{\text{COL}}} \right)^2} - \cos^{-1} \left(\frac{w_{\text{PROJ}}}{D_{\text{COL}}} \right) \right\} \quad [47]$$

$$\cong 85\% \quad [48]$$

This transmission formula has been derived from the vignetting geometry and does not include the effect of the centrally obscuring foot. The arc cosine term returns a value in radians.

2. If a significant fraction of the incident light strikes the back side of the blazed facet, it will tend to degrade the degree with which the diffracted beam will be in phase, lowering the efficiency and stretching the applicability of the scalar theory. A reasonable lower limit of 60.5% was chosen for the grating angle, α . This corresponds to 10% of the incident light hitting the back sides (Equation 36).
3. Low efficient configurations will not be used since, typically, there will be a higher efficient operating condition in an adjacent order. For example, near the wavelength boundaries between orders, it is possible to use either order by adjusting α and φ_c accordingly. The more efficient selection should be chosen. See Table 2 where for the $\varphi_c = 11^\circ$ case, these edge efficiencies are typically 35% and 40%. The first row in the table corresponds to the $m_{\text{OFF}} = m + 1/2$ edge and the last row corresponds to the $m_{\text{OFF}} = m - 1/2$ edge. Since all wavelengths, then, should be able to “see” a grating efficiency of better than 30%, efficiencies below this value will be rejected.

Plotting these selection criteria yields a resultant surface as a function of λ and φ .

An illustrative shape is given below for $m = 12$:

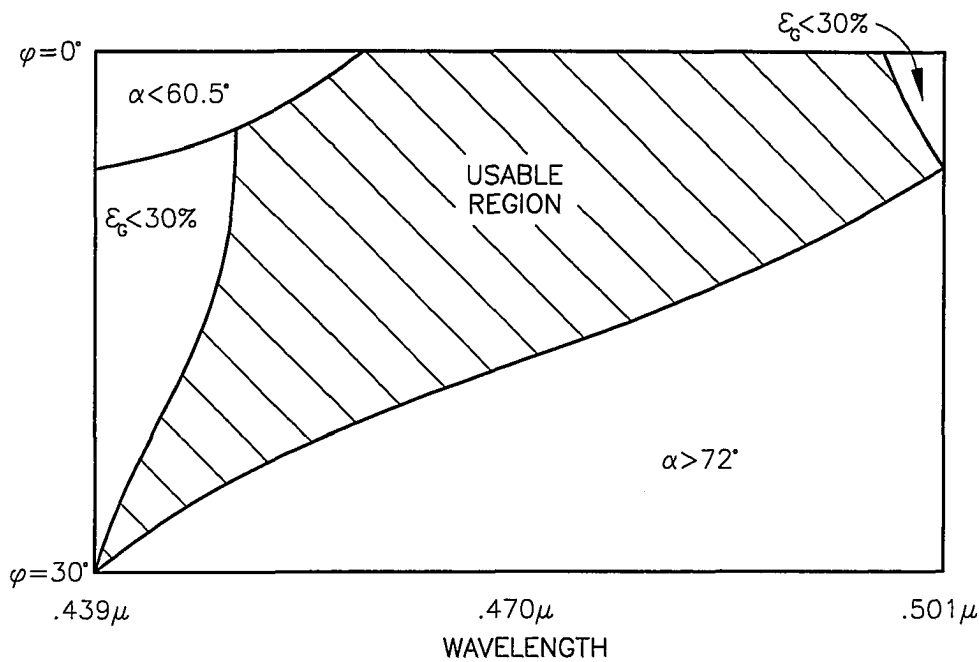


Figure 12, Scalar Efficiency Map

Note that the wavelength range extends blueward of $m_{\text{OFF}} = 12.5$ ($.451 \mu\text{m}$) and redward of $m_{\text{OFF}} = 11.5$ ($.490 \mu\text{m}$). This is because sometimes it will be prudent or necessary to work beyond the limit of being within a half order of the blaze condition. Really, what is at issue is whether or not the operating condition is efficient. The useful efficiency surface then is:

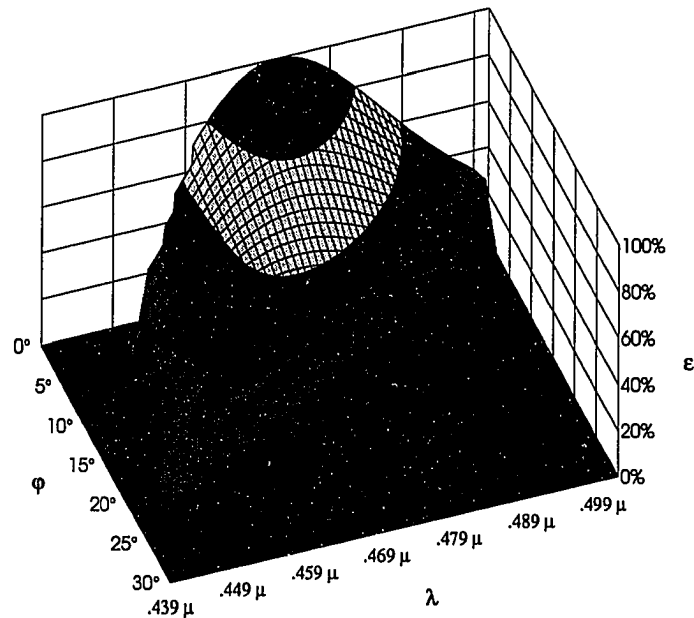


Figure 13, Scalar Efficiency Profile

Much can be gleaned from this plot. Note the lack of any subscripts for the vertical axis (efficiency). This is because the surface represents the individual efficiencies for all the wavelengths across an extended order, not the sought after average. For the Littrow ($\phi = 0^\circ$) condition, there is strongly peaked efficiency for the blaze wavelength (the center of the order). As ϕ is increased, this peak flattens and shifts to the blue. Note that there is a sub-region in the blue for which the optimal camera-collimator angle is non-zero and reaches as high as $\phi \cong 25^\circ$. Averaging the efficiencies across all wavelengths and rejecting the four forbidden zones yields $\epsilon_c(\phi)$ for the scalar diffraction theory:

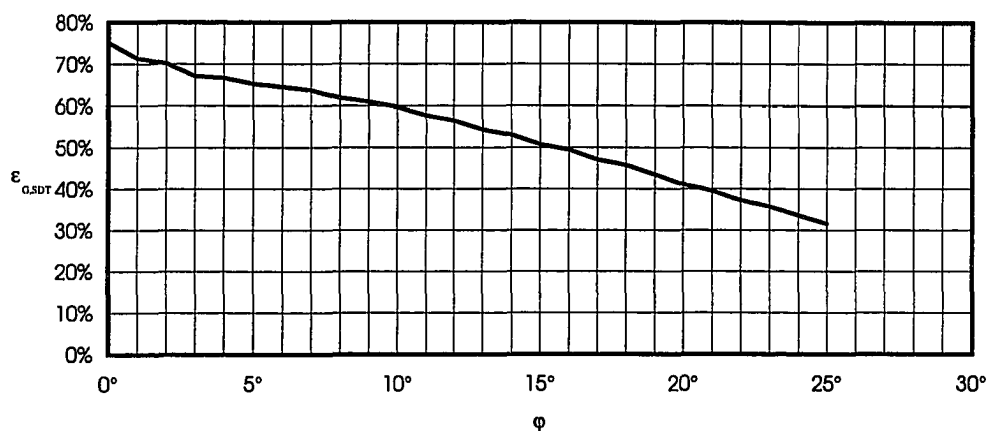


Figure 14, Average Scalar Efficiency

The result is the expected smooth monotonically decreasing grating efficiency. Note how the graph is devoid of data below $\epsilon_G = 30\%$, which corresponds to a camera-collimator angle of approximately 25° .

On a case by case basis, scalar diffraction cannot accurately model real grating efficiencies. However, it is the average (as determined above) efficiency, not any particular efficiency (for a wavelength) with which parameters of the spectrograph are to be evaluated. For, since the spectrograph is a general purpose instrument, it should be optimized to provide the best science without any regard to a particular wavelength.

7.1.2 New Developments

Since the development of scalar diffraction theory, a number of improvements have been made to the modeling of grating efficiency¹⁹. Here, notation for polarization varies widely. The notation adopted here is opposite some. Diffraction for no field ($\theta = 0^\circ$) lies in the xz plane. This will be called the plane

of diffraction. When the electric field disturbance is parallel to this plane, the notation will be p . When it is perpendicular to this plane, the notation will be s (the German word for perpendicular is *senkrecht*). Parallelism and perpendicularity are **not** with respect to the grooves.

The polarization, however, is not particularly important to the goal of modeling the grating efficiency and potential information gathering power of the spectrograph. The fibers emit light that is unpolarized and the grating is, for all intents, the only component of the instrument which has a strong dependence on polarization. If this were not the case, the efficiencies for the s and p polarizations would need to be carried out separately and then averaged at the detector. Fortunately, the polarizations can be combined at the grating, yielding ϵ_g that can then be combined into the transmission function.

All the following models are very complex and have a theoretical treatment beyond the scope of this work:

1. The so-called “Rayleigh theory” solved the boundary conditions of the electric field (polarization) at the grating surface based on Maxwell’s equations. It considered the propagation of exponentially decaying evanescent waves and is substantially better than the scalar theory. Its major drawback is the inability to accurately predict efficiencies for gratings with deep grooves, foremost of which is the Echelle.
2. The next step was the to tackle the issue of the scattering down inside the grooves themselves. A model based on surface

current density for a perfectly conductive surface proved to yield excellent prediction with the *s* polarization.

3. Finally, consideration was made to the real finite conductivity of the grating (in this case a thick aluminum layer). This was the first time that the Helmholtz reciprocity theorem was actually met. This implies that if the passage of a beam is reversed, the same efficiency is predicted.
4. Since then, a quantum mechanical model has been developed based on surface plasmons. Until this time, the models had been based on electromagnetic field theory. The quantum mechanical method is able to predict scattering effects due to surface roughness. The results are generally in agreement with the previous method.

7.1.3 Milton Roy Data

The grating used is a common large format astronomical Echelle. As such, E. Loewen has explored the theoretical efficiency of this grating using a refinement of the 3rd improved method listed (above), suited to the difficult case of Echelles. Earlier it was stated that the absolute accuracies of recent techniques are on the order of 20%. There are two primary reasons for this limit:

1. The actual profiles of the grating surface are not triangular with 90° apex angles. There are both systematic departures due to the manufacturing process and random “errors”.

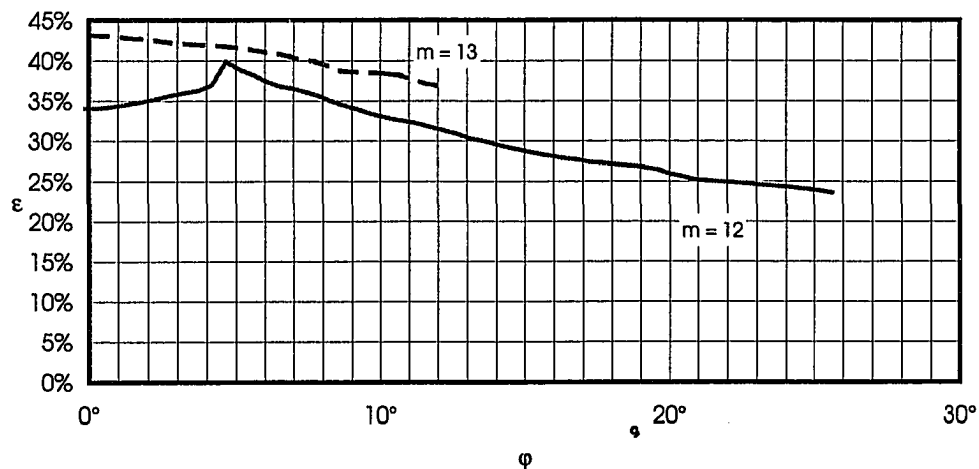
2. The aluminum coating is neither perfect nor equivalent to the textbook value for the complex admittance. In fact, an oxide layer has grown on the raw aluminum. This layer has been ignored.

In spite of this, the data is very good (limited, but certainly more accurate than the scalar modeling) and the author is indeed grateful for the privilege of using it and folding it into the overall model of grating efficiency²⁰. Like the scalar model, it is for the no field ($\theta = 0^\circ$) case. The data consists of theoretical efficiencies for seven wavelengths, covering the range of orders from $m = 13$ (blue) to $m = 10$ (red). The data was calculated as a function of the grating angle for the range $54^\circ \lesssim \alpha \lesssim 72^\circ$, less the ranges where the orders “pass off” or do not propagate. The limit at the high end matches that selected previously for the scalar diffraction theory. The low limit is so low that data is given for $\beta < \alpha$, *i.e.*, for $\phi < 0^\circ$ (marked by an asterisk, below). The spectrograph is not configured to work that way, although this is equivalent to mounting the grating upside down.

λ	m	From ϕ	To ϕ
.4416 μ	12	0 ^{o*}	25.7 ^o
"	13	0 ^{o*}	12.3 ^o
.4579 μ	11	2.5 ^o	32.2 ^o
"	12	0 ^{o*}	20.3 ^o
"	13	0 ^{o*}	3.6 ^o
.4726 μ	11	0 ^{o*}	28.2 ^o
"	12	0 ^{o*}	14.7 ^o
.4880 μ	11	0 ^{o*}	23.8 ^o
"	12	0 ^{o*}	7.9 ^o
.4965 μ	11	0 ^{o*}	21.2 ^o
"	12	0 ^{o*}	3.3 ^o
.5000 μ	11	0 ^{o*}	20.1 ^o
"	12	0 ^{o*}	1.1 ^o
.5145 μ	10	0 ^{o*}	29.6 ^o
"	11	0 ^{o*}	15.1 ^o

Table 3, Summary of Milton Roy Data

The first step was to recast the data in terms of ϕ , the author's choice as the independent variable. The data for the s and p polarizations have been averaged together. An example of the processed data for $\lambda = .4416 \mu\text{m}$ is shown:

Figure 15, Processed Milton Roy Efficiency Data for $\lambda = .4416 \mu\text{m}$

A linear interpolation on the data is made to provide the efficiencies at standardized values of φ , simplifying the averaging for all available wavelengths and orders. Again, before the averaging is performed, some filtering of the data is required. Since the Milton Roy data is for $\alpha \leq 72^\circ$ already, applying an upper limit to α will not be necessary. The lower limit of α is now meaningless as there is no problem, as with the scalar model, that this theory will break down when a non inconsequential fraction of the incident light hits the back side of the blazed facet. However, once again, efficiencies below some reasonable limit (again picked as $\epsilon_G = 30\%$) are rejected since the particular wavelength will be available in an adjacent order with a higher efficiency.

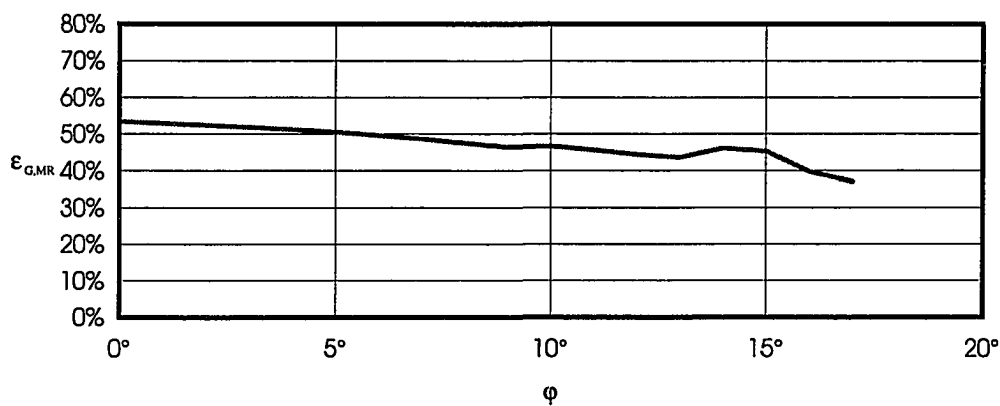


Figure 16, Average Grating Efficiency From Milton Roy Data

This plot also reveals a smooth, slowly decreasing efficiency as a function of φ . It has a slight non-monotonicity, which is probably due to the limited sampling at higher values of φ (see summary, Table 3).

7.2 BENCH SPECTROGRAPH DATA

In addition to modeling the average grating efficiency with the two theoretical models, data were taken with the instrument itself. In Section 7.3, these data will be combined to form the best estimate of the actual efficiency.

7.2.1 Description

During June, 1993, the Bench Spectrograph was configured in the high resolution mode for the purpose of determining an experimentally derived average grating efficiency. The Echelle grating was employed at $m = 10$ and an interference filter designated X16 was used for order separation. The Simmons Camera was used and data was taken for a range of camera-collimator angles. In order to simplify the data reduction, several steps were made to make the vignetting function more consistent:

1. The collimator was blocked on either side of a 100 mm wide aperture. This was done so that vignetting would not occur at the grating (for the largest grating angle).
2. The spatial asymmetry at the foot was eliminated by extending a 13 mm wide mask in the $-y$ direction there as well.
3. The grating to objective distance, L_1 , was set for the lowest camera-collimator angle and not allowed to shrink for larger ϕ_c .
4. An elliptical mask usually employed at the entrance aperture of the Simmons Camera was removed.

The technique used to gather the data was as follows. The camera-collimator angle was set to $\varphi_c = 12^\circ$ and incremented twice to 14° and 16° . At each camera-collimator position, the grating angle was changed to provide three wavelength regions. These are designated as “blue”, “mid”, and “red”. The grating angles were chosen so that the blue wavelength regions for $\varphi_c = 12^\circ$, 14° , and 16° were centered at very close to the same wavelength. The same was done for the mid and red wavelength regions.

For each combination of φ_c and wavelength region, different polarizations were investigated. This was accomplished by either placing one of two polarizing filters directly behind the interference filter or nothing at all. The (collimator) focus was not adjusted to compensate for the thin polarizers.

In each case, a flat field image was acquired to determine the flux. At the time, the fiber positioner was not attached to the Kitt Peak Mayall 4m telescope. Rather, it sat in its laboratory/storage location and. By opening up the top of the fiber positioner and turning on the normal incandescent room lights, reasonable spectra of a quasi black body distribution were recorded. Each set of flat field spectra was integrated for 200 seconds.

In addition to taking flat fields for the three polarizations at each φ_c and wavelength region, comparison spectra were recorded. A diffusing white screen was placed in front of the fibers, the room lights were turned off and the screen was illuminated with 6 Thorium-Argon hollow cathode arc lamps. These lamps produce many well-known spectral emission lines. These allowed precise identification and calibration of wavelength across the CCD. In fact, since the camera-collimator angle could only be set to an accuracy of approximately $.3^\circ$, the

three wavelength regions exhibited slight shifts in the locations of their emission lines from one camera-collimator angle to the next. So, the grating angle was adjusted slightly for the $\varphi_c = 14^\circ$ and 16° cases from the nominal theoretical value to match the locations of these lines for $\varphi_c = 12^\circ$. This was done so as to insure that the same wavelengths were available in the same region for each φ_c . The spectral radiance from these lamps is not as high as that from the flat field lights, so the integration time was increased to 20 minutes to achieve a high SNR.

φ_c	Blue		Mid		Red	
	Theory	Actual	Theory	Actual	Theory	Actual
12°	68.369°		69.416°		70.903°	
14°	69.630°	69.673°	70.645°	70.733°	72.093°	72.216°
16°	70.927°	70.851°	71.912°	71.927°	73.327°	73.411°

Table 4, Wavelength Regions

7.2.2 Data Reduction

The first step in reducing the data was to extract the spectra. A typical line or row plot for a flat field is shown following. It is along y and shows the processed irradiance from each fiber .

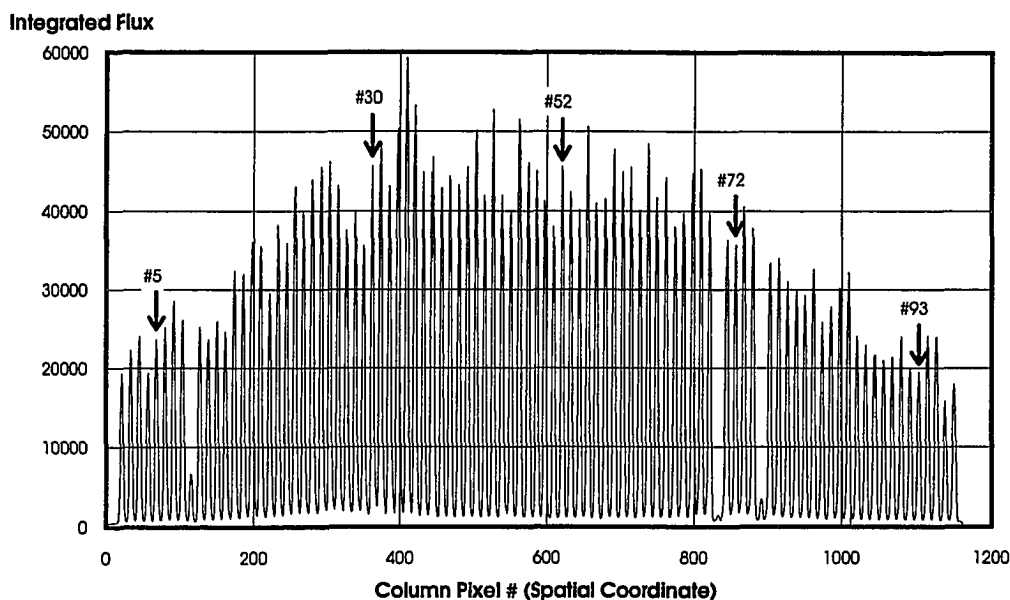


Figure 17, Row Plot for $\varphi_c = 14^\circ$, Mid Region, *s* Polarization

Here, the flux from 10 rows (Lines 1019 to 1028) has been summed together. There are 97 fibers (counting left to right). No field ($y = 0$) is located at approximately fiber #47. The only processing in this cut through the spectra is bias removal. There are three bad fibers (#9, #70, and #75). Note the overall vignetting pattern for the system. The irradiance for the extreme field drops to roughly half that at $y = 0$. So that the efficiency as a function of field (conical diffraction) could be studied, five fibers were selected for extraction. These are marked by arrows and their fiber numbers are indicated.

There are two criteria for this selection. The fibers should be spread out as evenly as possible with symmetry about $y = 0$ and they should be representative of the average vignetting function. The high frequency deviation from the smooth vignetting function is due to the fiber-to-fiber transmission disparities. These have

a standard deviation on the order of (\pm) 11%. A further development of the field dependence is found in Section 7.2.4.

About each of these 5 apertures, the flux was integrated across the peak in the spatial direction (from the valleys between fibers) along the x^* or spectral direction yielding spectra. Next, a smoothing function was applied to the data since the black body distribution is a low order function. The higher frequency irregularities come instead from photon noise and pixel variations. A typical result is shown below:

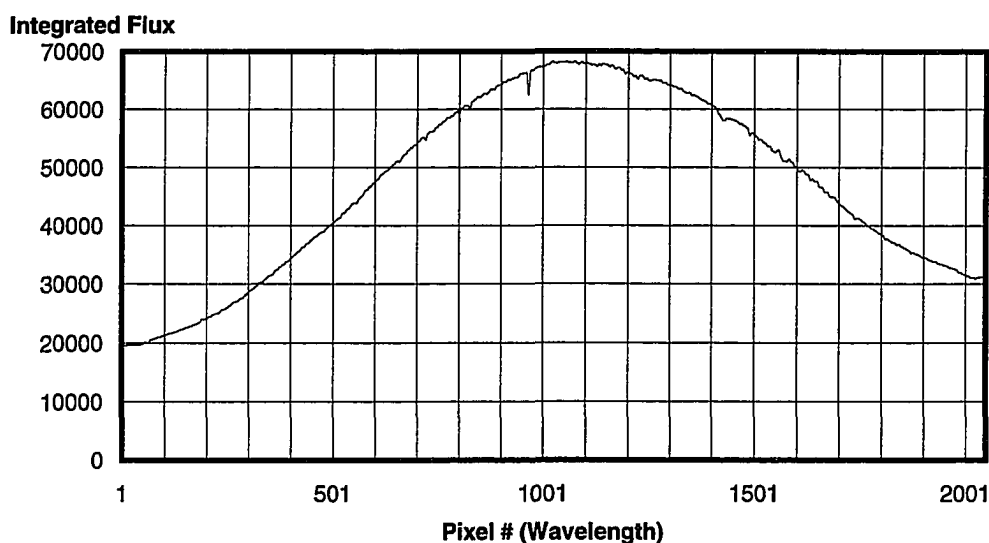


Figure 18, Typical Flat Field Spectrum

Some low-level pixel-to-pixel variance is still evident. The half dozen or so depressions from the smoothly varying flat field are a result of absorption bands due to impurities in the particular fiber. Special care is required to fit the general

* Actually, the tracing follows the conically distorted peak.

distribution when data is required from within these absorption bands. Not apparent in this spectrum are two other anomalies, cosmic rays and “hot” columns. Reasonable attention is given to these as well.

For the wavelength calibration data, emission line spectra were extracted for the same 5 apertures. An atlas of such emission lines was used to identify the peaks. Since α was adjusted for the $\varphi_c = 14^\circ$ and 16° cases, the wavelength scales were very close for each camera-collimator angle. The scales were, of course, shifted for the three wavelength regions. Then, 8 strong emission lines corresponding to 8 wavelengths, which are roughly evenly spaced out in the mid wavelength region, were selected to have their efficiencies evaluated. There is some overlap of these wavelengths in both the blue and red wavelength regions (6 each). For a given φ_c , turning the grating angle for each region causes the chosen wavelengths to traverse a different φ on their way to being imaged. Hence, they will experience up to three different grating efficiencies for each φ_c .

Wavelength Ranges		
Blue	Mid	Red
.5539 μ	.5539 μ	
.5558 μ	.5558 μ	
.5587 μ	.5587 μ	.5587 μ
.5615 μ	.5615 μ	.5615 μ
.5640 μ	.5640 μ	.5640 μ
.5665 μ	.5665 μ	.5665 μ
	.5701 μ	.5701 μ
	.5720 μ	.5720 μ

Table 5, Selected Wavelengths

Due to conical diffraction, the mapping of wavelength across the CCD will vary for each of the five apertures (fibers). The task is now to determine the efficiency

for each of these 8 wavelengths as a function of ϕ given y and the polarization. Then the best grating efficiency for the Bench Spectrograph, $\epsilon_{G,BS}$, data can be found by combining the efficiencies for the 8 individual wavelengths. For the moment, the case of no field ($y = 0$) and no polarization will be considered.

The knowledge of where (pixel number) each wavelength occurs on the flat fields yields the raw integrated flux for the wavelength in question. However, in order to compute the efficiencies, the raw flux must be first normalized by the vignetting. This is because the amount of vignetting will change over the 2 dimensional field and with camera-collimator angle. The latter dependence is a result of the anamorphic factor. The beam width along the camera axis, w_{CAM} , varies with the anamorphic factor, which in turn varies with α and ϕ . There are, however, some simplifications that can be taken advantage of in computing the vignetting:

1. Spatial symmetry ($\pm y$) dictates that the vignetting will be mirrored about the $y = 0$ center line of the detector.
2. Empirically, the vignetting functions at each ϕ_c for the three wavelength regions (values of α), are within 1% for all field (y) values. This was determined by using the “canned” vignetting routine of the optical design program Zemax* to find the amount of vignetting for a model of the spectrograph for different conditions. Since the data were acquired at the 4m telescope (*cf.*, the WIYN telescope), the fibers nominally produce a fiber radiance distribution where 90% of the energy is within an $f/6.7$

* A product of Focus Software Incorporated, Tucson, AZ

cone. So, a uniform distribution out to this value is assumed. At $\varphi_c = 12^\circ$, the vignetting was computed for a sample of 6 equally spaced wavelengths starting from the center of the detector ($\varphi = 12.00^\circ$) to the blue edge ($\varphi = 15.70^\circ$) for each wavelength region. This was done for 11 values of y (from 0 to \bar{y}_{FIB} or 38.1 mm). The three resulting sets of percent unvignetting were averaged together and the deviations computed from the average. Deviation is defined as the average amount of unvignetting less the amount for the specific wavelength region. The following is a typical plot of these showing the deviation for the $\varphi_c = 12^\circ$ mid wavelength region. Each series is one of 6 different wavelengths, representing a spectral (or x) position on the CCD. As a result, for each φ_c , the same vignetting function is used for the three wavelength regions.

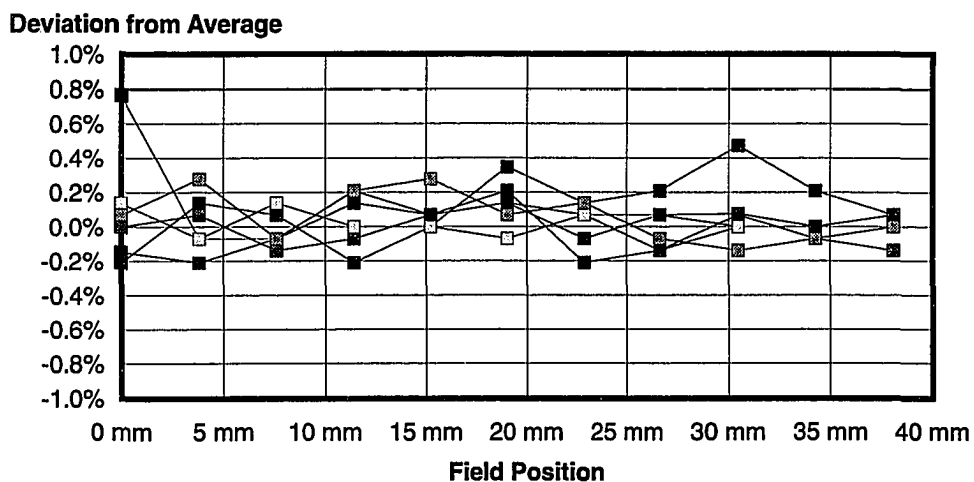


Figure 19, Region to Region Vignetting Deviation

3. Empirically, the vignetting function from the center of the detector ($\varphi = \varphi_c$) to the blue edge is within 1% the same as that from the center to the red edge. There is a systematic error associated with the change in anamorphic factor, but it is small. For example a typical deviation for 6 wavelengths equally spaced from the center of the detector to the red edge (from the average of this and two other regions with 6 wavelengths equally spaced from the center to the blue edge) is shown below. It is for the $\varphi_c = 14^\circ$ mid wavelength region with $\varphi < \varphi_c$:

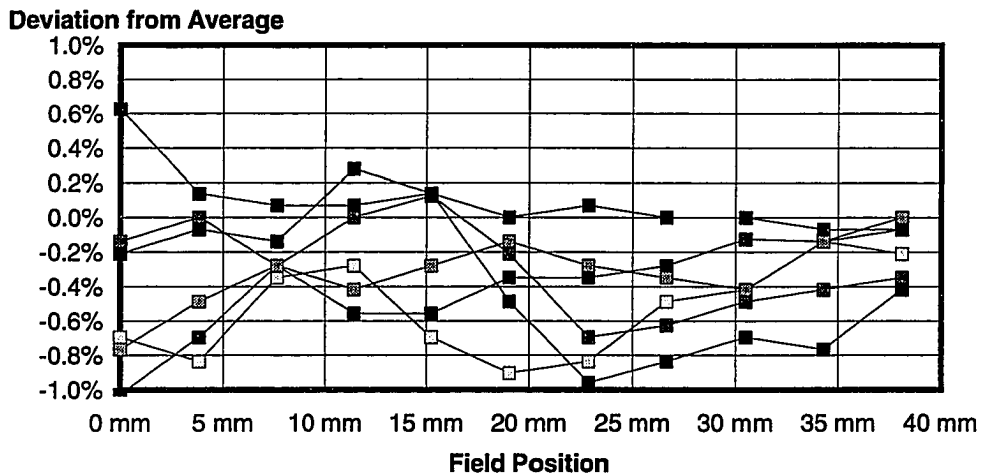


Figure 20, Red to Blue Side Vignetting Deviation

Notice the general trend to below average ($< 0\%$ deviation). This is because the red side of the detector ($\varphi < \varphi_c$) has a lower anamorphic factor than the blue side. The beam is more compact and experiences less vignetting. However, since the

deviation is small, the same vignetting function is applied to both the red and blue sides folded about φ_c .

Now the normalized flux (Norm) can be computed from the raw integrated flux of the flat field spectra (Flux). The following table shows this calculation for the $\varphi_c = 12^\circ$ mid wavelength region. Since the vignetting normalization is independent of polarization, the calculation is done for all polarizations. The column labeled $|\varphi|$ is not the absolute angle of φ . Rather, it is the angle folded about φ_c so there are only angles greater than φ_c . This is to take advantage of the third simplification for computing the vignetting function, denoted VF:

$$|\varphi| = \varphi, \varphi \geq \varphi_c \quad [49]$$

$$|\varphi| = \varphi_c + (\varphi_c - \varphi), \varphi < \varphi_c \quad [50]$$

φ	$ \varphi $	VF	Unpolarized		<i>s</i> Polarized		<i>p</i> Polarized	
			Flux	Norm	Flux	Norm	Flux	Norm
14.60°	14.60°	22.9%	28792	125532	9331	40683	3475	15151
13.98°	13.98°	29.2%	38760	132581	12388	42374	4863	16634
12.98°	12.98°	40.3%	57323	142225	18097	44901	6908	17140
12.08°	12.08°	45.6%	67375	147659	20585	45114	8477	18578
11.32°	12.68°	43.5%	65860	151395	19166	44058	8994	20675
10.45°	13.55°	33.9%	57966	171149	15672	46273	8579	25330
9.19°	14.81°	21.1%	38377	182080	9305	44148	6326	30014
8.48°	15.52°	18.1%	31516	174461	7192	39812	5438	30103

Table 6, Typical Normalized Flux Calculation

When the previous calculation is done for all three values of φ_c and all three wavelength regions, the resultant normalized flux as a function of φ can be determined. A plot for the most general case of no field ($y = 0$) and no polarization is shown. Each series is one of 8 wavelengths and is displayed as a

set of connected squares. There are either 6 or 9 points in each series. This depends on the number of regions (2 or 3) over which the wavelength was available (see Table 9). As is the case with the theoretical data, the trend for any given wavelength (series) is unimportant. It is the aggregate of all wavelengths which represents the average grating efficiency. And once again, the trend is a smoothly monotonically decreasing efficiency function.

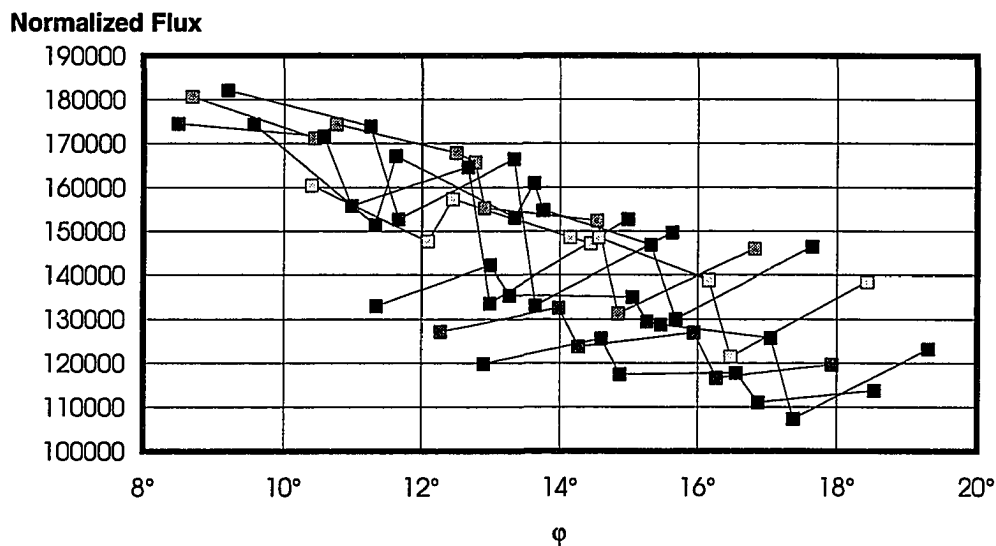


Figure 21, Bench Spectrograph Unpolarized Efficiency Function

7.2.3 Polarization

Although the main thrust of this thesis is unconcerned with the polarization, the setup has allowed polarization data to be acquired. Here is a brief summary of the experimental results. It is generally considered that the *s* polarization behaves more scalar like. The following figure shows the efficiency function for the *s* polarization data (again, $y = 0$). The vertical axis has been expanded so that the

trend as a function of wavelength may be seen. There are 8 wavelengths plotted as distinct data series in the order listed in Table 6. The series marked Start is the bluest wavelength (.5539 μm). The arrows designate the next wavelength in the sequence of 8. The sense of the arrow (upward or downward) shows the trend in efficiency from one series (wavelength) to the next. The wavelength given at the top is that for the series exhibiting the highest efficiency, from which the arrows point down to both the blue and the red.

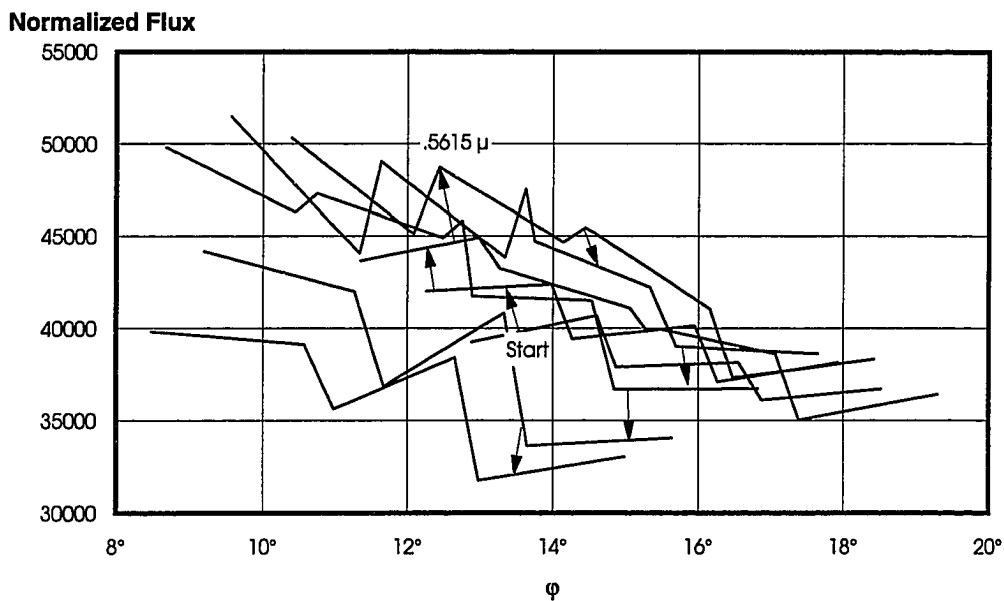


Figure 22, Bench Spectrograph s Polarization Efficiency Trend

For the s polarization, the wavelength series with the highest efficiency is .5615 μm . This is amazingly close to that predicted from the scalar theory. The blaze wavelengths ($m_{\text{OFF}} = m$) are .5628 μm , .5617 μm , and .5604 μm for $\phi = 12^\circ$, 14° ,

and 16° respectively. So, the measured peak efficiency for the s polarization is right where predicted by the scalar theory.

There are two major changes with the p polarization. First the efficiency is on the order of half as much as with the s polarization. Secondly, the peak shifts redward in wavelength:

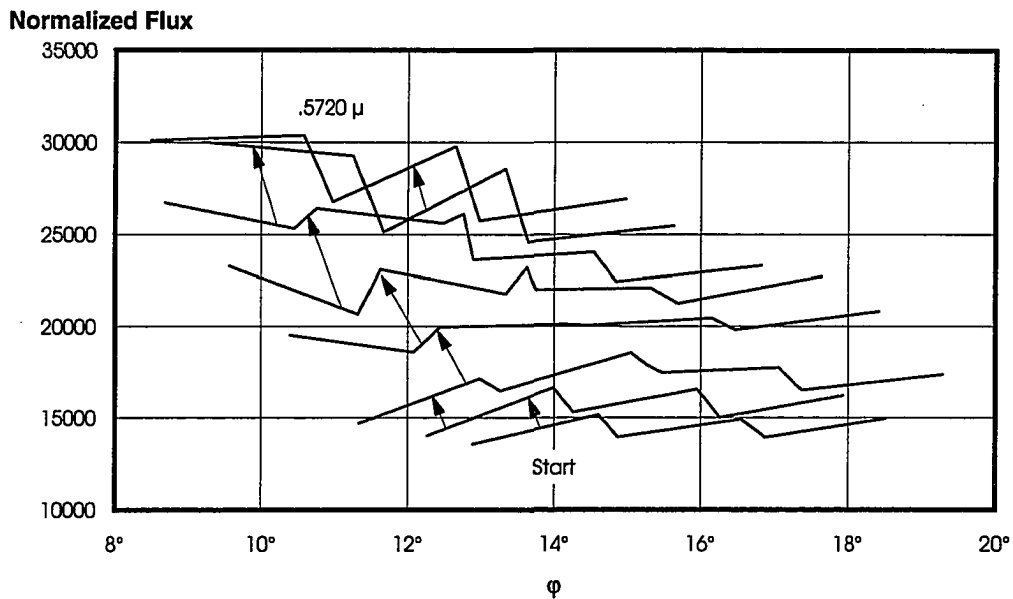


Figure 23, Bench Spectrograph p Polarization Efficiency Trend

A possible interpretation of this phenomenon is that p polarization “sees” a rougher or steeper surface than the s polarization. Equation 34 can be re-written to solve for the blaze angle, δ :

$$\delta = \sin^{-1} \left[\frac{m\lambda}{2d \cos(\phi/2)} \right] \quad [51]$$

For the *s* polarization case, substituting in the peak series wavelength (.5617 μm) into this equation yields the actual blaze angle ($\cong 63.4^\circ$ average for $\phi = 12^\circ, 14^\circ,$ and 16°). For the *p* polarization case, the computed blaze angle increases to $\cong 65.6^\circ$, which represents a steeper surface. Conceptually, this agrees with the principle that for the *p* polarization, the free electrons in the conduction band of the grating surface have a more difficult task of vibrating perpendicularly to the grooves.

The unpolarized case lies in between the two polarizations:

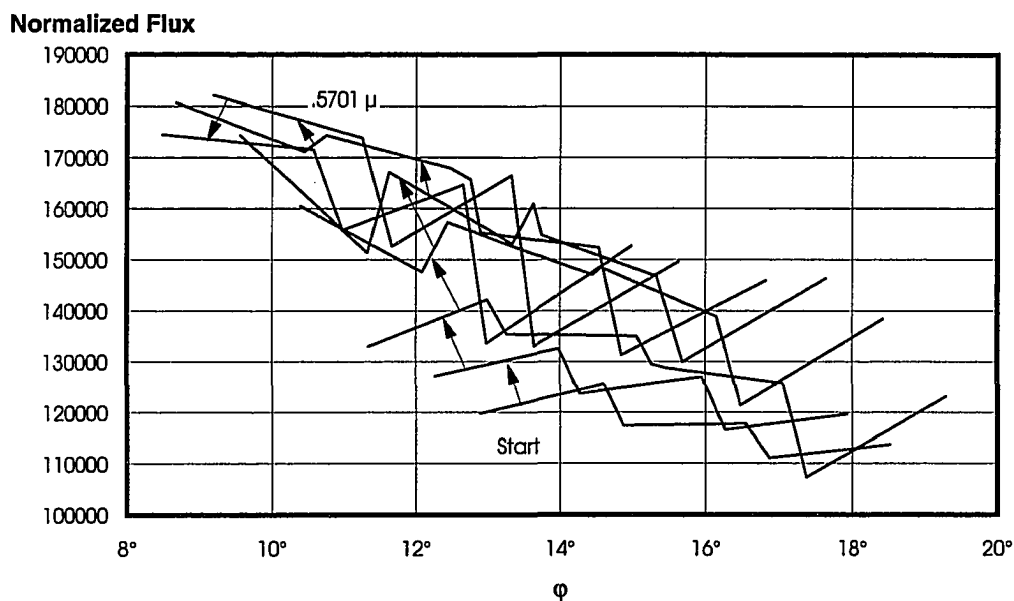


Figure 24, Bench Spectrograph, Unpolarized Efficiency Trend

7.2.4 Conical Diffraction

One of the questions that should be answered is the degree to which the grating efficiency is field independent. Certainly it is expected that with the shallow field angles involved (Equation 42), the average grating efficiency, which in the most general case is both a function of φ and y (or θ), can be simplified:

$$\varepsilon_G(\varphi, y) \rightarrow \varepsilon_G(\varphi) \quad [52]$$

There are two methods that were employed to test this simplification:

1. The same data reduction technique used to derive the efficiency for the $y = 0$ case was applied to other field positions (apertures) as well.
2. Data were extracted from the unpolarized flat field spectra from a series of 6 new line plots (cuts across spectra). Without applying any vignetting normalization, the shapes of the resultant efficiency plots (as a function of φ) are compared for three field positions.

For the first method, the following table summarizes the five apertures previously selected (see Figure 17):

Fiber #	Apx Field Pos (Object)	Symmetrical	Apx Field Pos (Image)	CCD Column Center
5	-34.3 mm	33.5 mm	-12.8 mm	68
30	-15.2 mm	16.0 mm	-5.7 mm	362.5
52	1.5 mm	0 mm	.6 mm	621
72	16.8 mm	16.0 mm	6.2 mm	856.5
93	32.8 mm	33.5 mm	12.2 mm	1103.5

Table 7, Field Position Summary

Due to the fiber-to-fiber spatial variations, the aperture positions approximately symmetrical about $y = 0$ are combined and assumed to have object positions equal to the average of the absolute values of the two component apertures (column labeled Symmetrical). This was done to “beat down” the effects of the spatial variations. The goal is to model the off (spatial) axis vignetting and compute the efficiencies for these two averaged spatial dimensions ($y = 16.0$ mm and 33.5 mm).

Data were extracted in the same fashion, using the canned vignetting routine evaluated for the appropriate field values. Next three numerical fits to these data were made (see Section 7.3).

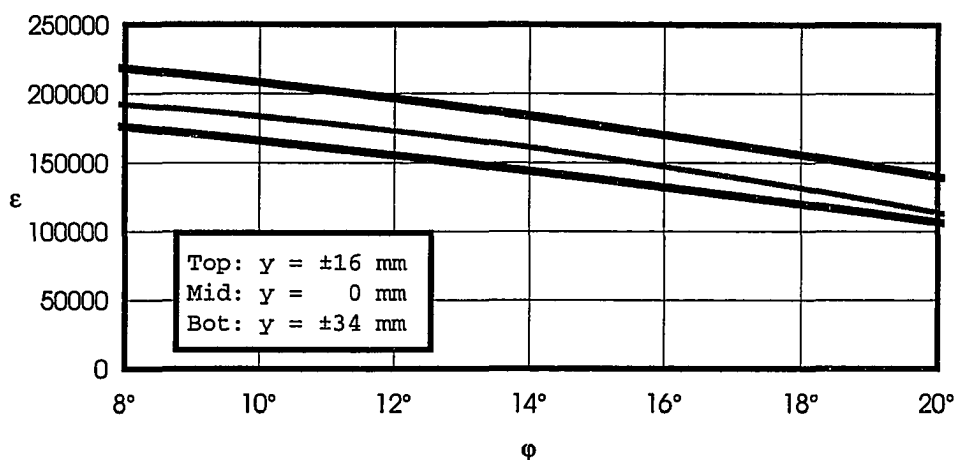


Figure 25, Average Efficiency for Three Fields, Not Normalized

There is a fair amount of scale shift within these curves. This is due to two primary reasons. First, the apertures selected (Figure 17) do not exactly follow the overall vignetting function. Simple inspection reveals that the average of the peaks of the fibers half-way between the central and edge fibers is above the overall vignetting function. This is precisely what is evident in the figure above. The second reason for the scale variation has to do with imperfection of the canned vignetting function in modeling the actual fiber radiance distribution (see below). However, it is noteworthy that the three efficiency curves have the same shape. They are re-scaled and plotted below:

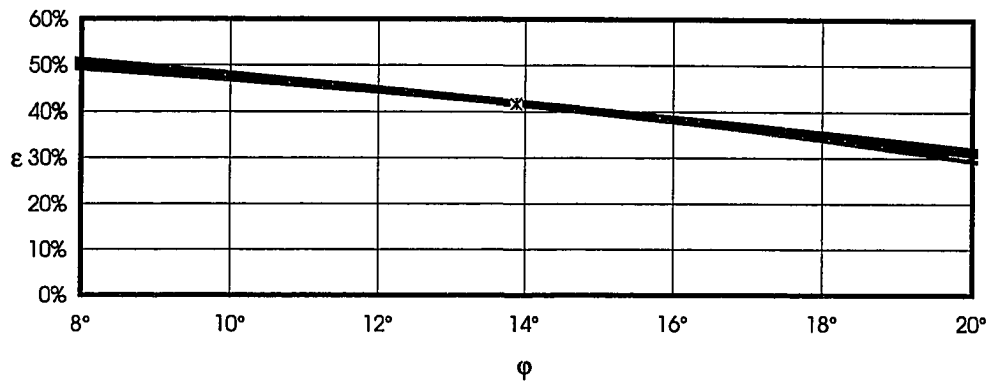


Figure 26, Average Efficiency for Three Fields, Normalized

Here, the individual curves are barely distinguishable. The scaling factors for each numerical fit were chosen so that centroid of each data set had the same efficiency as that for the scalar data. This normalization will be utilized later in Section 7.3.

In effort to eliminate the effects of imperfect modeling of the canned vignetting routine, another approach was explored. Here, 6 new line plots were extracted from the flat fields for three unpolarized mid wavelength regions. The line numbers over which the raw flux was integrated were chosen to correspond to the six $\phi = \phi_c \pm .5^\circ$ zones:

Source ϕ_c	10 Lines Summed		Yields ϕ
	From	To	
12°	881	890	11.5°
12°	1157	1166	12.5°
14°	881	890	13.5°
14°	1157	1166	14.5°
16°	881	890	15.5°
16°	1157	1166	16.5°

Table 8, Summary Data for 6 Line Plots

Since the three wavelength regions are very nearly the same, the odd numbered rows in the above table represent one wavelength and the even numbered rows another. The next step was to fit a low order function through each line plot. After some experimentation, a good fit was found to be the combination of two identical Gaussians mirrored about the $y = 0$ point:

$$\epsilon_{\text{FIT}} = A e^{-\frac{[y_{\text{PIX}} - (y_{\text{CENT}} - y_{\text{OFF}})]^2}{2\sigma^2}} + A e^{-\frac{[y_{\text{PIX}} - (y_{\text{CENT}} + y_{\text{OFF}})]^2}{2\sigma^2}} \quad [53]$$

Where A is the amplitude, y_{PIX} is the column number, y_{CENT} is the center of the distribution where $y = 0$, y_{OFF} is the offset of the 2 Gaussians from the center, and σ is the width parameter. The best fit was determined numerically. An example for the $\varphi_c = 12^\circ$ case for lines (column pixel numbers) 881 to 890 follows:

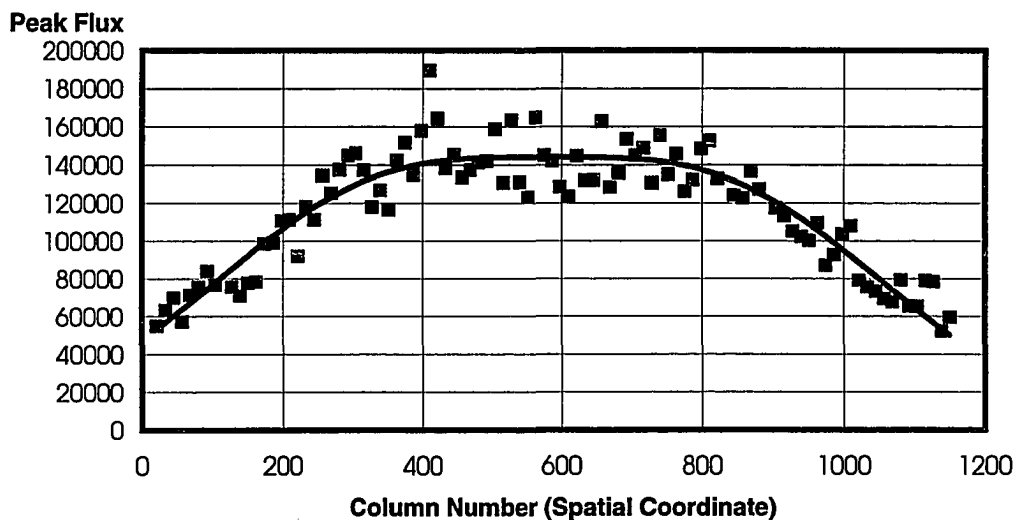


Figure 27, Typical Numerical Fit to Vignetting Function Along y

The individual squares are the locations of the peaks of the distributions from the fibers. Data from the three bad fibers was rejected. Each peak flux was determined by fitting the best parabola to the middle 4 spatial pixels for each fiber's distribution. Now the spatial dependence of efficiency can be determined without relying on any particular fiber (and its peculiar characteristics). Instead, the overall vignetting function (given by the solid line) will be used. After, numerical fits were made for each of the 6 cases, they were evaluated at the same three field positions as done earlier. Finally, the $y = \pm 16.0$ mm and ± 33.5 mm curves were normalized to the $y = 0$ mm case to see if there is any change in the **shape** of the efficiency as a function of y (or θ):

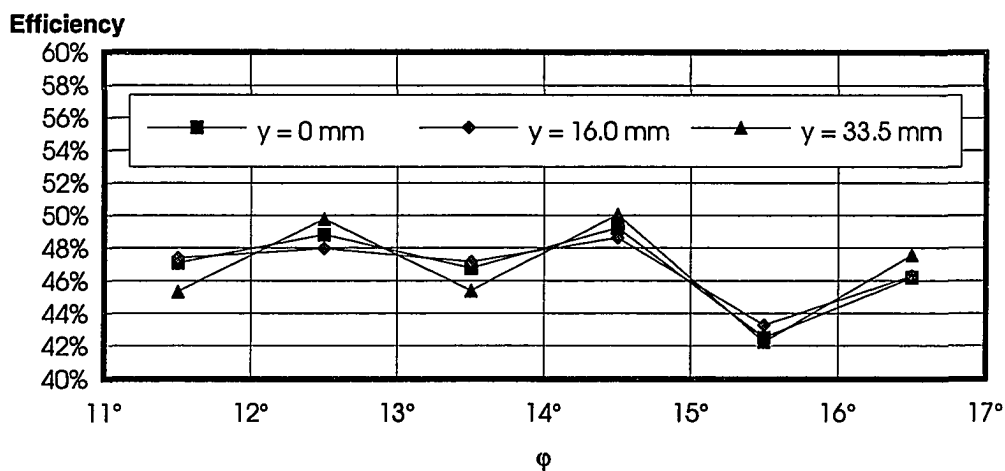


Figure 28, Efficiency, Experimental Vignetting Normalization

Since only a minimum number of wavelengths (2) and camera-collimator angles (6) were used, one should not place any relevance on the general trend of these efficiency functions (fairly flat). Rather, it is that the shape does not change as a

function of the field variable that is important. The variance is a few percent, well within the experimental errors.

Both methods show that for the mild field angles involved, the shape of the average efficiency as a function of φ is the same. Unfortunately, although consistent with this determination and certainly likely, the lack of an overall shift as a function of the field variable in the average efficiency is not proven. Mathematically, it is unlikely, though possible for the average efficiency to have a field dependent term that is separable from the diffraction angle dependent term:

$$\varepsilon_G(\varphi, \gamma) \stackrel{?}{=} g(\varphi) \cdot h(\gamma) \quad [54]$$

7.2.5 Results

A more careful modeling would permit absolute normalization of the vignetting function. As it is, two assumptions have been made in this regard:

1. The fiber radiance distribution is a uniform distribution out to an angle corresponding to an $f/6.7$ (4m telescope) beam speed. This was checked with a model of the focal ratio degradation based on the theory of modal diffusion^{21,22}. The following example illustrates the quality of this assumption. The technique employed was to utilize the data published by Barden²³ to solve for the fiber parameter that characterizes microbending, d_0 . For a 25 m length 300 μm diameter fiber, fed with an irradiance

distribution corresponding to that at the 4m telescope, the following theoretical fraction of collected output within a given $f/\#$ was determined for $d_0 = 17.8 \text{ m}^{-1}$:

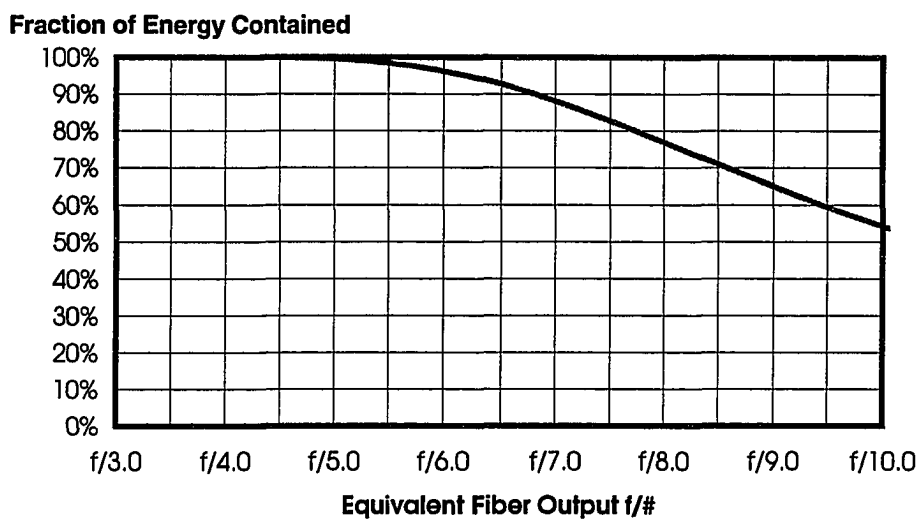


Figure 29, Integrated Fiber Radiance

Note that there is 90% of the emitted energy collected within the $f/6.7$ cone angle. The input (to the fiber) and output (from the fiber) distributions for this case are modeled to be:

Relative Irradiance and Radiance

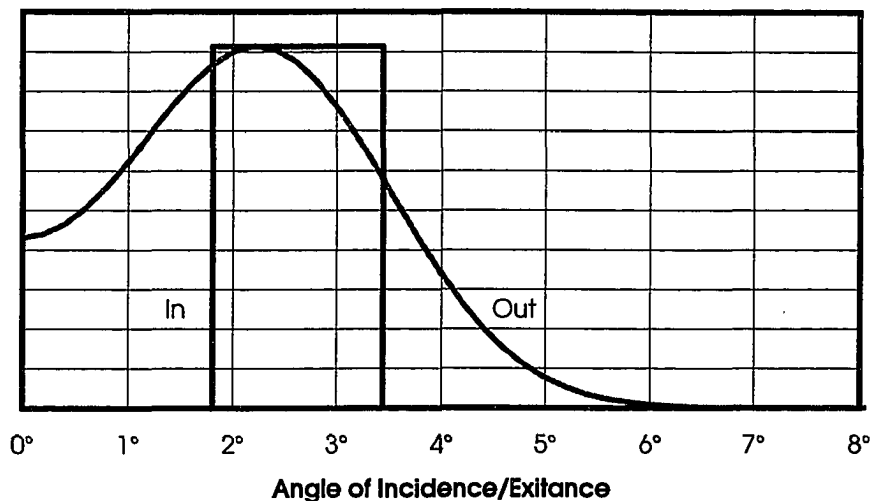


Figure 30, Fiber Modal Diffusion

The plot is rotational symmetric about the line where the angle of incidence is equal to zero. The rectangular distribution is the feeding beam of the telescope. It is uniform from the secondary shadow out to the marginal ray given by the usable aperture of the primary mirror. The curved distribution represents the modal diffusion or focal ratio degradation of the fiber. A perfect uniform distribution equivalent to $f/6.7$ would be a rectangular distribution with the rightmost edge at 4.3° .

2. The second assumption is that the experimental set-up was approximately the same as that for telescope, yielding a uniform $f/6.7$ fiber radiance distribution. The illumination scheme involved allowing the fibers to “see” the available incandescent

lighting and the rest of a white ceiling. This is difficult to model.

As it is, the shape of the derived efficiency function is really what is important. And, this is measured with confidence to approximately $\pm 5\%$ within the region of interpolation. The shape for the off (spatial) axis is the same as that on-axis and it will be assumed that there is no uniform departure from the on-axis average efficiency for the field angles involved.

A concern with utilizing the derived shape of the efficiency function is that it is not overwhelmed by large systematic errors. There are two systematic errors which should be described:

1. The first systematic error is a result of two phenomena. The flat field is not perfectly flat (*i.e.*, uniform with respect to wavelength) and the sampling of φ in the data contains a slight bias with respect to wavelength. As a result, the efficiency has a bias with respect φ . There are three reasons for the non-uniformity of the flat field. The first is that the black body distribution of standard incandescent lighting is not even. The product of the filament temperature dependent spectral radiance and filament emissivity has a color temperature of approximately 2800 K. The second reason is that the fibers themselves have a wavelength dependent transmission. Finally, the interference filter has a wavelength dependent transmission. When these three effects are combined, the resultant flat field is:

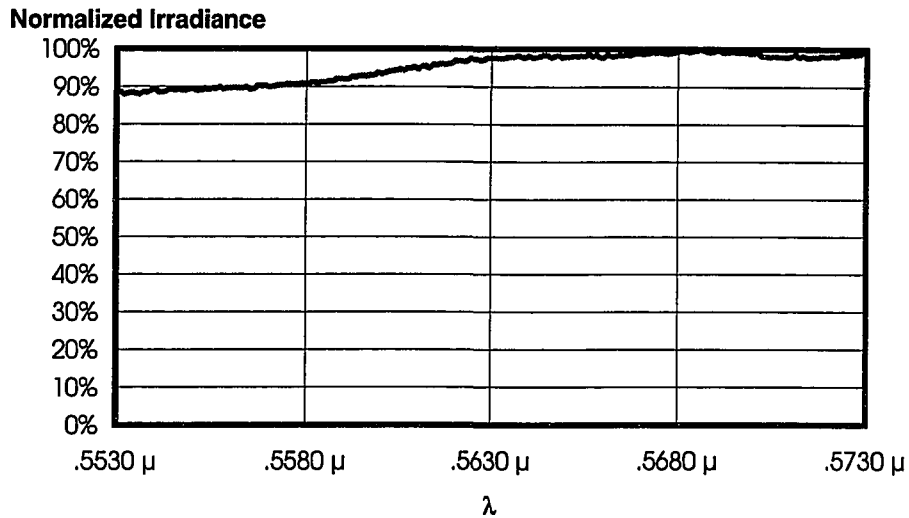


Figure 31, Flat Field Distribution

The wavelength range was chosen to match the data in the previous section. The following table summarizes the 8 wavelengths that were used and the corresponding camera-collimator angles from which the flux was acquired:

		Wavelength							
		.5539 μ	.5558 μ	.5587 μ	.5615 μ	.5640 μ	.5665 μ	.5701 μ	.5720 μ
φ ↓		12.89°	12.27°	11.34°	10.40°	9.56°	8.68°		
		14.87°	14.27°	13.26°	12.44°	11.63°	10.76°		
		16.87°	16.27°	15.26°	14.44°	13.63°	12.76°		
		14.60°	13.98°	12.98°	12.08°	11.32°	10.45°	9.19°	8.48°
		16.55°	15.95°	15.05°	14.14°	13.34°	12.48°	11.26°	10.57°
		18.52°	17.93°	17.05°	16.15°	15.32°	14.53°	13.33°	12.65°
				15.47°	14.56°	13.75°	12.89°	11.67°	10.98°
				17.37°	16.47°	15.69°	14.85°	13.64°	12.98°
			19.30°	18.42°	17.64°	16.82°	15.63°	14.98°	
	AVG	15.72°	15.11°	15.23°	14.35°	13.54°	12.69°	12.45°	11.78°
	Irradiance	89%	89%	91%	96%	98%	98%	99%	98%

Table 9, Data Set of Camera-Collimator Angles

If the normalized (to 100%) flat field irradiance is then plotted as a function of ϕ , a bias is evident that reduces the efficiency of higher camera-collimator angles approximately 10% over the region employed:

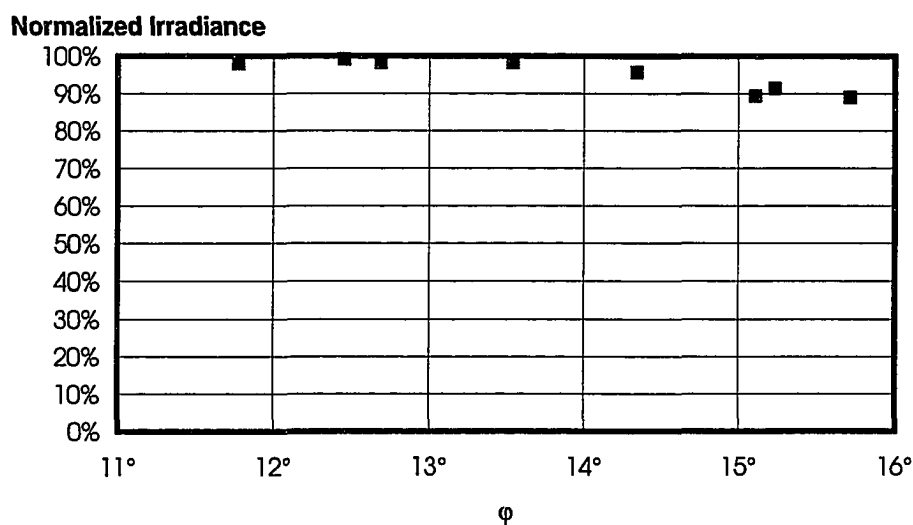


Figure 32, Irradiance Bias as a Function of ϕ

2. The second systematic error is a result of not factoring in the effects of dispersion. So far, when the data from the Bench Spectrograph was reduced, the amount of flux for any given wavelength was proportional to that directly recorded on the detector. However, since the diffraction angles, α and ϕ , change over the data set, the degree to which each wavelength is spread over the detector in the spectral direction is effected. To normalize out this effect, the raw flux should be divided by the

reciprocal linear dispersion. This was done for the unpolarized $y = 0$ data and is compared with that determined without this factor. A fit to each data set was made (see Section 7.3) and these are shown below:

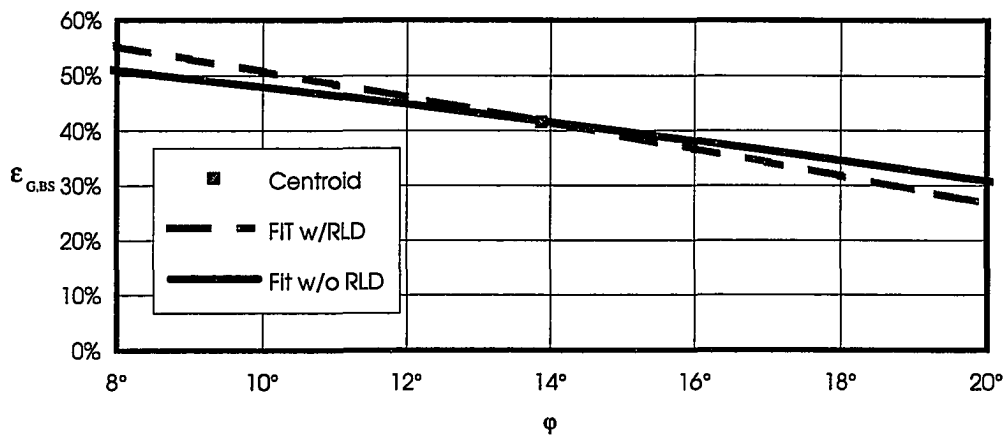


Figure 33, Effect of Dispersion on Efficiency

Here, w/RLD and w/o RLD signify whether normalization by the reciprocal linear dispersion was included or not, respectively. The result is that over the range of values of ϕ for which data were acquired, the original processed data without this allowance is approximately biased to be 10% more efficient at the high limit of ϕ relative to that at the low limit.

Fortunately, the two systematic errors offset each other to a large degree. Since the confidence level of this data is only on the order of $\pm 5\%$, no further refinement is warranted.

7.3 FITTING THE DATA

One of the reasons why the average grating efficiency function derived from the experimental data, $\epsilon_{G,BS}$, is validated, is the proximity of its shape to the theoretically derived models (the scalar method and that utilizing the Milton Roy data). The goal now, is to apply common sense to the data from all three methods so that they may be combined to yield the most reasonable estimate for the actual average grating efficiency dependence on the collimator-camera angle. This will then be used in the following section to model the all inclusive field dependent transmission term, $T(x,y)$. There are seven steps in the process:

1. The absolute efficiency returned by the average grating efficiency is rather unimportant since the computation of the potential information gathering power is relative. Nevertheless, it is necessary to normalize the three methods for estimating ϵ_G so they may be combined. The Milton Roy data is probably the better of the two theoretical models that yield absolute efficiency, so the other models will be scaled to match it. The Bench Spectrograph data yields relative efficiency only.
2. The scalar model is scaled to match the Milton Roy data. It was reduced to 77.5% of its original value.
3. The two theoretical models were then averaged together to produce the best theoretical estimate

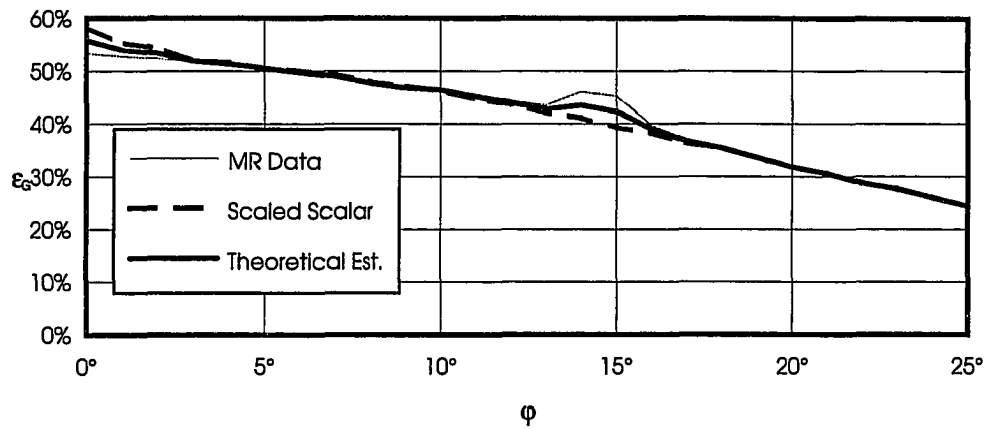


Figure 34, Theoretical Models of Average Grating Efficiency

Note the strong similarity between the two models. Since the range of the Milton Roy data extends only out to $\phi = 17^\circ$, for curve fitting (next step), the scaled scalar data will be appended to the tail of the best theoretical estimate for $17^\circ < \phi \leq 25^\circ$.

4. A numerical fit was made to the best theoretical estimate. It was determined that a three parameter fit would match the data. Four fits were investigated, parabolic, circular, cosine, and cosine². The two cosine fits have linear terms as well.

Type	Equation	Parameters	Residue
Parabolic	$\epsilon_G(\varphi) = C_1 + C_2 \cdot \varphi + C_3 \cdot \varphi^2$	$C_1 = .5452$ $C_2 = -.00564$ $C_3 = -.00026$	1.516
Circular	$\epsilon_G(\varphi) = \epsilon_o + \sqrt{r_o^2 - (\varphi - \varphi_o)^2}$	$\varphi_o = -10.14$ $\epsilon_o = -1850.28$ $r_o = 1850.85$	1.519
Cosine	$\epsilon_G(\varphi) = A_1 \cos(P_1 \varphi) + L_1 \varphi$	$A_1 = .5446$ $P_1 = .03257$ $L_1 = -.00533$	1.542
Cosine ²	$\epsilon_G(\varphi) = A_2 \cos^2(P_2 \varphi) + L_2 \varphi$	$A_2 = .5442$ $P_2 = .02428$ $L_2 = -.00500$	1.596

Table 10, Various Numerical Fits For Average Grating Efficiency

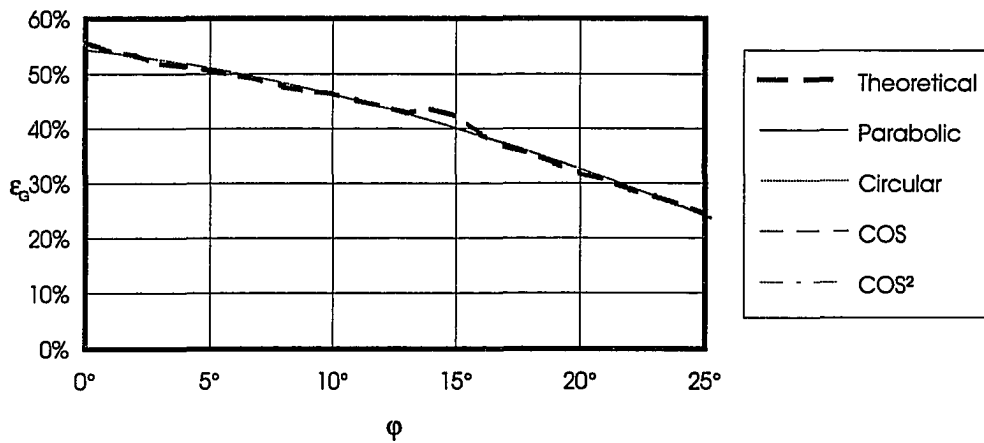


Figure 35, Various Numerical Fits Displayed

Visually there is little difference among the four numerical fits. The column labeled Residue in the Table 10 is proportional to the sum of the squares of the deviations from the respective fits. A lower number implies a better fit.

The circular fit was chosen for its simplicity, the fact that it is as good as the parabolic fit, and since it can be easily recast to minimize deviations radially as opposed to along the ordinate (efficiency axis) only. This latter characteristic allows the fitting of data to be unbiased with respect to slope, not weighting the region of higher φ disproportionately. This is important when there is a large spread to the data, such as with fitting to the Bench Spectrograph data.

5. Next the Bench Spectrograph data was scaled so that the centroid of the unpolarized $y = 0$ data set lies on the best theoretical fit. The average of all the camera-collimator angles within the data set (see Table 9) is $\varphi = 13.48^\circ$, which has an efficiency of 41.65% for the circular fit. The normalized flux from the data set was multiplied by 2.884×10^{-6} to convert to efficiency.
6. Then a circular fit to the Bench Spectrograph (experimental) data was determined so that the sum of squares of the radial deviations between the members of the data set and the fit was minimized.
7. And, finally the three parameters for the theoretical and experimental fits were averaged together:

Parameter	Theoretical	Experimental	Average
φ_C	-10.14	-27.89	-19.01
ε_C	-1850.28	-2505.97	-2178.12
r_C	1850.85	2506.74	2178.80

Table 11, Determination of Best Estimate of Grating Efficiency

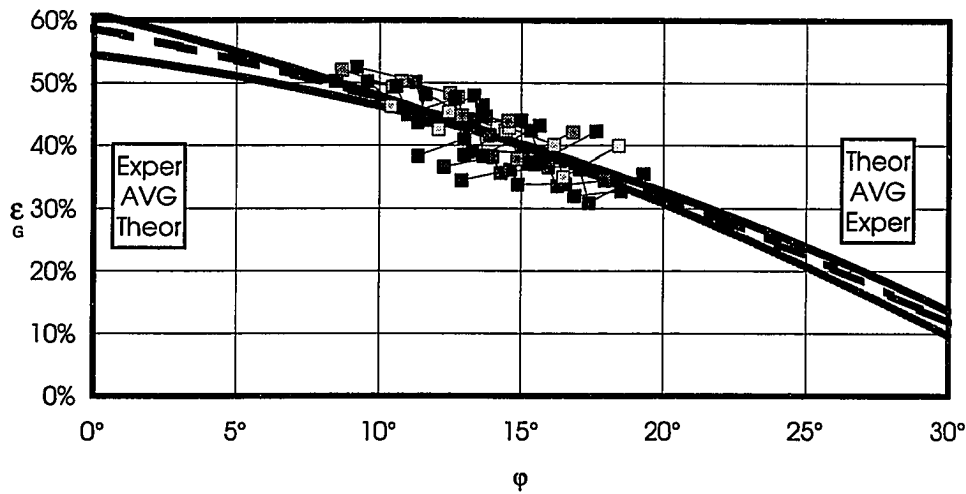


Figure 36, Best Estimate of Average Grating Efficiency

The experimentally determined efficiency function shows a marginally stronger dependence upon φ than the theoretical model. However, in the region of interpolation ($8^\circ \lesssim \varphi \lesssim 20^\circ$), the match between both methods is very good, deviating by only a few percent. For comparison, the experimental efficiencies for the unpolarized $y = 0$ case is plotted on top. The final best estimated average grating efficiency is then:

$$\varepsilon_G(\varphi) \cong -2178.12 + \sqrt{(2178.80)^2 + (\varphi + 19.01^\circ)} \quad [55]$$

8. MODELING

8.1 DETERMINATION OF THE SET-UP

It would be impossible to model all imaginable high resolution configurations. The method adopted is to start with an “average” set-up, evaluate and optimize, and then check to see how proposed modifications effect the larger range of possibilities.

A range of three camera-collimator angles was selected for analyses, $\varphi_c = 11^\circ$, 15° , and 19° . The angle $\varphi_c = 11^\circ$ was chosen as the low limit due to physical limitations of the spectrograph. The upper limit, $\varphi_c = 19^\circ$, was selected because it allows the camera objective to be placed approximately half as close to the grating as with $\varphi_c = 11^\circ$ (see Figure 11). Increasing φ_c past this results in a marginal reduction in the vignetting. In addition, with $\varphi_c = 11^\circ$, 15° , and 19° , it is expected that the sampling of φ_c is small enough to catch an anomalous behavior of the potential information gathering power within the range.

The next step is to select an “average” order in the “middle” of the usable wavelength range. The quotations around these terms reflect that the “middle” wavelength should be selected bluer than the numerical mean of the edges of the usable range. There are two reasons for this. With many notable exceptions, scientific interests tend to favor the blue. But, more importantly, dispersion is more predominate in the blue. In other words, the mean optical path though a refractive system in terms of wavelength is toward the blue. So, there is as much, if not more, change in the imaging properties from $.35 \mu\text{m}$ to $.55 \mu\text{m}$ as there is from $.55 \mu\text{m}$ to $1.0 \mu\text{m}$.

The order $m = 10$ was selected for this reason and because of the correlation to the orders used in the analyses of grating efficiency ($m = 12$ for the scalar theory, $10 \leq m \leq 13$ for the Milton Roy data, and $m = 10$ for the Bench Spectrograph data). The on-blaze center of this order changes as a function of φ_c going from $\lambda_{BL} = 5633 \mu\text{m}$ @ $\varphi = 11^\circ$ to $\lambda_{BL} = 5582 \mu\text{m}$ @ $\varphi = 19^\circ$. The blaze wavelength, though is not the “middle” wavelength of the order. The middle wavelength is found, rather, by first determining what the “middle” grating angle is as a function of φ_c .

For each φ_c , m and α were determined for each wavelength (sampled linearly) over the range $.35 \mu\text{m} \leq \lambda \leq 1.0 \mu\text{m}$. This was done by simply finding the combination closest to the blaze condition (minimizing $|m_{OFF} - m|$). In Figures 7-9, this is the region between the squares for each order. Then, the average grating angle, α_{AVG} , was computed. The following table summarizes the results:

		$\varphi_c = 11^\circ$	$\varphi_c = 15^\circ$	$\varphi_c = 19^\circ$	
x	$\Delta\varphi$	69.355°	71.426°	73.498°	← α_{AVG}
-24.58 mm	4.929°	.5503 μ	.5476 μ	.5443 μ	
-18.43 mm	3.700°	.5543 μ	.5518 μ	.5486 μ	
-12.29 mm	2.469°	.5581 μ	.5559 μ	.5529 μ	
-6.14 mm	1.235°	.5619 μ	.5598 μ	.5570 μ	
0 mm	0°	.5655 μ	.5636 μ	.5610 μ	
6.14 mm	-1.235°	.5691 μ	.5673 μ	.5649 μ	
12.29 mm	-2.469°	.5724 μ	.5709 μ	.5687 μ	
18.43 mm	-3.700°	.5757 μ	.5744 μ	.5724 μ	
24.58 mm	-4.929°	.5788 μ	.5777 μ	.5759 μ	

Table 12, Configuration Summary with Wavelengths

Here, in addition to summarizing the average grating angles, nine wavelengths are shown which are uniformly distributed across the detector in the x direction for each camera-collimator angle. These three configurations will be used to

determine the optimal selection of ϕ_c . A number of other modifications will be considered. Each of these modifications and combinations of these modifications will be modeled and evaluated with each of the three camera-collimator angles.

Normally the distance between the fibers and the collimator is fixed and equal to the collimator focal length. Actually, there is a slight adjustment to account for the reduced thickness of the interference filter. The first configuration modification is allowing this distance (from the rear of the interference filter to the vertex of the collimator) to change from the first order value. This permits some balancing of the field aberrations and can be thought of as moving the object plane to a compromise position of the best object surface, similar to moving an image plane.

The second modification option is inserting a refractive field lens behind the interference filter. The primary advantage is the ability to shift the spatial pupil forward from the location of the fibers in the return beam to a position of choice. The following simplified figure shows the unfolded geometry of the spectrograph without a field lens:

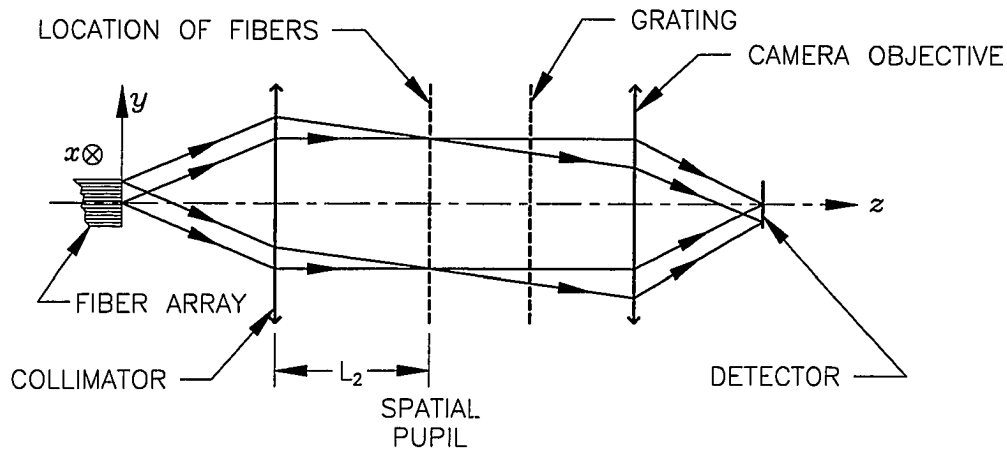


Figure 37, Unfolded Spatial Geometry, No Field Lens

L_2 is the first order distance from the collimator along the unfolded path to the location of the spatial pupil. The following table summarizes the vignetting for the original unmodified spectrograph. The vignetting can occur in four places. The row marked Camera actually is a summation of many different places that vignetting can occur within the camera. Vignetting is the average for the nine wavelengths spaced across the detector and for nine field positions spaced evenly from $y = 0$ to 38.1 mm (\bar{y}_{FIB}). Vignetting includes effects from ray missed surface errors and total internal reflections. The amount of vignetting was computed by tracing a uniformly distributed grid of 68^2 rays in the pupil through the model of the spectrograph (see Table 13). The rays from the four corners of the square grid that did not pass the pupil were, of course, not counted.

Location	% Vignetted
Collimator	0.0%
Foot Shadow	8.3%
Grating	6.7%
Camera	35.7%
Total	50.8%

Table 13, Vignetting Summary for Original Configuration ($\phi_c = 11^\circ$)

There are a couple of noteworthy items regarding the vignetting from the original spectrograph. There is negligible vignetting at the collimator, a small amount at the grating, and the bulk occurring in the camera. It is expected that by shifting the location of the spatial pupil in the direction of the camera, there would be less vignetting. This is, in fact, the case and is accomplished by assigning negative power to the field lens. This allows the chief rays of the fibers to diverge from the lens and then after the collimator converge at a less rapid rate.

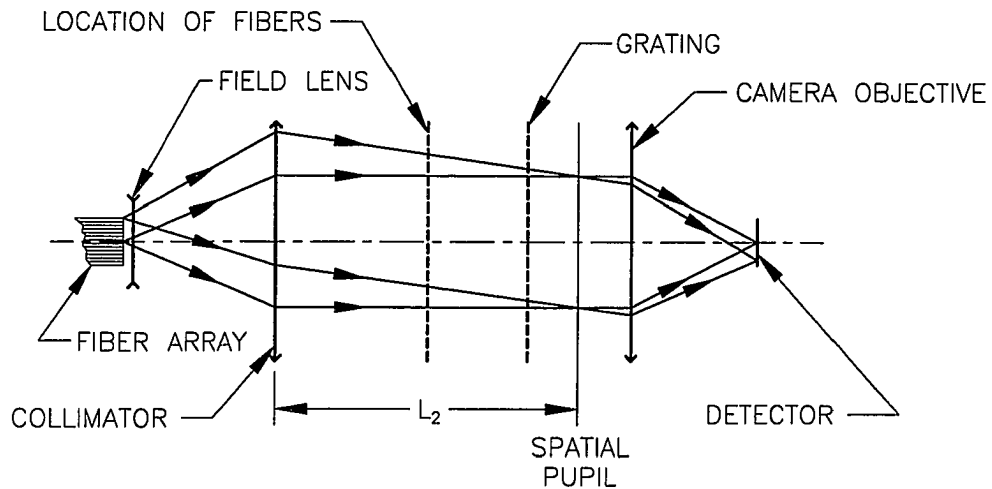


Figure 38, Unfolded Spatial Geometry, With Field Lens

On a case by case basis, the first step for a configuration having a field lens is to find the location of the spatial pupil, L_2 , with the least amount of vignetting. However, rather than utilizing L_2 as the independent variable, a choice is made to use \bar{u} , the paraxial chief ray angle evaluated after refracting out the back side of the field lens. The reason is that it can be easily related to the radius of curvature of the back side of the field lens, R_2 , when front side is plano ($R_1 = \infty$) and R_2 is amenable to optimization with the optical design program.

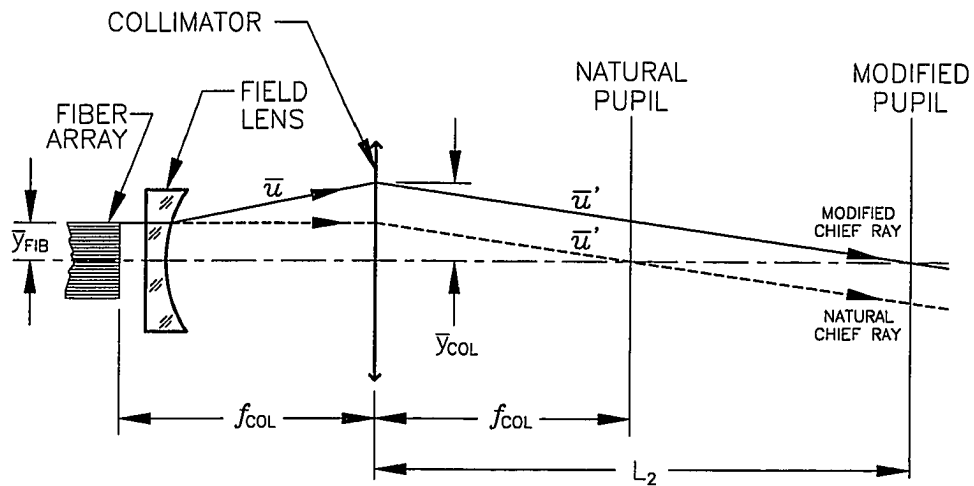


Figure 39, Modified Spatial Pupil and Chief Rays

$$\bar{u} = \frac{\bar{y}_{\text{FIB}}(n_{\text{FL}} - 1)}{R_2} \quad [56]$$

Where, the subscript FL designates a property of the field lens. This angle, \bar{u} , can also be related to the position of the spatial pupil, L_2 , by assuming the field lens to be located at the fibers. In fact, this is the working definition of a true field lens, a lens placed at or near the location of an image²⁴. In this case the *image* is the object itself. When the effects of reduced thicknesses of the interference filter and the field lens are accounted for, the back side of the field lens is located approximately 2% of the distance to the collimator away from the fibers. So although it is not strictly speaking a field lens, it will be referred to as such. Paraxially then, the chief ray angle after reflecting from the collimator will be the same whether or not a field lens is employed:

$$L_2 \cong \frac{\bar{y}_{COL} \cdot f_{COL}}{\bar{y}_{FIB}} \quad [57]$$

$$\cong f_{COL} \left[1 + \frac{f_{COL} (n_{FL} - 1)}{R_2} \right] \quad [58]$$

The following figure shows vignetting of the original spectrograph with the spatial pupil re-imaged by virtue of the field lens. There are three principal locations on the plot that are indicated by vertical dashed bars, the natural location of the spatial pupil (at the fibers in the return beam from the collimator), the grating, and the front vertex of the Bench Spectrograph Camera, designated BSC.

% Unvignetted

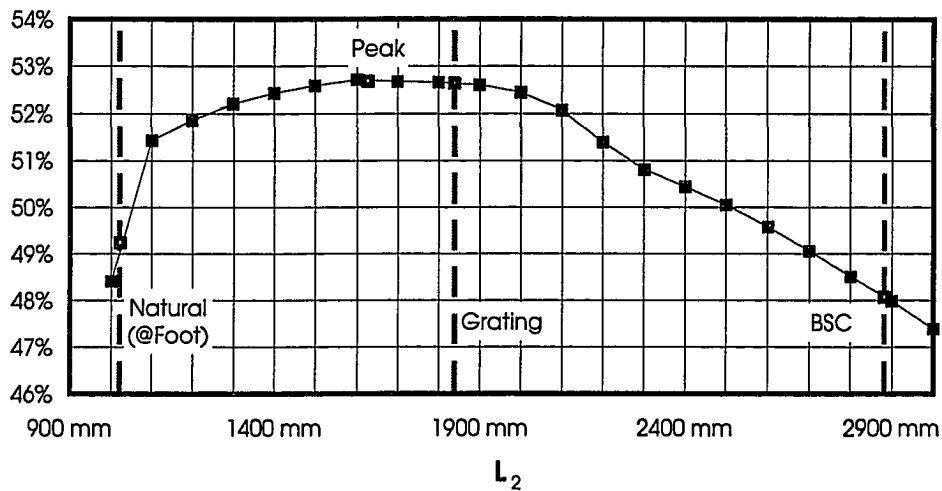


Figure 40, Spatial Pupil Dependence on Vignetting

As the spatial pupil is moved forward, granted the vignetting in the camera, which predominates in the unmodified system, decreases. However, the vignetting at collimator and grating increases. For this case, the peak transmission (highest unvignetting) occurs at a point approximately 200 mm in front of the grating and it

corresponds to the field lens having a concave back surface of $R_2 = 892$ mm with a chief ray angle of $\bar{u} = .0221$. Now, once this angle is fixed, the parameters of the field lens (see Section 6.2.1) are allowed to vary in an effort to optimize the imaging properties of the system since the vignetting will remain nearly fixed.

When a negative power field lens is inserted, the off-axis beams will diverge on their way to the collimator. This will produce vignetting there. In the preceding figure, this becomes the predominate effect for large values of L_2 . The third modification considered is replacing the collimator with another of the same focal length but with a larger blank size. It is increased from having a clear aperture (diameter) of 242 mm to one having an aperture of 292 mm.

The final modification option is reducing the focal length of the collimator from 1021 mm to 914 mm to produce a smaller diameter beam per fiber consistent with the size produced previously at the 4m telescope. This is to compensate for the enlarged fiber radiance pattern at the WIYN telescope. A smaller beam will undergo less vignetting. The downside is that with a shorter collimator focal length, the field angle (θ) will increase and there will be more aberration introduced at the collimator. This trade-off will be quantified and analyzed.

In addition to each of these modification options, there are several permutations that are investigated. For instance, in addition to adding a field lens to the otherwise unmodified spectrograph, it may be added to one having a collimator with a larger aperture or one with both a larger aperture and a reduced focal length. Finally, all of these permutations will be evaluated at each of the three camera-collimator angles.

8.2 ANALYSIS

This section describes the model of the spectrograph and the model of determining \mathcal{P}_{REL} , the relative potential information gathering power. The goal is to evaluate \mathcal{P} relative to that for the unmodified spectrograph for each of the possible modifications listed above.

8.2.1 Effects Which are Not Modeled

Before proceeding with the development of the evaluation of \mathcal{P} , it is prudent to note the items which are not modeled. This list is relatively short. At the top of this list is the uncertainty of the actual fiber radiance pattern, as previously discussed in section 7.2.5. A uniform distribution is assumed. It is expected that when the system comes on-line in 1995, a measurement of the distribution will be made. In addition to this, the following items are also not included:

1. The refractive properties of the optical cement: There are three cemented doublets within the all-refractive Bench Spectrograph Camera. It is assumed that each of the two elements are in contact having inner radii equivalent to the average of the two measured values.
2. Astigmatism of the rear element of the Bench Spectrograph Camera: It is a nominally concave-plano field flattener. However, the rear plano surface is astigmatic and slightly concave. The radius varies from .52 km to .73 km, which translates to a surface error of approximately $.7\lambda @ .6328 \mu\text{m}$.

The effect of the astigmatism is not noticeable and an average rear radius of .62 km is assumed.

3. The individual refractive properties of the interference filters: There is a set of order separating interference filters, each with peculiar composition and refractive properties. Each filter is planar. The properties of several filters were averaged together yielding a composite thickness of 6.4 mm, an index of 1.53 (n_d), and an Abbe number of 65. The variance within the set is relatively small and the proximity of the filter (9.8 mm) to the fibers renders inconsequential all but the effects of the reduced thickness.
4. Non-ideal opto-mechanical and thermo-mechanical effects: The alignment of the various modules making up the instrument was done meticulously so that the effects of misalignment are negligible. Furthermore, the assembly of the Bench Spectrograph Camera (though not completed) is done utilizing a process known as the lathe assembly technique²⁵, again to virtually eliminate effects from misalignments.
5. N₂ filling of two cavities: The interspatial media between the rear of the camera objective (this is the same element as mentioned in #2, above) and the front of the dewar window is filled with N₂ to prevent water condensation on the dewar window. There is another cavity within the objective which must be filled as well due to mechanical constraints. Air is

mostly N_2 and their refractive properties are virtually identical, especially at the reduced pressure owing to operation at Kitt Peak National Observatory (see Section 8.2.3).

6. Both optical cables: Rather than doing the analysis for either or both the blue cable (310 μm core diameters) and the red cable (200 μm core diameters), it will be assumed that the fibers have median core diameters of 250 μm .

8.2.2 Assembling the Relative Information Gathering Power

The goal is to come up with a fair estimate of \mathcal{P}_{REL} for each configuration. The procedure for this is to simplify Equation 14 and assemble the constituent parts. First, since the subject of the thesis is an improvement in the spectrograph from an unmodified configuration, all scalar constants which go into making up \mathcal{P}_{REL} can be eliminated from consideration since the resultant \mathcal{P}_{REL} for each configuration will be normalized (divided) by that determined for the unmodified case.

The first quantity to suffer this fate is the relative flux coupled into each fiber, ϕ , since this will not change as a function of fiber number, n . It is assumed that the imagery produced at the telescope focal surface is approximately equivalent over the telescope field. The next simplification is to perform the original sum over n , instead over a diminished, though representative, sample. The last simplification is to do the same for the integral over x , changing this to a representative sum. With finer sampling of x and y on the detector, the estimate is better. As long as the sampling is fine enough to pick up the finest trends in the constituent parts which change as function of configuration, the estimate for \mathcal{P}_{REL} will be valid.

$$\mathcal{P} \propto \sum_y \sum_x \frac{T(x, y)}{w(x, y) \cdot \bar{n}(x, y)} \quad [59]$$

A spreadsheet was used for each configuration to assemble $T(x, y)$, $\bar{n}(x, y)$, and $w(x, y)$ into \mathcal{P}_{REL} . The degree of sampling over x and y was determined by analyzing the output from the ray trace model for the highest frequency term that goes into \mathcal{P}_{REL} .

8.2.3 The Ray Trace Model

The ray trace model produces two parameters that are incorporated by the spreadsheet in the calculation of \mathcal{P}_{REL} . The first is the RMS full-width spot size in the x (or spectral direction) which is a function of field and wavelength, $w_{\text{PSF}}(y, \lambda)$. The subscript PSF designates that this non-diffraction width is associated with a theoretical point source located on a line $x = 0$ at the fiber array (the object). w_{PSF} is a property of the spectrograph and its configuration. It does not include geometrical imaging effects, diffraction, nor detector effects. Since the size of the pupil and the radiance distribution are functions of properties of the fibers and not the spectrograph, w_{PSF} will be dependent only on these external aspects to the instrument proper. The other contribution of the ray trace model is the amount of vignetting (actually, percent unvignetted) as function of field and wavelength, $\varepsilon_v(y, \lambda)$.

A listing of the software model for the spectrograph is found in Appendix C. Included in the ray trace model are the following:

1. The fibers are stacked in a parallel array along the y axis. This telecentricity is modeled by placing the entrance pupil 1 km in

front of the array and adjusting the numerical aperture to the equivalent of an $f/6.0$ distribution ($N.A. = .08305$). After the rays are traced to this pupil, they are re-traced 1 km back along the z axis to the fiber array from which they start propagating through the model of the spectrograph.

2. There are two places where refractive elements are used. The first is directly in front of the fibers where there is an interference filter and, in some cases, a field lens. The interference filter is modeled as an index data element having a median index of n_d and with dispersive properties given by the Abbe number, v . The partial dispersion is assumed to lie along the normal line defined by the Schott glass types F2 and K7. The field lens is not constructed. It is assumed to be made out of the Schott glass type BK7 (though, see Section 9.2) and has the nominal catalog index properties of that type. The second area of refractive elements within the spectrograph is the camera. In the objective there are 5 refractive components, two singlets and three doublets. There are three steps to the melt fitting for these glasses:

- A. Some indices and dispersions (defined as the differences between two indices) were measured by the manufacturer. The quantity and location of these measurements changed both with manufacturer and within manufacturer. For elements **C** and **D**, a least squares fit of these

measurements were made to minimize the errors for the over constrained indices and dispersions.

- B. From this data, 2 points (λ , n) were picked to anchor the matching relative partial dispersion fit, which will exactly go through these two points.
- C. A fit matching the relative partial dispersion (MRPD) to the nominal glass was made. The nominal Sellmeier coefficients provided by the Schott catalog were used for this.

$$n_{\lambda, \text{MRPD}} = n_{2, \text{A}} - \frac{(n_{2, \text{N}} - n_{\lambda, \text{N}}) - (n_{1, \text{A}} - n_{2, \text{A}})}{n_{1, \text{N}} - n_{2, \text{N}}} \quad [60]$$

The prefix of the subscript designates if the index is determined as a function of wavelength (λ), or at one of the two anchoring wavelengths (1 and 2). The suffix of the subscript designates if the index is from one of the two anchors (A) or the nominal value (N).

- D. A fit was then made to the MRPD data for 10 wavelengths covering the range $.35 \mu\text{m} \leq \lambda \leq 1.19 \mu\text{m}$. New Sellmeier coefficients were found that minimized the sum of the squares to the MRPD data.

$$n_{\lambda, \text{FIT}} = \sqrt{1 + \frac{K_1 \lambda^2}{\lambda^2 - 1_1} + \frac{K_2 \lambda^2}{\lambda^2 - 1_2} + \frac{K_3 \lambda^2}{\lambda^2 - 1_3}} \quad [61]$$

The following table summarizes the results of the melt fitting:

	Element Designator			
	A	B	C	D
MFGR	Schott	Schott	Schott	Schott
Type	BK7	BK7	F7	SSK4A
n_d	1.516778	1.516778	1.625419	1.617751
v	64.188	64.188	35.607	55.155
K_1	1.03800582E+0	1.03800582E+0	1.35846704E+0	1.38383146E+0
K_2	2.33344877E-1	2.33344877E-1	2.10897611E-1	1.86982661E-1
K_3	1.01009280E+0	1.01009280E+0	8.80726049E-1	9.44083383E-1
l_1	5.98546613E-3	5.98546613E-3	1.01367763E-2	7.87000334E-3
l_2	1.99749194E-2	1.99749194E-2	4.82820554E-2	2.89425612E-2
l_3	1.03560659E+2	1.03560659E+2	1.10387295E+2	1.05742424E+2
Confidence	$\pm 3E-6$	$\pm 3E-6$	$\pm 3E-6$	$\pm 2E-6$
	Element Designator			
	E	F	G	H
MFGR	Schott	Corning	Ohara	Schott
Type	BaLF4	C17-55 (SSK4A)	LF7	BaSF52
n_d	1.579295	1.617750	1.575290	1.701820
v	53.718	55.206	41.567	41.119
K_1	1.29307667E+0	1.38168353E+0	1.26982046E+0	1.63894711E+0
K_2	1.57991089E-1	1.89180369E-1	1.56701572E-1	1.84586225E-1
K_3	9.46734806E-1	9.43261899E-1	8.84833681E-1	1.00473971E+0
l_1	7.80121527E-3	7.83884978E-3	9.14548446E-3	9.89356286E-3
l_2	3.21368399E-2	2.88359523E-2	4.46915081E-2	4.62602211E-2
l_3	1.09158666E+2	1.05742525E+2	1.06820366E+2	8.16164147E+1
Confidence	$\pm 2E-6$	$\pm 7E-6$	$\pm 2E-5$	$\pm 3E-6$

Table 14, Melt Fitting Summary

The confidence factor reflects the maximum absolute deviation of the data from the fit. It is not a standard deviation.

The final refractive element in the camera is the dewar window, which is made out of fused silica. Normally, the melt-to-melt variation of fused silica is small enough ($\leq 10^{-6}$) to be ignored²⁶.

3. The refractive properties are all given relative to air. Since the spectrograph is to operate at Kitt Peak National Observatory, the indices were modified slightly to account for the change in environment from standard pressure and temperature (STP), which is defined as $T = 20^\circ \text{ C}$ and $P = 1.00$ atmospheres (760 mm Hg). The average operational conditions are $T \cong 15^\circ \text{ C}$ and $P \cong .765$ (580 mm Hg corresponding to a height of approximately 2.1 km). There are, of course, seasonal changes in these values which reflect average conditions.
4. The fictitious dispersion of the vacuum in the dewar was modeled. This was done in five steps:

- A. For 10 vacuum wavelengths covering the range of .35 μm to 1.19 μm , the index of dry air was computed for $T = 15^\circ$ and $P = 1.00$ using the formulation from Edlén²⁷:

$$n_{T=15, P=1} = 1 + \left(6432.8 + \frac{2949810 \lambda_{\text{VAC}}^2}{146 \lambda_{\text{VAC}}^2 - 1} + \frac{25540 \lambda_{\text{VAC}}^2}{41 \lambda_{\text{VAC}}^2 - 1} \right) \times 10^{-8} \quad [62]$$

- B. The air indices were converted to values at STP by applying the formulation given by Kohlrausch²⁸:

$$n_{\text{STP}} = 1 + \frac{n_{T=15, P=1} - 1}{1 + .0034785 \cdot (20 - 15)} \cdot 1 \quad [63]$$

- C. The reciprocal was taken to yield the fictitious indices of air at STP as a function of vacuum wavelengths.

- D. The vacuum wavelengths were converted to air wavelengths by dividing by the STP air indices.
- E. Sellmeier coefficients were found by minimizing the sum of the squares of the errors.

K_1	-9.98340700E-5
K_2	-3.11447250E-3
K_3	2.67863389E-3
l_1	-5.31510156E-3
l_2	1.03934642E-2
l_3	1.07652513E-2

Table 15, Fictitious Sellmeier Coefficients for Vacuum

The advantage to creating a fictitious dispersion for the vacuum is that the “canned” software routine can then be used to determine the glass indices at any temperature and pressure (relative) to air. At the same time, the fictitious vacuum index relative to air is not a function of these parameters and remains correct. A check of this method was made by reducing the pressure to zero and seeing how close to unity the vacuum index became. The absolute error is on the order of 4×10^{-6} and within 1×10^{-8} of being invariant across a typical wavelength range imaged onto the detector.

5. As built parameters were used in modeling the optical system. For example, with the Bench Spectrograph Camera, each radius and thickness, whether external or internal, was measured by a minimum of two separate methods and/or facilities.

6. All vignetting effects, regardless of how small their impact, were modeled.

For computing the RMS full-width in the x direction, w_{PSF} , and percent of unvignetting, ϵ_v , for each combination of field and wavelength, a macro was written. There are two noteworthy items in this macro. First, w_{PSF} is computed with respect to the centroid of image. So, the rays are traced twice, the first time to determine the centroid location and the second time to do the actual computation. Secondly, the rays are traced from a square grid in the pupil, where the grid density can be changed. In order to determine the appropriate density, first a goal of achieving 1% accuracy (actually precision) was established. Then a version of the macro was run for a typical model of the spectrograph with the density progressively increased. At a density of 68^2 , both w_{PSF} and ϵ_v change on the order of less than 1% so this density was adopted for the modeling.

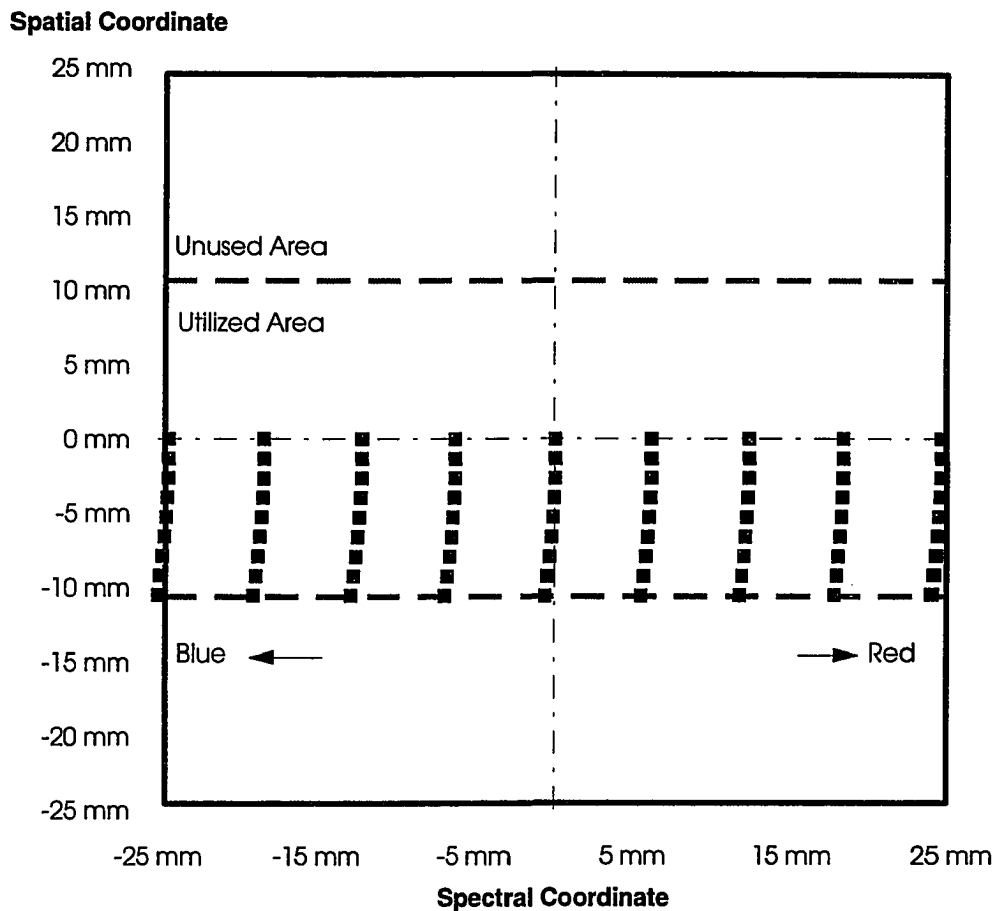


Figure 41, Image Centroids for 9 y by 9 λ Sampling

The sampling for evaluation is chosen to be 9 field locations by 9 wavelengths. Here, the centroid values were computed for the unmodified spectrograph operating at $\varphi_c = 11^\circ$. The square border shows the size of the 2048^2 CCD which measures 24.58 mm on a side. The wavelengths are chosen so that the first and last are computed to be at the spectral edges of the detector for $y = 0$ using a first order calculation of $\Delta\varphi$ (Equation 40). This does not include the effects of distortion and shift of image placement from the chief rays (for each y , λ) to the

centroid. The latter is a result of asymmetrical aberration such as coma and complex vignetting. It is evident that for $y = 0$, these edge wavelengths are imaged just inside the extent of the detector. The central (5th) wavelength in the series is the chief wavelength which is imaged on the center of the CCD. Furthermore, as is evident, the effect of conical distortion gives each spectral line a curved shape.

The horizontal dashed lines show the extent of the utilized area of the CCD and are located at $y = \pm m_y \cdot \bar{y}_{\text{FIB}}$ (± 10.64 mm). The sampled field positions are chosen to be on **one** side of the field axis. At the fiber array (the object), the 9 field positions are chosen above the field axis, $y \geq 0$. The spectrograph images the array magnified and mirrored about the field axis (Figures 38-39), so these positive object fields will image below the field axis, $y \leq 0$. Since, the spectrograph is slightly asymmetric with respect to field (see Section 6.1.1), the imagery and vignetting will vary slightly for mirrored points ($+y, \lambda$ to $-y, \lambda$). A comparison of the effects of this asymmetry is shown in the following two tables, where the unmodified spectrograph operating at $\varphi_c = 11^\circ$ was modeled for values of $+y$ and $-y$ and the differences in w_{PSF} and ϵ_v computed (positive object field less negative object field).

Object Field	Wavelength								
	.5503 μ	.5542 μ	.5581 μ	.5619 μ	.5655 μ	.5691 μ	.5725 μ	.5757 μ	.5788 μ
0 mm	.0 μ								
± 4.8 mm	-.7 μ	-.6 μ	-.2 μ	.0 μ	.0 μ	.0 μ	-.1 μ	-.3 μ	-.5 μ
± 9.5 mm	-1.7 μ	-1.1 μ	-.2 μ	.0 μ	.0 μ	.0 μ	.0 μ	-.5 μ	-1.2 μ
± 14.3 mm	-2.8 μ	-1.3 μ	.0 μ	.1 μ	.1 μ	.1 μ	.2 μ	-.6 μ	-2.3 μ
± 19.1 mm	-4.1 μ	-1.5 μ	.3 μ	.3 μ	.2 μ	.3 μ	.4 μ	-.8 μ	-3.3 μ
± 23.8 mm	-5.4 μ	-1.6 μ	.5 μ	.6 μ	.4 μ	.6 μ	.6 μ	-1.0 μ	-4.2 μ
± 28.6 mm	-6.3 μ	-1.7 μ	.6 μ	.7 μ	.6 μ	.7 μ	.7 μ	-1.2 μ	-4.5 μ
± 33.3 mm	-6.7 μ	-1.9 μ	.7 μ	.8 μ	.6 μ	.8 μ	.7 μ	-1.5 μ	-4.8 μ
± 38.1 mm	-7.0 μ	-2.0 μ	.8 μ	.9 μ	.7 μ	.9 μ	.7 μ	-1.9 μ	-4.1 μ

Table 16, \pm Field Comparison, w_{PSF}

Object Field	Wavelength								
	.5503 μ	.5542 μ	.5581 μ	.5619 μ	.5655 μ	.5691 μ	.5725 μ	.5757 μ	.5788 μ
0 mm	0%	0%	0%	0%	0%	0%	0%	0%	0%
± 4.8 mm	0%	-1%	0%	0%	0%	0%	0%	-1%	-1%
± 9.5 mm	-1%	-1%	0%	0%	0%	0%	0%	-2%	-1%
± 14.3 mm	-1%	-2%	-1%	0%	0%	-1%	-1%	-2%	-2%
± 19.1 mm	-2%	-2%	-1%	-1%	-1%	-1%	-2%	-2%	-1%
± 23.8 mm	-2%	-2%	-2%	-2%	-1%	-1%	-2%	-2%	-2%
± 28.6 mm	-3%	-2%	-2%	-2%	-2%	-2%	-2%	-2%	-1%
± 33.3 mm	-2%	-2%	-2%	-2%	-2%	-2%	-2%	-2%	-1%
± 38.1 mm	-2%	-2%	-2%	-2%	-2%	-2%	-2%	-2%	-2%

Table 17, \pm Field Comparison, ϵ_v

The first observation is that there is slightly more vignetting for the positive (object) field. The complex vignetting has an odd impact on the imagery, which is mixed. However, for both w_{PSF} and ϵ_v , the effects are negligible. For example, even a difference of 7 μm in w_{PSF} translates to less than a 1% effect in all-inclusive w . Furthermore, it is a safe assumption to expect that if the imagery and vignetting improve for one half of the field, they will likewise improve for the other half as well. The inverse is also true. Typical shapes for $w_{\text{PSF}}(y, \lambda)$ and $\epsilon_v(y, \lambda)$ are now given. They are for the case of the unmodified spectrograph operating at $\phi_c = 11^\circ$.

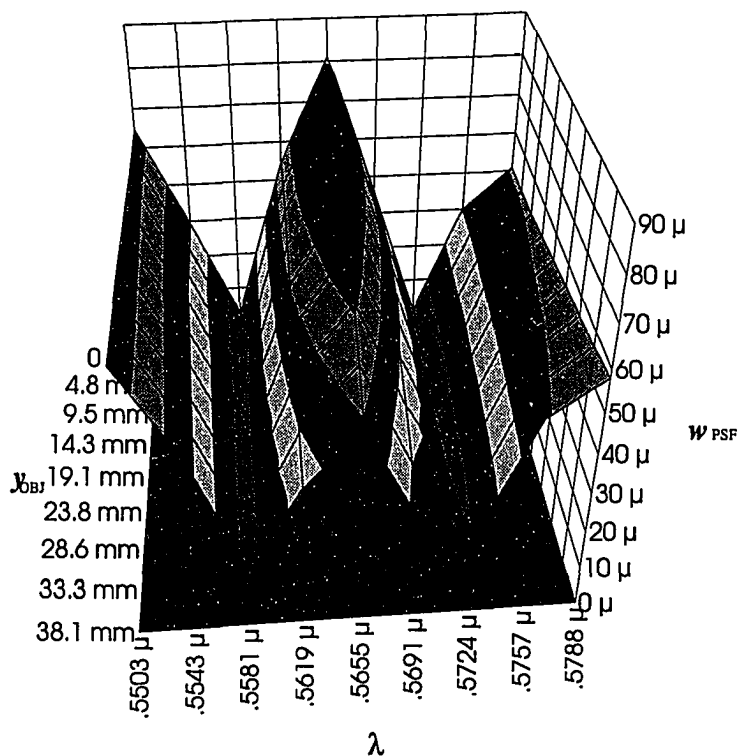


Figure 42, Typical $w_{\text{PSF}}(y, \lambda)$

The strong “W” shape is a result of the warp in the CCD. It allows roughly only an annulus of the detector to be within good focus. The imagery is optimized so that center and corners of the 2 dimensional field are almost equally compromised. The reason that the best imagery (lowest w_{PSF}) does not resemble a circle is due to the fact that less than half the detector is used in the y direction. The valleys of the “W” do in fact come together in the direction of increasing y , which is not shown.

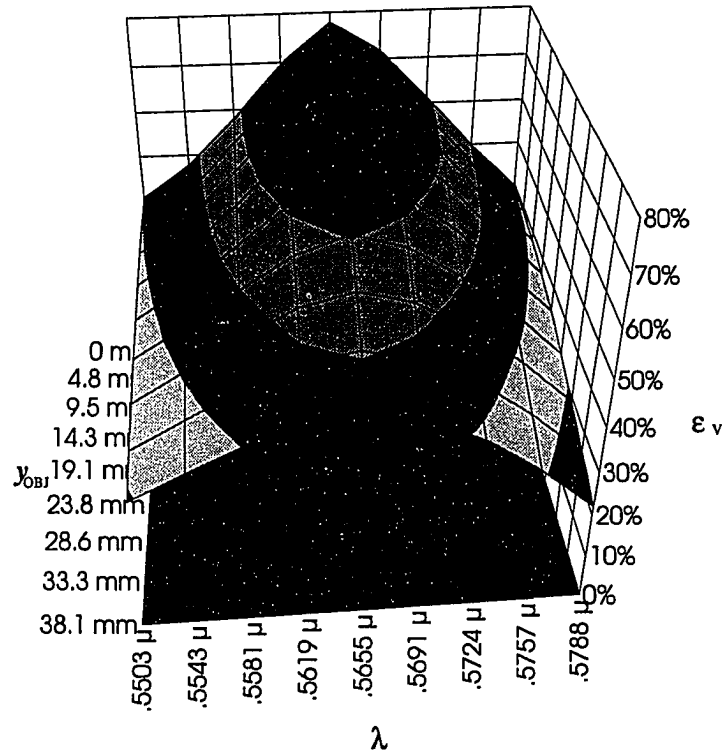


Figure 43, Typical $\epsilon_v(y, \lambda)$

The vignetting function (ϵ_v) is, as expected, smooth and monotonically decreasing from the center of the detector. This belies the fact that it has a fairly complex geometry. Of the two field dependent terms produced from the ray trace model, $w_{PSF}(y, \lambda)$ changes much more rapidly over the 2 dimensional field. It is with this parameter that the impetus for sampling at $9 y$ by 9λ is evident. Certainly, an argument could be made for reducing the sampling in the y direction and, in fact, this will be utilized in Section 8.3. In terms of the λ direction, the question is whether sampling at 9 wavelengths is good enough, for the peaks and valleys have

definite cusp like tendencies. Unfortunately, a finer sampling with λ was not investigated since this is the practical limit with the “canned” software.

Finally, a note regarding an assumption that has been made. Due to conical diffraction and distortion (and to a much lesser extent imagery), the region covered by the ray trace model is not exactly the same as the utilized area of the CCD. So, optimizing the spectrograph over the shape covered by the ray trace model is an approximation of optimizing the true information gathering power. However, the overlap of the areas are on the order of 98% and it is a safe assumption that optimizing over the model area applies to the actual \mathcal{P} goal region as well.

8.2.4 The Transmission Term

The first of three terms to be assembled into the relative information gathering power (Equation 59) is the field dependent transmission term $T(x,y)$. As already stated in Section 5.3.2, the transmission term is the product of three components (Equation 13):

1. ϵ_T represents the traditional transmissive losses of an optical system. It includes anti-reflection coatings, absorption in glass (or SiO_2), and reflections from mirrored surfaces. It will be assumed that this term is not field dependent. A rule of thumb is that when angles of incidences for air/glass and air/mirror surfaces are on the order of 7° or less, polarization effects are minimal. With one exception, all these effects are common to all configurations and can be neglected in the computation of \mathcal{P}_{REL} . The exception is the addition of a field lens, which

introduces 2 more air/glass surfaces over the unmodified system, $N_{\text{SUR}} = 2$. It is the intention to coat the field lens with a very broad band anti-reflection coating which, typically, will have a gradual change in transmission over the region .35 μm to 1.0 μm . A good estimate of the average transmission, $T_{\text{AIR} \leftrightarrow \text{GL}}$, for a single layer MgF_2 coating is 98% per surface. So, for the field lens case,

$$\epsilon_T = T_{\text{AIR} \leftrightarrow \text{GL}}^{N_{\text{SUR}}} \quad [64]$$

$$\cong .96 \quad [65]$$

It is expected that the additional absorption loss within the field lens is inconsequential.

2. ϵ_v is the fraction of unvignetted light passed through the spectrograph. It is strongly field dependent, both in the spatial and spectral senses $\epsilon_v(y, \lambda)$. This term is produced by the ray trace model (Section 8.2.3).
3. ϵ_G is the average grating efficiency that is derived in Chapter 7 (Equation 55). It is assumed to be a function ϕ but not y , $\epsilon_G(\phi)$ or $\epsilon_G(\lambda)$. The relationship between ϕ and λ is given by Equations 16 or 18.

8.2.5 The Image Width Term

The second of three terms to be assembled into the relative information gathering power (Equation 55) is the field dependent RMS full-width in the spectral

direction $w(x,y)$. The technique employed here in the determination of this term is not rigorous. Nevertheless, it is found to be rather accurate. The assumption is that the composite RMS full-width is equal to the components added up in quadrature:

$$w = \sqrt{w_{\text{PSF}}^2 + w_{\text{IMG}}^2 + w_{\text{PIX}}^2 + w_{\text{DIFF}}^2} \quad [66]$$

This equation is exact for the case when the distributions for the four components in the focal surface are Gaussians. And, this really is not the case for any of them. However, a test of the validity of this assumption reveals a remarkably good result. The components are now described in the order presented in the equation.

As shown in the Section 8.2.3, the RMS full-width from a theoretical point source, w_{PSF} , varies strongly both as a function of y and λ (Figure 43). This term is produced by the ray trace model (Section 8.2.3).

The second term, w_{IMG} , represents the RMS full-width of an ideal image of a fiber. In an ideal case, the image of each fiber would be an ellipse with major and minor axes given by the product of the fiber diameter and the spatial and spectral magnifications respectively. Now the way that spectra are extracted, is to sum the captured flux along the spatial dimension for each wavelength unit*. Consider the source aperture (or fiber) as a series of differential slices along x , centered on $x = 0$, and having different values for y . At the image surface, the width of any given slice will be equal to the product of the source width and the spectral

* A modification of the direct summation method is to weight the flux inversely proportional to the variance along y (K. Horne, "An Optimal Extraction Algorithm for CCD Spectroscopy", *PASP*, v. 98, pp. 609-617).

magnification. Assuming that the source exitance is uniform (as is the case for the fibers employed), the captured flux for this slice will be proportional to the differential area of the original slice.

Since the spatial information is “summed out” in the extraction, the equivalent width of a real rectangular source which would produce the same “summed out” (along y) distribution as the actual source can be found by weighting the differential widths of the constituent slices. This equivalent width is the *area-weighted width*, \bar{w} , and a mathematical description of it may be found in Appendix B along with a figure showing a differential slice for an arbitrary aperture. For a circular source, the area-weighted width can be found:

$$D_{\text{FIB}}^2 = x^2 + y^2 \quad [67]$$

$$g^2(y) = 4 \left[\left(\frac{D_{\text{FIB}}}{2} \right)^2 - y^2 \right] \quad [68]$$

$$\bar{w} = \frac{\int_{-D_{\text{FIB}}/2}^{D_{\text{FIB}}/2} 4 \left[\left(\frac{D_{\text{FIB}}}{2} \right)^2 - y^2 \right] dy}{\frac{\pi D_{\text{FIB}}^2}{4}} \quad [69]$$

$$= \frac{8}{3\pi} D_{\text{FIB}} \quad [70]$$

Now then, a rectangular aperture of this width will produce the same distribution of flux as the circle if the flux is summed along the spatial direction. The next step is to find the RMS full-width of a rectangular distribution. Consider a normalized uniform distribution, $p(x)$ having a width w , height, w^{-1} , and centered at $x = 0$:

$$\sigma^2 = \int x^2 p^2(x) dx \quad [71]$$

$$= \int_{-\frac{w}{2}}^{\frac{w}{2}} x^2 \frac{1}{w} dx \quad [72]$$

$$= \frac{1}{12} w^2 \quad [73]$$

$$2\sigma = \frac{w}{\sqrt{3}} \quad [74]$$

So, the RMS-full width of a rectangular distribution, 2σ , is equal to its width divided by $\sqrt{3}$. Combining Equations 70 and 74 and taking into account the spectral magnification, the RMS full-width of the fiber is then estimated to be:

$$w_{\text{IMG}} = D_{\text{FIB}} \frac{8}{3\pi\sqrt{3}} m_\lambda \quad [75]$$

To validate this model, a circular distribution was generated on a 25 by 25 grid representing a fiber. Rather than being traced from a theoretical point source, rays were then traced from each position of the grid where there is a 1. The size of the grid was set to 250 μm at the entrance to the spectrograph.

```

0 0 0 0 0 0 0 0 0 0 1 1 1 1 1 0 0 0 0 0 0 0 0 0
0 0 0 0 0 0 0 1 1 1 1 1 1 1 1 1 1 0 0 0 0 0 0 0
0 0 0 0 0 1 1 1 1 1 1 1 1 1 1 1 1 1 1 0 0 0 0 0
0 0 0 0 1 1 1 1 1 1 1 1 1 1 1 1 1 1 1 1 0 0 0 0
0 0 0 1 1 1 1 1 1 1 1 1 1 1 1 1 1 1 1 1 1 0 0 0
0 0 1 1 1 1 1 1 1 1 1 1 1 1 1 1 1 1 1 1 1 1 0 0
0 0 1 1 1 1 1 1 1 1 1 1 1 1 1 1 1 1 1 1 1 1 0 0
0 1 1 1 1 1 1 1 1 1 1 1 1 1 1 1 1 1 1 1 1 1 1 0
0 1 1 1 1 1 1 1 1 1 1 1 1 1 1 1 1 1 1 1 1 1 1 0
0 1 1 1 1 1 1 1 1 1 1 1 1 1 1 1 1 1 1 1 1 1 1 0
1 1 1 1 1 1 1 1 1 1 1 1 1 1 1 1 1 1 1 1 1 1 1 1
1 1 1 1 1 1 1 1 1 1 1 1 1 1 1 1 1 1 1 1 1 1 1 1
1 1 1 1 1 1 1 1 1 1 1 1 1 1 1 1 1 1 1 1 1 1 1 1
1 1 1 1 1 1 1 1 1 1 1 1 1 1 1 1 1 1 1 1 1 1 1 1
1 1 1 1 1 1 1 1 1 1 1 1 1 1 1 1 1 1 1 1 1 1 1 1
0 1 1 1 1 1 1 1 1 1 1 1 1 1 1 1 1 1 1 1 1 1 1 0
0 1 1 1 1 1 1 1 1 1 1 1 1 1 1 1 1 1 1 1 1 1 1 0
0 1 1 1 1 1 1 1 1 1 1 1 1 1 1 1 1 1 1 1 1 1 1 0
0 0 1 1 1 1 1 1 1 1 1 1 1 1 1 1 1 1 1 1 1 1 1 0
0 0 1 1 1 1 1 1 1 1 1 1 1 1 1 1 1 1 1 1 1 1 1 0
0 0 0 1 1 1 1 1 1 1 1 1 1 1 1 1 1 1 1 1 1 1 1 0
0 0 0 0 1 1 1 1 1 1 1 1 1 1 1 1 1 1 1 1 1 1 1 0
0 0 0 0 0 1 1 1 1 1 1 1 1 1 1 1 1 1 1 1 1 1 1 0
0 0 0 0 0 0 1 1 1 1 1 1 1 1 1 1 1 1 1 1 1 1 1 0
0 0 0 0 0 0 0 1 1 1 1 1 1 1 1 1 1 1 1 1 1 1 1 0
0 0 0 0 0 0 0 0 1 1 1 1 1 1 1 1 1 1 1 1 1 1 1 0
0 0 0 0 0 0 0 0 0 1 1 1 1 1 1 1 1 1 1 1 1 1 1 0

```

Figure 44, Model of Circular Object (Fiber) From 25^2 Grid

After the rays were traced to the focal surface, statistics were performed to determine the RMS full-width, denoted w_2 . This was then checked with the computed value given by combining w_{PSF} (found by ray tracing also) and w_{IMG} in quadrature, denoted w_1 . This comparison is made for the on-axis and off-axis case ($y = 0, \bar{y}_{\text{FIB}}$) for five wavelengths distributed evenly across the CCD. The following table summarizes the results and demonstrates the validity of the method.

		Wavelength				
Field		.5503 μ	.5581 μ	.5655 μ	.5725 μ	.5788 μ
	φ	15.922°	13.480°	11.013°	8.509°	6.074°
	$m\lambda$.165	.175	.188	.202	.219
	w_{IMG}	20 μ	21 μ	23 μ	25 μ	27 μ
0 mm	w_{PSF}	79 μ	62 μ	33 μ	58 μ	57 μ
	w_1	81 μ	66 μ	40 μ	63 μ	63 μ
	w_2	81 μ	66 μ	40 μ	62 μ	64 μ
38.1 mm	w_{PSF}	74 μ	61 μ	37 μ	59 μ	57 μ
	w_1	77 μ	65 μ	43 μ	64 μ	63 μ
	w_2	78 μ	65 μ	44 μ	64 μ	62 μ

Table 18, Validation of the Model for w_{IMG}

The third term of Equation 66, w_{PIX} , represents the degradation due to finite sampling of the CCD at the focal surface. The determination of w_{PIX} is made empirically. A hypothesis is made that it is simply the RMS full-width of a uniform distribution having a width given by that of a single pixel ($x_{\text{PIX}} = 24 \mu\text{m}$). Certainly, for the case of a theoretically small image, all the flux is directed into one pixel and the measured RMS full-width would be that of a single pixel:

$$w_{\text{PIX}} = \frac{x_{\text{PIX}}}{\sqrt{3}} \quad [76]$$

$$= 13.9 \mu \quad [77]$$

The validity of this model was tested by tracing rays through a model of the spectrograph from a theoretical point source and then binning the resultant x locations in the focal surface as though the image was captured by 24 μm wide pixels. Then a statistical analysis was made to find the RMS full-width of the recorded image, denoted w_4 . This was then compared with the combination of w_{IMG} and w_{PIX} in quadrature, denoted w_3 . This comparison is made for the on-axis and

off-axis case ($y = 0, \bar{y}_{\text{FIB}}$) and for three wavelengths distributed from the blue edge to the center of the CCD. The results show a good correspondence, validating Equation 76.

		Wavelength		
		.5503 μ	.5581 μ	.5655 μ
	w_{PIX}	14 μ	14 μ	14 μ
0 mm	w_{IMG}	81 μ	66 μ	40 μ
	w_3	82 μ	68 μ	42 μ
	w_4	83 μ	67 μ	42 μ
38.1 mm	w_{IMG}	78 μ	65 μ	44 μ
	w_3	79 μ	66 μ	46 μ
	w_4	81 μ	66 μ	46 μ

Table 19, Validation of the Model for w_{PIX}

The final term that enters into the image quality, w , is an estimate of the effects due to diffraction. The two principal effects are a broadening of the imagery at the focal surface due to the diffraction from the grating itself and that from the imaging properties of the camera:

$$w_{\text{DIFF}} = \sqrt{w_{\text{GRAT}}^2 + w_{\text{CAM}}^2} \quad [78]$$

The intent is to make good first order estimates of each of these diffraction effects and check the impact on the overall imagery, not to do a rigorous diffraction analysis. With the very complex vignetting patterns present in this system and with a probable complex apodization of the pupil due to the mode scrambling properties of the fibers, the latter could be material enough for a thesis.

The broadening effect due to the diffraction of the grating is a result of the finite extent of the illuminated portion of the grating. Each diffracted radiant intensity peak, $I(\varphi)$, is a sinc pattern as from multiple slits, and corresponds to a diffraction order. The width in φ for each peak is inversely proportional to the width of the illuminated portion of the grating and is given by²⁹:

$$\sin(\Delta\varphi) = \frac{\lambda}{w_{\text{GRAT}}} \quad [79]$$

Where here, $\Delta\varphi$ is the angular half-width of the peak (to the first zero) and w_{GRAT} is the illuminated portion of the grating (see Figure 43). If we assume the angular full width of the distribution to be approximately equal to the RMS full width, the spread in the focal surface can be related by the geometry:

$$\frac{\lambda}{w_{\text{GRAT}}} \cong \frac{w_{\text{GRAT}}}{2f_{\text{CAM}}} \quad [80]$$

$$w_{\text{GRAT}} \cong \frac{2f_{\text{CAM}}\lambda}{w_{\text{GRAT}}} \quad [81]$$

This assumes that the angle $\Delta\varphi$ is small and that the illuminated portion is rectangular. The latter assumption is not valid and should be modified so that the broadening is slightly larger than that from a rectangular beam of width w_{GRAT} at the grating. This broadening from an elliptical beam, having an axis in the x direction of w_{GRAT} , can be estimated by using the area-weighted width (see Appendix B) of the ellipse instead:

$$w_{\text{GRAT}} \equiv \frac{2 f_{\text{CAM}} \lambda}{\bar{w}_{\text{GRAT}}} \quad [82]$$

$$\equiv 2\lambda \left(\frac{3\pi}{8} \right) \frac{f_{\text{CAM}}}{f_{\text{COL}}} \cos(\alpha) (f/\#)_{\text{FIB}} \quad [83]$$

Now there is only one more effect which should be added into this model. That is the effect from the field dependent vignetting. Vignetting of the elliptical beam at the mouth of the objective will have the effect of reducing the beam size. If the peculiar shape of the vignetting is ignored, a reasonable first order approximation of the additional broadening is to consider the effective illuminated footprint on the grating reduced by the vignetting factor, ϵ_v . Adding this to Equation 83 and re-writing the center portion in terms of the spectral magnification yields:

$$w_{\text{GRAT}} \equiv 2.36\lambda m_\lambda \cos(\alpha - \varphi) \frac{(f/\#)_{\text{FIB}}}{\epsilon_v} \quad [84]$$

The second broadening effect is the diffraction due to the finite aperture associated with the imaging properties of the camera. If the objective clipped an otherwise unvignetted beam in a circular fashion, one would expect an Airy pattern. Two assumptions are made. First, the RMS full width is estimated to be approximately equal to two times the Airy disk radius³⁰. This is, of course, not true rigorously. Secondly, as before, the effect of vignetting is accounted for by assuming the beam to be circular with a width (diameter) given by $w_{\text{CAM}} \cdot \epsilon_v$:

$$w_{\text{CAM}} = \cos(\alpha - \varphi) w_{\text{GRAT}} \quad [85]$$

$$= f_{\text{COL}} \frac{\cos(\alpha)}{\cos(\alpha - \varphi)} \frac{1}{(f/\#)_{\text{FIB}}} \quad [86]$$

$$w_{\text{CAM}} \cong 2.44\lambda \frac{f_{\text{CAM}}}{w_{\text{CAM}}} \quad [87]$$

$$\cong 2.44\lambda \frac{f_{\text{CAM}} \cos(\alpha - \varphi)}{f_{\text{COL}} \cos(\alpha)} (f/\#)_{\text{FIB}} \quad [88]$$

$$\cong 2.44\lambda m_\lambda \frac{(f/\#)_{\text{FIB}}}{\epsilon_v} \quad [89]$$

Combining Equations 84 and 89 into Equation 78, a rough estimate of the diffraction effects can be found to be:

$$w_{\text{DIFF}} \cong \frac{\lambda m_\lambda (f/\#)_{\text{FIB}}}{\epsilon_v} \sqrt{2.44^2 + [2.35 \cos(\alpha - \varphi)]^2} \quad [90]$$

An estimate for the net diffraction effect may be found by measuring its influence on a typical system. This is done for two cases. The first represents a typical spectrograph configuration with data determined for no field ($y = 0$ mm) and the second for data at the extreme field ($y = \bar{y}_{\text{FIB}}$) exhibiting approximately twice the vignetting. The five wavelengths represent those which are evenly distributed across the CCD, the third wavelength (.5655 μm) being the chief wavelength which propagates in the direction of φ_c (11°). The vignetting data is from ray tracing a 68^2 grid through a model spectrograph. w_5 is the combined effect of all the image width terms other than diffraction (w_{PSF} , w_{IMG} , and w_{PIX}). w_6 is the combination of w_{DIFF} and w_5 (all four terms) and Effect is the fractional difference between w_5 and w_6 , hence the additional estimated effect of diffraction. It is on the

order of less than 1%. So, even if the rough estimate of the diffraction effect was off by a factor of two, the estimated effect would not significantly degrade the model.

	Wavelength				
	.5503 μ	.5581 μ	.5655 μ	.5724 μ	.5788 μ
ϕ	15.92°	13.48°	11.01°	8.55°	6.07°
$m\lambda$.17	.18	.19	.20	.22
Case 1, No Field (Low Vignetting)					
Vignetting	40%	58%	78%	61%	40%
w_{DIFF}	3.8 μ	2.8 μ	2.2 μ	3.0 μ	5.1 μ
w_{IMG}	64.7 μ	12.3 μ	81.0 μ	10.8 μ	50.8 μ
w_5	69.2 μ	28.4 μ	85.3 μ	30.3 μ	59.1 μ
w_6	69.3 μ	28.5 μ	85.4 μ	30.5 μ	59.3 μ
Effect	0.2%	0.5%	0.0%	0.5%	0.4%
Case 2, Extreme Field (High Vignetting)					
Vignetting	29%	40%	46%	39%	22%
w_{DIFF}	5.2 μ	4.1 μ	3.8 μ	4.8 μ	9.1 μ
w_{IMG}	66.4 μ	15.9 μ	49.0 μ	20.3 μ	57.9 μ
w_5	70.8 μ	30.1 μ	55.9 μ	34.9 μ	65.3 μ
w_6	71.0 μ	30.4 μ	56.0 μ	35.2 μ	65.9 μ
Effect	0.3%	0.9%	0.2%	1.0%	1.0%

Table 20, Summary of Diffraction Effects

8.2.6 The Noise Term

The last of three terms to be assembled into the relative information gathering power (Equation 59) is the field dependent level of RMS noise $\bar{n}(x,y)$. Its interpretation is the amount of noise per resolution element. It can be written as the sum of component sources in quadrature. Each component will be described in the order presented in the following equation:

$$\bar{n} = \sqrt{\bar{n}_{\text{DARK}}^2 + \bar{n}_{\text{SCAT}}^2 + \bar{n}_{\text{hv}}^2 + \bar{n}_{\text{SKY}}^2 + \bar{n}_{\text{READ}}^2} \quad [91]$$

1. The quantity \bar{n}_{DARK} is the thermally induced dark noise. Since the dewar is cooled to LN₂ temperature, this noise is virtually eliminated and will not be considered. It is proportional, though, to the integration time.
2. The quantity \bar{n}_{SCAT} represents the noise related to scattered light. Scattered light may come from two sources, the fibers themselves and sources external to the spectrograph. For the latter, considerable effort was placed on insuring that the spectrograph environment is as dark as possible. This included analyzing wall paints, fixture paints, and the floor tile for phosphorescence. Feedthroughs and doors have been redundantly sealed. Fiber optic cables and connectors have been jacketed. The environment was imaged to verify that no external sources are present.

Scattered light can also result from vignetting, reflections, and refractions in the spectrograph. There are prudent steps that are taken to minimize ill effects. These include keeping the optics clean and re-aluminizing the collimator periodically. Also, high quality broad anti-reflection coatings have been employed and all surfaces which vignette the beam are blackened. This is especially important for those surfaces which are nearly parallel to the beam since grazing incidence reflections are typically very high and can manifest ghost images. Normal blackening, such

as with paint or anodizing, is virtually useless. Surface roughening techniques and flocking have been utilized in this regard. It is assumed that these precautions enable the noise from scattered light to be negligible.

3. The quantity \bar{n}_{iv} represents the inherent statistical photon noise, which is approximately equivalent to the square root of the signal and hence integration time. The goal is to be photon noise limited, not instrument noise limited. Since there is no control over the source radiances, it will be assumed that the photon noise is zero in an effort to minimize the other noise sources as much as possible.
4. The quantity \bar{n}_{BACK} is the amount of sky background noise. This is extraneous flux scattered by the atmosphere and admitted into each fiber along with the source flux. It is possible to optimize the SNR by selecting the best fiber diameter. In the spectrograph, though, a fixed ratio of source to non-source flux will be imaged onto each resolution element. This quantity is not dependent on any property of the spectrograph. It is constant.
5. The quantity \bar{n}_{READ} is the so called read noise associated with reading out, amplifying, and converting the charge in the detector to a digital level. The amount of read noise is proportional to the number of pixels, and hence the area read out per resolution element. If it is assumed that the integrated height along y is fixed over the spectra, the read noise will then be

proportional to the width, w , of each resolution element. So the read noise will be field dependent and related to the imagery.

The two primary sources of noise then are sky background and read noise.

$$\bar{n} \equiv \sqrt{\bar{n}_{\text{SKY}}^2 + \bar{n}_{\text{READ}}^2} \quad [92]$$

$$\equiv \sqrt{C_{\text{SKY}}^2 + (C_{\text{READ}} \cdot w)^2} \quad [93]$$

The constants of proportionality C_{SKY} and C_{READ} can be absorbed into a ratio of the amounts of sky background to read noise, R_{SB} :

$$R_{\text{SB}} = \frac{C_{\text{SKY}}}{C_{\text{READ}}} \quad [94]$$

$$\bar{n}(x, y) \equiv \sqrt{R_{\text{SB}}^2 + w^2(x, y)} \quad [95]$$

When the sky background noise is dominant, the noise term will be scalar like. This will normally be the case during “bright time”, when the phase of the moon is such that roughly half or better is visible. During “dark time”, the moon will be less conspicuous and read noise will dominate, causing the noise to be more proportional to the RMS full-width, w . Since the noise term enters into the denominator of \mathcal{P}_{REL} , during dark time, the preferred configuration will tend to be the one with better imagery (at the expense, for example, of transmission). For the analysis section (Chapter 9), the relative potential information gathering power will be ascertained for three cases sky background, low ($R_{\text{SB}} = 0$), medium ($R_{\text{SB}} = 1 \times 10^3$), and high ($R_{\text{SB}} = 1 \times 10^6$).

8.3 OPTIMIZING

Before the analysis of each configuration can be made, each configuration must be optimized to produce the highest \mathcal{P}_{REL} within the configuration by adjusting the free parameters (see Section 6.2.2). The goal of each optimization is to produce the best balanced imagery over the field. This is a very time consuming task, measuring in days per configuration.

First, it should be said that the optimization of the imagery has two requirements:

1. That the imagery be measured with respect to the centroid, not the chief ray for each image.
2. That vignetted rays not be included in the computation of the image quality.

Both of these are a result of the large complex vignetting properties of the instrument. In fact, all chief rays and a central part of the beam produced by each fiber are vignetted by the foot. These requirements insure that there is no bias against asymmetrical aberrations such as coma where the centroid and chief ray are displaced.

An optimization operand meeting these requirements is now available with the software package, but with one caveat. It is only available as a measure of the RMS **radius** of image, not as width in one direction. However, this provides an insurance that the imagery in the y direction remains acceptable. Until now, it has been assumed that in the spatial sense, the spectra are separated, *i.e.*, that the flux from one fiber does not “bleed” into the spectrum for an adjacent fiber. By

optimizing the imagery with respect to the RMS radius, it insures that the imagery in the spatial direction is not compromised.

There are three ways to mitigate the time requirement for optimization:

1. Choosing an appropriate ray density in the pupil: This does not have to be the same quantity as that for performing analyses. All that is required is for the sampling to be enough so that the free parameters are optimized to within small enough tolerances of the values determined with a larger ray density. The resultant configuration must yield the same results.
2. Using a smaller representative sample of the 9λ by $9 y$ combinations used for analyses: As mentioned in Section 8.2.3, the sampling of wavelength is somewhat critical but the sampling in the spatial sense is more than enough with 9 field positions. So, the sampling was reduced to 5 field positions for the optimization.
3. Avoid global optimization: This technique was tested and in fact, in some cases, substantial changes in the free parameters were made. However, in the final analysis of potential information gathering power, the only noticeable change was in the large amount of additional time expended.

Finally, the usual course of reality constraints had to be incorporated into the optimization process. These include making sure that the thicknesses and curvatures of elements remain reasonable and allowances are made for opto-

mechanical considerations. The following table summarizes the optimized free parameters for each configuration:

Row	Configuration				Δz_{BFD}	Θ	Δz_{COL}
	ϕ_c	Col	Δz_{COL}	FL			
1	11°	Old			7.46 mm	.035°	1007.1 mm
2		Old	√		7.51 mm	.043°	1006.2 mm
3		Old	√	√	7.55 mm	.050°	978.7 mm
4		Size			7.46 mm	.035°	1007.1 mm
5		Size	√		7.51 mm	.043°	1006.2 mm
6		Size	√	√	7.51 mm	.044°	978.1 mm
7		SFL			7.46 mm	.030°	900.4 mm
8		SFL	√		7.49 mm	.036°	899.9 mm
9		SFL	√	√	7.48 mm	.032°	871.4 mm
10	15°	Old			7.46 mm	.011°	1007.1 mm
11		Old	√		7.48 mm	.016°	1006.5 mm
12		Old	√	√	7.47 mm	.014°	978.1 mm
13		Size			7.46 mm	.011°	1007.1 mm
14		Size	√		7.48 mm	.016°	1006.5 mm
15		Size	√	√	7.47 mm	.013°	977.3 mm
16		SFL			7.45 mm	.018°	900.4 mm
17		SFL	√		7.45 mm	.020°	900.3 mm
18		SFL	√	√	7.49 mm	.024°	871.8 mm
19	19°	Old			7.45 mm	.014°	1007.1 mm
20		Old	√		7.45 mm	.014°	1007.0 mm
21		Old	√	√	7.46 mm	.012°	978.1 mm
22		Size			7.45 mm	.014°	1007.1 mm
23		Size	√		7.45 mm	.014°	1007.0 mm
24		Size	√	√	7.46 mm	.006°	977.3 mm
25		SFL			7.44 mm	-.016°	900.4 mm
26		SFL	√		7.44 mm	-.016°	900.5 mm
27		SFL	√	√	7.44 mm	-.015°	871.5 mm

Table 21, Summary of Free Parameters

The first row is the configuration of the unmodified spectrograph. After the row designator, the next group of four columns describes each configuration. After the camera-collimator angle (ϕ_c), there is a description of the collimator, which is either unmodified (Old), one having a larger aperture (Size), or both a larger

aperture and a shorter focal length (SFL). The next two columns show whether the collimator focus is allowed to vary (Δz_{COL}) and/or a field lens (FL) included. The next two columns show the free parameters common to all configurations, back focal distance (Δz_{BFD}) and dewar azimuth (Θ). The sixth column is the *value* for Δz_{COL} . For the cases where the second column is unchecked, the value of Δz_{COL} will be that for a first order computation, placing the collimator exactly one focal length away from the object (compensating for the reduced distances). Δz_{COL} is measured from the rear of either the interference filter, or field lens if used, to the collimator vertex.

ϕ_c	Col	Δz_{SEP}	Δz_{THK}	R_1	R_2	\bar{u}	L_2
11°	Old	4.43 mm	4.13 mm	-319 mm	-500 mm	.0221	1627 mm
	Size	5.35 mm	5.04 mm	-232 mm	-406 mm	.0361	2009 mm
	SFL	5.20 mm	6.35 mm	-242 mm	-562 mm	.0460	1923 mm
15°	Old	4.45 mm	6.72 mm	-398 mm	-694 mm	.0209	1594 mm
	Size	5.38 mm	7.00 mm	-230 mm	-392 mm	.0349	1977 mm
	SFL	5.98 mm	3.87 mm	-196 mm	-338 mm	.0419	1833 mm
19°	Old	4.43 mm	6.83 mm	-344 mm	-432 mm	.0114	1333 mm
	Size	5.35 mm	7.00 mm	-232 mm	-369 mm	.0310	1870 mm
	SFL	6.15 mm	5.35 mm	-188 mm	-298 mm	.0383	1756 mm

Table 22, Summary of Field Lens Parameters

This table shows the free parameters for the configurations having a field lens. After the first two columns which identify the configuration, are four columns showing the opto-mechanical parameters. These are the separation from the rear of the interference filter to the front of the lens (Δz_{SEP}), the lens thickness (Δz_{THK}), and the front and rear radii (R_1 and R_2). Without exception, the lenses are each negative menisci shaped to be somewhat concentric about the fiber array. The final two columns relate to the optimally determined re-imaging of the spatial

pupil. The chief ray angle leaving the field lens (\bar{u}) and approximate location of the spatial pupil (L_2) are given.

There are two trends that are evident. First, as φ_c is increased, the camera is moved closer to the grating. The optimal location of the spatial pupil (L_2) shifts back as well as it becomes easier to simultaneously minimize the vignetting at the collimator (in the case of the old small aperture collimator), grating, and objective. Secondly, regardless of φ_c , opening up the aperture of the collimator allows the location of the spatial pupil that manifests the least vignetting to move away from the collimator, farther down the optical path toward the grating and objective. Reducing the beam size by utilizing a collimator with a shorter focal length reduces the vignetting further by allowing the objective to be placed closer to the grating (smaller L_1). This permits the spatial pupil (L_2) to be similarly shifted back.

9. ANALYSIS

9.1 RESULTS

Row	Configuration				w_{PSF}	ϵ_y	ϵ/w	\mathcal{P}_{REL}		
	ϕ	Col	Δz_{COL}	FL				Lo Rsb	Mid Rsb	Hi Rsb
1	11°	Old			1.00	1.00	1.00	1.00	1.00	1.00
2		Old	√		1.00	1.00	1.00	1.00	1.01	1.01
3		Old	√	√	1.04	1.07	1.03	1.02	1.03	1.03
4		Size			1.00	1.00	1.00	1.00	1.00	1.00
5		Size	√		1.00	1.00	1.00	1.00	1.01	1.01
6		Size	√	√	1.05	1.14	1.09	1.06	1.08	1.08
7		SFL			.99	1.10	1.11	1.12	1.11	1.11
8		SFL	√		.98	1.09	1.11	1.13	1.12	1.11
9		SFL	√	√	1.03	1.22	1.19	1.14	1.16	1.17
10	15°	Old			1.23	1.00	.82	.77	.78	.80
11		Old	√		1.23	1.00	.81	.78	.79	.81
12		Old	√	√	1.25	1.08	.86	.80	.80	.83
13		Size			1.23	1.00	.82	.77	.78	.80
14		Size	√		1.23	1.00	.81	.78	.79	.81
15		Size	√	√	1.27	1.13	.89	.82	.83	.86
16		SFL			1.23	1.12	.91	.86	.87	.90
17		SFL	√		1.23	1.12	.91	.87	.87	.90
18		SFL	√	√	1.30	1.22	.94	.89	.90	.93
19	19°	Old			1.46	.94	.64	.46	.50	.55
20		Old	√		1.46	.94	.64	.46	.50	.55
21		Old	√	√	1.47	.95	.65	.44	.48	.53
22		Size			1.46	.94	.64	.46	.50	.55
23		Size	√		1.46	.94	.64	.46	.50	.55
24		Size	√	√	1.48	1.05	.71	.49	.54	.59
25		SFL			1.43	1.04	.73	.54	.58	.63
26		SFL	√		1.43	1.04	.73	.54	.58	.63
27		SFL	√	√	1.50	1.13	.75	.53	.57	.63

Table 23, Summary of \mathcal{P}_{REL}

After each of the 27 configurations was optimized, a spreadsheet was used to assemble the parts that make up \mathcal{P}_{REL} and the summations over field (y) and wavelength (x) were performed. This was done for the three values of the relative

ratio of sky background to read noise, R_{SB} . In each case, the resultant quantity was divided by the value determined for the unmodified configuration (1st row).

The 5th and 6th columns (w_{PSF} , ϵ_v) show the output from the ray trace model **averaged** over the 2 dimensional field relative to the unmodified configuration. Notice that any gains realized in the vignetting by increasing the camera-collimator angle are overwhelmingly offset by the growth of the images for a theoretical point source. The reason for this is a strong dependence of the imagery on the anamorphic factor. As ϕ_c is increased, the beam width widens. This in turn forces the camera objective to operate at a higher effective speed (lower effective $f/\#$), increasing aberrations. The seventh column shows the quotient of the average amount of unvignetted light and the average w_{PSF} . It actually is a good indication of the relative information gathering power for moderate values of the anamorphic factor. Note how this correspondence degrades as ϕ_c increases.

The last three columns show the relative information gathering power for increasing amounts of sky background noise. The conclusion that is immediately apparent is the dependence on the camera-collimator angle. The degradation with increasing ϕ_c is strong and monotonic. This is a confirmation of earlier rules of thumb which suggested that the spectrograph should be operated as close to Littrow as possible.

Allowing the collimator focus to deviate from the first order position improves the performance by 1%. Adding a field lens yields a 2-3% increase. As expected, increasing the size of the collimator without a field lens is meaningless. When the field lens and larger collimator are combined, a noticeable improvement of 6-8% may be realized. Changing the focal length and increasing the size of the

collimator has the greatest single effect ($\cong 12\%$). When this is combined with a field lens, the best configuration is found, with a nominal improvement between 14% and 17%.

An interesting point can be found by contrasting configurations with and without a field lens. For example, consider rows 7-9, where for the $\phi_c = 11^\circ$ case, a larger sized and shorter focal length collimator is used. When the field lens is not employed (rows 7-8), the average imagery (w_{PSF}) is better than the unmodified case. These two configurations perform better in the low sky background condition, for \mathcal{P}_{REL} is higher than for the mid and high sky background conditions. The next configuration (row 9) has worse imagery but better vignetting than these two. And, the performance with sky background is reversed. This reversal is due to the fact that in the low sky background condition, the denominator of integrand (summand) for \mathcal{P}_{REL} is more quadratic with w as opposed to linear, shifting some dependence from transmission to imagery.

The best overall configuration is the one represented in the 9th row. Here, the camera-collimator angle is set to its minimum allowable value, a larger collimator is employed with a shorter focal length, and a field lens is utilized. Depending on the amount of sky background noise, a 14% to 17% increase in the information gathering power may be realized.

9.2 FIELD LENS MATERIAL

The material chosen and used so far for the lens has been BK7. This is the most common optical glass type and for good reason. It has very good mechanical and optical properties. It is also very easy to work with and is inexpensive. In terms of

its refractive properties, it has a mild index and relatively high Abbe number. The latter implies a relatively low dispersion so that the power of the lens changes little with wavelength. This is important in that the position of the spatial pupil will stay close to the optimal position, keeping the vignetting as low as possible, regardless of which wavelength range is used.

The one property of the lens which could be construed as less than ideal is the index, which is fairly low, $n_d \cong 1.517$. In general, lenses with greater index have more power per given curvature. As such, they tend to have lower angles of incidence and hence produce lower aberration. So, as a check to see if the potential information gathering power could be improved, the glass type was changed to LaKN22. This also is a preferred glass* with low dispersive and mechanical properties, though not as good as BK7. The index, however, is much higher, $n_d \cong 1.653$. The best configuration ($\phi_c = 11^\circ$, $f_{COL} = 914$ mm) was re-optimized with a field lens made of this higher index glass.

	BK7	LaKN22
ΔZ_{SEP}	5.20 mm	5.21 mm
ΔZ_{THK}	6.35 mm	7.00 mm
R_1	-242 mm	-242 mm
R_1	-562 mm	-442 mm
R_{SB}	\mathcal{P}_{REL}	
Lo	1.14	1.15
Mid	1.16	1.16
Hi	1.17	1.17

Table 24, Comparison of Field Lens Material

* It is colored red on the Schott glass map, indicating good availability.

The powers of the two lenses are virtually equivalent. This is a result of forcing the exiting chief rays to have the same angle. Note that the optimization for the higher index glass configuration yields the same front radius (R_1). This is unexpected since it represents more power. In order for the total lens power to be the same, it must have a **stronger** back radius (R_2). So, the angles of incidence are actually greater with the higher index lens material.

For the low sky background case, the LaKN22 lens produces a 1% increase in \mathcal{P}_{REL} . This is the condition that places more emphasis on imagery and less on vignetting. The improvement is inconsequential and is lost once the sky background noise is raised at all. There really is no virtue in choosing a glass type other than the standard BK7.

9.3 OPTIMIZING ACROSS THE ENTIRE WAVELENGTH RANGE

So far, the design and analysis have been limited to a median wavelength region. Now that the optimal configuration has been identified, the design of the field lens should be revisited so that the entire wavelength range may be improved as much as possible. This is done by selecting two additional regions farther blue and red of the median region (referred to as “green”). These new regions coincide with the normal wavelength edges of the instrument. The wavelengths are computed as before (Section 8.1):

ϕ_c	11°	
α	69.355°	
Wavelength Region		
Blue	Green	Red
m = 14	m = 10	m = 7
.3931 μ	.5503 μ	.7861 μ
.3959 μ	.5543 μ	.7918 μ
.3987 μ	.5581 μ	.7973 μ
.4014 μ	.5619 μ	.8027 μ
.4040 μ	.5655 μ	.8079 μ
.4065 μ	.5691 μ	.8129 μ
.4089 μ	.5724 μ	.8178 μ
.4112 μ	.5757 μ	.8224 μ
.4134 μ	.5788 μ	.8269 μ

Table 25, Three Wavelength Regions

The next step is to optimize the free parameters of the system to “tune” the spectrograph for each wavelength region.

	Blue	Green	Red	AVG
Δz_{BFD}	8.35 mm	7.48 mm	7.90 mm	
Θ	-.320°	.032°	.138°	
Δz_{COL}	870.0 mm	871.4 mm	865.8 mm	
Δz_{SEP}	5.66 mm	5.20 mm	9.67 mm	6.84 mm
Δz_{THK}	7.00 mm	6.35 mm	7.00 mm	6.78 mm
R_1	-212.6 mm	-242.3 mm	-104.3 mm	-186.4 mm
R_2	-416.8 mm	-562.2 mm	-141.6 mm	-332.9 mm
n	1.5304	1.5179	1.5107	
Paraxial Power	-.001208 1/mm	-.001208 1/mm	-.001208 1/mm	-.001208 1/mm
...of Avg Params	-.001232 1/mm	-.001203 1/mm	-.001187 1/mm	-.001207 1/mm
Δel^2	5.995590535	0.209012604	4.326981351	10.53158449

Table 26, Free Parameters for Each Region

At this point, the parameters of the field lens need to be combined and frozen. The method of doing this is to average the optimized values for Δz_{SEP} , Δz_{THK} , and R_1 . The final value for the rear curvature (R_2) can not be determined this way. The

reason for this is that the purpose of the field lens is to re-direct the chief ray and re-image the spatial pupil to a specific location. Averaging the rear radii would yield a field lens with too much power. Instead, R_2 is determined by setting the powers of the final lens as close as possible to the nominal value. Note the last two rows of the table. The penultimate row shows the powers for each individualized lens. They are equivalent as each re-images the spatial pupil to the same point. Because of the lens dispersion, the final frozen design will not be able to hold this location constant. The final row shows how the power changes slightly for each region when the average lens parameters are used.

9.4 FINAL DESIGN

With this proposed field lens, there are still three free parameters that can be adjusted to optimize the performance for any wavelength region. They are Δz_{BFD} , Θ , and Δz_{COL} .

	Blue	Green	Red	AVG
Δz_{BFD}	8.36 mm	7.49 mm	7.90 mm	
Θ	-.32°	.03°	.13°	
Δz_{COL}	868.7 mm	869.2 mm	869.4 mm	
	\mathcal{P}_{REL}			
Lo	1.18	1.15	1.16	1.16
Mid	1.18	1.16	1.17	1.17
Hi	1.18	1.17	1.18	1.18

Table 27, Final Design Free Parameters and \mathcal{P}_{REL}

The combination of a new field lens and a modified collimator, then, is capable of increasing the relative information gathering power between 15% and 18% across the broad range the wavelengths used with the spectrograph in the high resolution

mode. In any case, the two remotely controllable foci (collimator and camera) and the dewar azimuth are adjusted to optimize the performance. The following figure shows a scale representation of the modified area in front of the fiber array. The parameters for the field lens are those given in Table 26 in the column labeled AVG. The rays shown below are from an actual ray trace for the center and edge fibers.

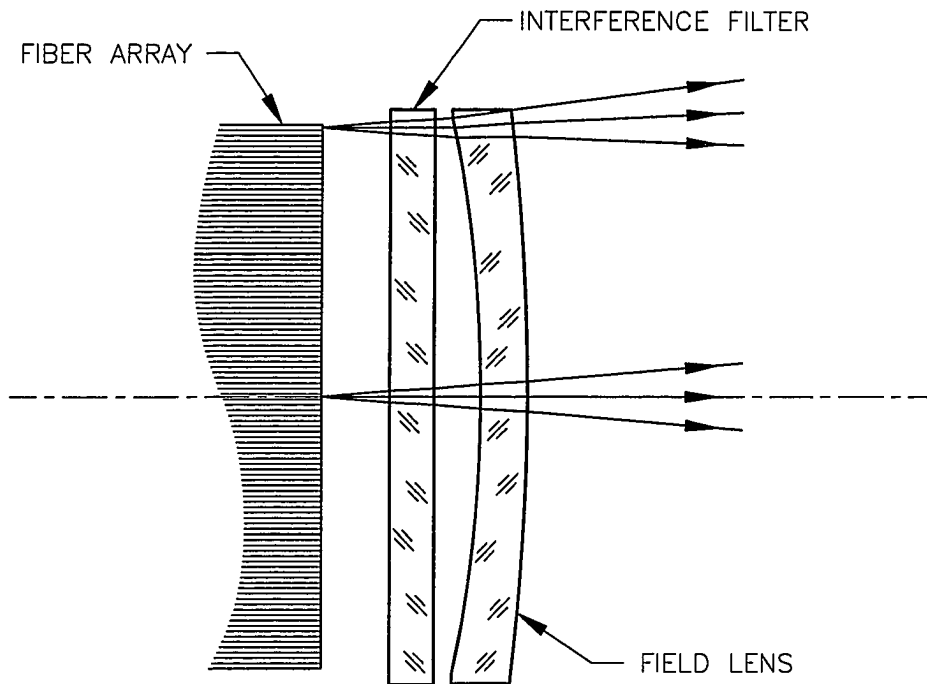


Figure 45, Final Design of the Field Lens

10. CONCLUSION

It is noteworthy that the driving principles in this system turn out to be those of first order optics, *e.g.*, placement of the spatial pupil, conjugates and magnification, radiometry, detector theory, and various losses due to vignetting, Fresnel reflections, and diffraction efficiency. The effects of aberrations and their control turn out to be less than expected (by the author). In fact, much more effort was expended in modeling the first order principles than in aberration control, and the best overall modification to the optical system turns out to be one with imagery worse than the unmodified system.

The potential information gathering power enables what is, in essence, a very complex system to be evaluated by a single figure of merit. This measure of performance is science-neutral, *i.e.*, it places no preference on any particular resolution and/or requirement for multiplex. Using potential information gathering power, trade-offs such as with resolution and efficiency can be quantified. A determination has been made that the best modification to the high resolution mode of the instrument is to shorten the focal length of the collimator from 1021 mm to 914 mm, increase the diameter from 241 mm to 292 mm, and to add a field lens with the parameters given in Table 26. In addition, improvement in the vignetting function by increasing the camera-collimator angle from $\varphi_c = 11^\circ$ and reducing the distance with which the camera objective must be separated from the grating should be forgone. The camera-collimator angle should remain as small or near Littrow as possible.

As is often the case, there are multiple ways to improve the performance of any given optical instrument. A further enhancement in the relative information gathering power is to divide \mathcal{P}_{REL} by the cost of any given set of modifications and/or additions. In this fashion, a cost benefit analysis may be performed. For example, with the Bench Spectrograph, a similar model to the one developed in this work could be applied to the problem of the inherent warp of the CCD. By normalizing each \mathcal{P}_{REL} by the estimated cost of the project, a determination may be made where one can get the “most bang for the buck”.

Finally, in the course of this work it has become apparent that certainly this is not the final word in the future development of the instrument. Both the modeling in the ray trace program of the RMS full-width and vignetting of the imagery is based on the assumption of a uniform distribution in the pupil. When the spectrograph becomes operational at WIYN, measurements of the actual fiber radiance distribution pattern should be made *in-situ*. It is expected that this will result in a closer match between the measured and computed vignetting function. Furthermore, if the fiber radiance pattern is measured to be significantly different from a uniform distribution, some additional work should be applied to modifying the calculation of the RMS full-width to reflect this.

11. APPENDIX A, GLOSSARY OF SYMBOLS

A_a	Area of a
A_a	Amplitude of a
d	The distance between successive grooves of a diffraction grating, inverse grating frequency
$C_{\#}$	General proportionality constants
D_a	The diameter of a
f_a	Focal length of a
$(f/\#)_a$	The f -number of a
F_{BACK}	The fraction of light incident upon the grating which strikes the back side of the blazed facet
$g(a)$	Arbitrary function of a
$h(a)$	Arbitrary function of a
$I(\varphi)$	Radiant intensity, $d\Phi/d\Omega$
k	Conic constant
$K_{\#}$	Sellmeier Coefficients
l_{SLIT}	The length of the "slit", equal to 2 times \bar{y}_{FIB}
$l_{\#}$	Sellmeier Coefficients
$L_{\#}$	General proportionality constants
L_1	The distance from the grating to the front of the camera objective along the camera axis
L_2	The approximate distance from the collimator to the spatial pupil along the unfolded collimator and camera axes

L_λ	Spectral radiance of the (astronomical) source
m	The diffraction order, an integer
m_{OFF}	The equivalent off-blaze order number, this is not an actual order but rather a measure of the degree with which a configuration is off-blaze
m_y	Spatial magnification
m_λ	Spectral magnification
M_y	Spatial simultaneity gain, the number of resolution elements in the spatial (or y) direction
M_λ	Spectral simultaneity gain, the number of resolution elements in the spectral (or x) direction
n_a	Refractive index of a
n_{FL}	Index of the field lens
\bar{n}_a	RMS noise of a
n_y	Fiber number, an integer between 1 and N_{FIB}
N_{FIB}	The total number of fibers within the “slit”
N_{SUR}	Number of surfaces
$p(x)$	A normalized probability distribution
P	Relative atmospheric pressure
\mathcal{P}	Potential information gathering power, designated as \mathcal{P}_{REL} when relative to some standard and expressed as a percentage of the standard
$P_\#$	General proportionality constants
r	Anamorphic factor
r	Radial position ($\sqrt{x^2 + y^2}$)

r_o	Radius for circular fit
R	Resolution, first order definition, a unitless number
R_a	Radius of a
R_{SB}	Sky background noise ratio (to read noise)
T	Transmission parameter of the system
T	Temperature
T_{AIR-GL}	Transmission of air/glass interface
\bar{u}	Chief ray angle
w_a	RMS full width of a computed/measured along the focal surface in the spectral or x direction unless otherwise specified
w_a	Width of a
\bar{w}_a	The area-weighted width of a
w_{PROJ}	Width of the grating projected onto a plane perpendicular to the collimator axis
x	The local coordinate perpendicular the direction of the propagating wavefront (for $\theta = 0$) and the spatial or field direction, hence the direction of diffraction or spectral coordinate
x_{PIX}	The width of a pixel (24 μm)
y	The local coordinate in the spatial direction
\bar{y}	Chief ray height
z	The direction of the propagating wavefront (for $\theta = 0$), in the post diffraction geometry, this applies to the chief wavelength only
Δz_{BFD}	The back focal distance, defined as the distance along z from the rear vertex of the last element of the camera objective to the front of the

dewar window

Δz_{COL}	The distance from the rear of the post slit optics (either the interference filter or field lens) to the vertex of the collimator
Δz_{THK}	Thickness of the field lens
Δz_{SEP}	Separation between the rear of the interference filter and the front of the field lens
Z_{POT}	A figure of merit given by Meaburn (see Equation 7)
α	The grating angle measured from the collimator axis to the grating normal in the xz plane, where 0° implies the Littrow condition, <i>i.e.</i> , the camera and collimator axes are collinear
β	The diffraction angle measured from the grating normal to the direction of the propagating diffracted wavefront in the xz plane
γ	The far-field phase difference in the diffracted wavefront between the center and edge of a blazed facet
δ	The grating blaze angle
ϵ	Efficiency
ϵ_{G}	The efficiency of the grating (diffraction)
ϵ_{T}	Transmission efficiency, includes anti-reflection coatings, absorption in glass (or SiO_2), and reflections from mirrored surfaces
ϵ_{V}	The fraction of unvignetting
ϵ_{O}	Efficiency for circular fit
θ	The field angle given by the chief ray, measured in the yz plane
Θ	The dewar/detector azimuth measured in the xz plane
λ	Wavelength
λ_{c}	The chief wavelength, the wavelength which is diffracted in the

	direction of φ_c
$\delta\lambda$	Resolution, the RMS full-width, w , in units of wavelength, defined less strictly for the first order case
$\Delta\lambda$	Free spectral range, a measure of an order's useful width in wavelength
v	Abbe number
ξ	Angular frequency
σ	Gaussian width parameter, RMS half-width
φ	The angle between the collimator axis and the direction of the propagating diffracted wavefront, a function of λ
φ_c	The angle between the camera and collimator axes
φ_o	Camera-collimator angle for circular fit
ϕ	Relative flux, the fraction of light from a real image of the telescope passed through the spectrograph aperture
Φ	Absolute flux, typical units are $\#/s \cdot \mu\text{m}$
$\Omega_{a,b}$	The projected solid angle of a as seen by b

12. APPENDIX B, AREA-WEIGHTED WIDTH

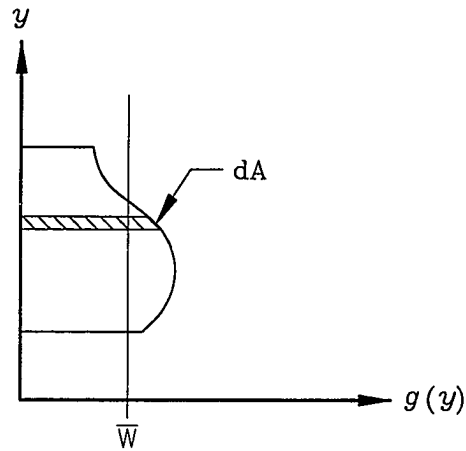


Figure 46, Area-Weighted Width

Area-weighted width is a mathematical concept. Numerically, it is larger than the average width. Here, $g(y)$ is an arbitrary function that represents a varying width. The differential area which “weights” the width is dA , the total area of the arbitrary function is A , and the area-weighted width is \bar{w} .

$$dA = g(y) dy \quad [96]$$

$$\bar{w} \equiv \frac{\int g(y) dA}{A} \quad [97]$$

$$= \frac{\int g(y)^2 dy}{A} \quad [98]$$

13. APPENDIX C, SOFTWARE MODEL OF THE SPECTROGRAPH

The spectrograph was modeled using Zemax. The following listing represents the model for a configuration with a camera-collimator angle of 11° , an enlarged collimator (aperture) with a modified focal length of 914 mm, and a BK7 field lens placed immediately behind the interference filter to re-image the spatial pupil to the location of minimum vignetting.

GENERAL LENS DATA:

```

Title           : THESIS SPECTROGRAPH
Surfaces        :           33
Stop            :           1
System Aperture :Object Space N.A.
Ray aiming      : Off
Gaussian Factor :   0.000000
Eff. Focal Len. :  -451.926
Total Track     :1.00081e+006
Image Space F/# :   0.00271157
Working F/#     :    1.47498
Obj. Space N.A. :   0.083045
Stop Radius     :   83332.8
Parax. Ima. Hgt.:   11.6425
Parax. Mag.     :  -0.305577
Entr. Pup. Dia. :   166666
Entr. Pup. Pos. :         0
Exit Pupil Dia. :   75.2093
Exit Pupil Pos. :   138.051
Maximum Field   :    38.1
Primary Wave    :   0.565500
Lens Units      : Millimeters
Angular Mag.    :  -2216.02

Fields          : 9
Field 1         : 0.00, 0.00 mm weight: 1.000000
Field 2         : 0.00, 4.76 mm weight: 0.000000
Field 3         : 0.00, 9.53 mm weight: 1.000000

```

Field 4 : 0.00, 14.29 mm weight: 0.000000
 Field 5 : 0.00, 19.05 mm weight: 1.000000
 Field 6 : 0.00, 23.81 mm weight: 0.000000
 Field 7 : 0.00, 28.58 mm weight: 1.000000
 Field 8 : 0.00, 33.34 mm weight: 0.000000
 Field 9 : 0.00, 38.10 mm weight: 1.000000

Wavelengths : 9
 Wavelength 1 : 0.550300 microns 1.000000 weight
 Wavelength 2 : 0.554300 microns 1.000000 weight
 Wavelength 3 : 0.558100 microns 1.000000 weight
 Wavelength 4 : 0.561900 microns 1.000000 weight
 Wavelength 5 : 0.565500 microns 1.000000 weight
 Wavelength 6 : 0.569100 microns 1.000000 weight
 Wavelength 7 : 0.572400 microns 1.000000 weight
 Wavelength 8 : 0.575700 microns 1.000000 weight
 Wavelength 9 : 0.578800 microns 1.000000 weight

SURFACE DATA SUMMARY:

Surf	Type	Radius	Thickness	Glass	Diameter	Conic
OBJ	STANDARD	Infinity	1000000		76.2	0
STO	STANDARD	Infinity	-1000000		166665.7	0
2	STANDARD	Infinity	9.8		0	0
3	INDEXDAT	Infinity	6.4		8	0
4	STANDARD	Infinity	5.201643		78.5276	0
5	STANDARD	-242.3284	6.348179	BK7	78.8562	0
6	STANDARD	-562.2233	15		80.66071	0
7	STANDARD	Infinity	5		84.98248	0
8	STANDARD	Infinity	871.3967		8	0
9	STANDARD	-1828.8	-914.4	MIRROR	254	-1
10	STANDARD	Infinity	-817.9		240.1551	0
11	COORDBRK	-----	0		0	-----
12	DGRATING	Infinity	0	MIRROR	440.5018	0
13	COORDBRK	-----	0		0	-----
14	COORDBRK	-----	0		0	-----
15	COORDBRK	-----	0		0	-----
16	STANDARD	Infinity	995.2		234.9517	0
17	STANDARD	423.6	25.46	AB	216.62	0
18	STANDARD	-3125.43	2.03		216.62	0

19 STANDARD	273.79	47.64	AB	216.02	0
20 STANDARD	-361.82	18.3	C	216.64	0
21 STANDARD	324.56	258.52		206.48	0
22 STANDARD	135.74	44.49	D	179.06	0
23 STANDARD	-802.12	13.81	E	179.06	0
24 STANDARD	1518.18	3.68		169.46	0
25 STANDARD	304.34	47.52	F	139.04	0
26 STANDARD	221.54	22.12	G	138.52	0
27 STANDARD	483.77	20.88		124.54	0
28 STANDARD	-142.6	4.93	H	77.98	0
29 STANDARD	618744	7.484173		80.52	0
30 COORDBK	-----	0		0	-----
31 STANDARD	Infinity	6.35	SILICA	101.6	0
32 STANDARD	Infinity	10.34	VACUUM	101.6	0
IMA STANDARD	1365	0		23.46941	-1682

SURFACE DATA DETAIL:

Surface OBJ : STANDARD
 Surface STO : STANDARD
 Surface 2 : STANDARD
 Surface 3 : INDEXDAT
 Index Nd : 1.53
 Abbe Vd : 65
 Aperture : Rectangular Aperture
 X Half Width : 2.38
 Y Half Width : 39.94
 Surface 4 : STANDARD
 Aperture : Rectangular Aperture
 X Half Width : 4
 Y Half Width : 41.5
 Surface 5 : STANDARD
 Aperture : Rectangular Aperture
 X Half Width : 4
 Y Half Width : 41.5
 Surface 6 : STANDARD
 Aperture : Rectangular Aperture
 X Half Width : 4
 Y Half Width : 41.5
 Surface 7 : STANDARD

Surface 8 : STANDARD
Surface 9 : STANDARD
Aperture : Circular Aperture
Minimum Radius : 0
Maximum Radius : 146
Surface 10 : STANDARD
Aperture : Rectangular Obscuration
X Half Width : 6.35
Y Half Width : 127
Y- Decenter : 73
Surface 11 : COORDBRK
Decenter X : 0
Decenter Y : 0
Tilt About X : 0
Tilt About Y : 69.355
Tilt About Z : 90
Surface 12 : DGRATING
Lines / Micron : 0.316
Diffract Order : 10
Aperture : Rectangular Aperture
X Half Width : 103
Y Half Width : 203
Surface 13 : COORDBRK
Decenter X : 0
Decenter Y : 0
Tilt About X : 0
Tilt About Y : 0
Tilt About Z : -90
Surface 14 : COORDBRK
Decenter X : 0
Decenter Y : 0
Tilt About X : 0
Tilt About Y : -69.355
Tilt About Z : 0
Surface 15 : COORDBRK
Decenter X : 0
Decenter Y : 0
Tilt About X : 0
Tilt About Y : 11
Tilt About Z : 0

Surface 16 : STANDARD
Surface 17 : STANDARD
Aperture : Circular Aperture
Minimum Radius : 0
Maximum Radius : 103.23
Surface 18 : STANDARD
Aperture : Circular Aperture
Minimum Radius : 0
Maximum Radius : 103.23
Surface 19 : STANDARD
Aperture : Circular Aperture
Minimum Radius : 0
Maximum Radius : 102.93
Surface 20 : STANDARD
Aperture : Circular Aperture
Minimum Radius : 0
Maximum Radius : 107.05
Surface 21 : STANDARD
Aperture : Circular Aperture
Minimum Radius : 0
Maximum Radius : 101.97
Surface 22 : STANDARD
Aperture : Circular Aperture
Minimum Radius : 0
Maximum Radius : 84.45
Surface 23 : STANDARD
Aperture : Circular Aperture
Minimum Radius : 0
Maximum Radius : 88.26
Surface 24 : STANDARD
Aperture : Circular Aperture
Minimum Radius : 0
Maximum Radius : 83.46
Surface 25 : STANDARD
Aperture : Circular Aperture
Minimum Radius : 0
Maximum Radius : 64.44
Surface 26 : STANDARD
Aperture : Circular Aperture
Minimum Radius : 0

Maximum Radius : 67.99
 Surface 27 : STANDARD
 Aperture : Circular Aperture
 Minimum Radius : 0
 Maximum Radius : 61
 Surface 28 : STANDARD
 Aperture : Circular Aperture
 Minimum Radius : 0
 Maximum Radius : 37.72
 Surface 29 : STANDARD
 Aperture : Circular Aperture
 Minimum Radius : 0
 Maximum Radius : 35.18
 Surface 30 : COORDBRK
 Decenter X : 0
 Decenter Y : 0
 Tilt About X : 0
 Tilt About Y : 0.03163866
 Tilt About Z : 0
 Surface 31 : STANDARD
 Aperture : Circular Aperture
 Minimum Radius : 0
 Maximum Radius : 45.72
 Surface 32 : STANDARD
 Aperture : Circular Aperture
 Minimum Radius : 0
 Maximum Radius : 45.72
 Surface IMA : STANDARD

SOLVE AND VARIABLE DATA:

Thickness of 4 : Variable
 Curvature of 5 : Variable
 Thickness of 5 : Variable
 Curvature of 6 : Solve, chief ray exit angle = 0.04597
 Thickness of 8 : Variable
 Parameter 4 Surf 14: Pickup from 11 times -1.000000
 Thickness of 29 : Variable
 Parameter 4 Surf 30: Variable

INDEX OF REFRACTION DATA:

Surf	Glass	0.550300	0.554300	0.558100	0.561900	0.565500
0		1.00000000	1.00000000	1.00000000	1.00000000	1.00000000
1		1.00000000	1.00000000	1.00000000	1.00000000	1.00000000
2		1.00000000	1.00000000	1.00000000	1.00000000	1.00000000
3	BK7	1.53173100	1.53152963	1.53134209	1.53115812	1.53098703
4		1.00000000	1.00000000	1.00000000	1.00000000	1.00000000
5	BK7	1.51859198	1.51839310	1.51820792	1.51802628	1.51785737
6		1.00000000	1.00000000	1.00000000	1.00000000	1.00000000
7		1.00000000	1.00000000	1.00000000	1.00000000	1.00000000
8		1.00000000	1.00000000	1.00000000	1.00000000	1.00000000
9	MIRROR	1.00000000	1.00000000	1.00000000	1.00000000	1.00000000
10		1.00000000	1.00000000	1.00000000	1.00000000	1.00000000
11		1.00000000	1.00000000	1.00000000	1.00000000	1.00000000
12	MIRROR	1.00000000	1.00000000	1.00000000	1.00000000	1.00000000
13		1.00000000	1.00000000	1.00000000	1.00000000	1.00000000
14		1.00000000	1.00000000	1.00000000	1.00000000	1.00000000
15		1.00000000	1.00000000	1.00000000	1.00000000	1.00000000
16		1.00000000	1.00000000	1.00000000	1.00000000	1.00000000
17	AB	1.51856973	1.51837093	1.51818581	1.51800424	1.51783540
18		1.00000000	1.00000000	1.00000000	1.00000000	1.00000000
19	AB	1.51856973	1.51837093	1.51818581	1.51800424	1.51783540
20	C	1.62920673	1.62877171	1.62836789	1.62797299	1.62760683
21		1.00000000	1.00000000	1.00000000	1.00000000	1.00000000
22	D	1.62020269	1.61992548	1.61966764	1.61941501	1.61918034
23	E	1.58165369	1.58138681	1.58113860	1.58089543	1.58066957
24		1.00000000	1.00000000	1.00000000	1.00000000	1.00000000
25	F	1.62020142	1.61992447	1.61966688	1.61941450	1.61918006
26	G	1.57827411	1.57793217	1.57761453	1.57730369	1.57701527
27		1.00000000	1.00000000	1.00000000	1.00000000	1.00000000
28	H	1.70548133	1.70505899	1.70466659	1.70428253	1.70392614
29		1.00000000	1.00000000	1.00000000	1.00000000	1.00000000
30		1.00000000	1.00000000	1.00000000	1.00000000	1.00000000
31	SILICA	1.45998660	1.45981981	1.45966442	1.45951192	1.45937004
32	VACUUM	0.99978752	0.99978758	0.99978763	0.99978768	0.99978773
33		1.00000000	1.00000000	1.00000000	1.00000000	1.00000000
Surf	Glass	0.569100	0.572400	0.575700	0.578800	

0		1.00000000	1.00000000	1.00000000	1.00000000
1		1.00000000	1.00000000	1.00000000	1.00000000
2		1.00000000	1.00000000	1.00000000	1.00000000
3	BK7	1.53081896	1.53066748	1.53051841	1.53038052
4		1.00000000	1.00000000	1.00000000	1.00000000
5	BK7	1.51769147	1.51754195	1.51739483	1.51725875
6		1.00000000	1.00000000	1.00000000	1.00000000
7		1.00000000	1.00000000	1.00000000	1.00000000
8		1.00000000	1.00000000	1.00000000	1.00000000
9	MIRROR	1.00000000	1.00000000	1.00000000	1.00000000
10		1.00000000	1.00000000	1.00000000	1.00000000
11		1.00000000	1.00000000	1.00000000	1.00000000
12	MIRROR	1.00000000	1.00000000	1.00000000	1.00000000
13		1.00000000	1.00000000	1.00000000	1.00000000
14		1.00000000	1.00000000	1.00000000	1.00000000
15		1.00000000	1.00000000	1.00000000	1.00000000
16		1.00000000	1.00000000	1.00000000	1.00000000
17	AB	1.51766956	1.51752010	1.51737303	1.51723701
18		1.00000000	1.00000000	1.00000000	1.00000000
19	AB	1.51766956	1.51752010	1.51737303	1.51723701
20	C	1.62724818	1.62692584	1.62660946	1.62631755
21		1.00000000	1.00000000	1.00000000	1.00000000
22	D	1.61895008	1.61874278	1.61853900	1.61835069
23	E	1.58044798	1.58024849	1.58005240	1.57987121
24		1.00000000	1.00000000	1.00000000	1.00000000
25	F	1.61895002	1.61874293	1.61853934	1.61835122
26	G	1.57673260	1.57647838	1.57622872	1.57599823
27		1.00000000	1.00000000	1.00000000	1.00000000
28	H	1.70357679	1.70326255	1.70295391	1.70266894
29		1.00000000	1.00000000	1.00000000	1.00000000
30		1.00000000	1.00000000	1.00000000	1.00000000
31	SILICA	1.45923062	1.45910491	1.45898116	1.45886664
32	VACUUM	0.99978778	0.99978783	0.99978787	0.99978791
33		1.00000000	1.00000000	1.00000000	1.00000000

14. REFERENCES

- ¹ D. Vaughnn, *et al.*, The KPNO 4M Fiber Optic Multi-Object Spectrograph, BAAS, Peter B. Boyce, ed., v. 22, p. 887, 1990.
- ² S. C. Barden, *et al.*, "Modifying Hydra for the WIYN telescope - an optimum telescope, fiber MOS combination," in *Instrumentation in Astronomy VIII*, David L. Crawford, Eric R. Craine, Editors, Proc. SPIE 2198, pp. 87-97 (1994).
- ³ D. J. Schroeder, Astronomical Optics, p. 221, Academic Press, Inc., San Diego, 1987.
- ⁴ J. Meaburn, Detection and Spectrometry of Faint Light, p. 246 (Astrophysics and Space Science Library, v. 56), D. Reidel Publishing Company, Dordrecht, 1976.
- ⁵ P. Jacquinot, "The Luminosity of Spectrometers with Prisms, Gratings, or Fabry-Perot Etalons", JOSA, v. 44, n. 10, 1954.
- ⁶ J. Meaburn, *op. cit.*, p. 6.
- ⁷ A. Girard and P. Jacquinot, "Principles of Instrumental Methods in Spectroscopy", Advanced Optical Techniques, A. C. S. Van Heel, p. 78, North-Holland Publishing Co., Amsterdam, 1967.
- ⁸ J. Meaburn, *op. cit.*, pp. 6-8.
- ⁹ G. Walker, Astronomical Observations, an Optical Perspective, pp. 140-141, Cambridge University Press, Cambridge, 1987.
- ¹⁰ A. Girard and P. Jacquinot, *op. cit.*, p. 79.
- ¹¹ J. P. Broadie, *et al.*, "Optimum Choice of Fiber Diameter for Multiple-Object Spectroscopy", The Astronomical Journal, v. 96, pp. 2005-2010, 1988.
- ¹² D. Vaughnn, "What's wrong with the throughput-resolution product? A fiber-fed spectrograph forces a re-evaluation of instrument design parameters" in *Instrumentation in Astronomy VIII*, David L. Crawford, Eric R. Craine, Editors, Proc. SPIE 2198, pp. 34-41 (1994).
- ¹³ *Ibid*, pp. 40-41.
- ¹⁴ T.E. Ingerson, "Assessing the Performance of Argus - CTIO's Multiple Object Spectrometer", *Fiber Optics In Astronomy II*, ASP Conference SERIES, P. M. Gray ed., p. 84 ff., 1993.
- ¹⁵ J. E. Simmons, private communication.
- ¹⁶ S. C. Barden, "Fiber Evaluation for Gemini Design Parameters", 1991.
- ¹⁷ M. Bottema, "Echelle efficiency and blaze characteristics", Periodic Structures, Gratings, Moiré Patterns and Diffraction Phenomenon, SPIE v. 40, pp. 171-172, 1980.
- ¹⁸ D. J. Schroeder, *op. cit.*, pp. 243-249.
- ¹⁹ M. C. Hutley, Diffraction Gratings, pp. 179-213, Academic Press Inc., London, 1982.
- ²⁰ E. G. Loewen (Milton Roy Company, David Richardson Grating Laboratory, Rochester), private communication, July, 1993
- ²¹ W. D. Heacox, "On the Application of Optical-Fiber Image Scramblers to Astronomical Spectroscopy", The Astronomical Journal, v. 92, pp. 222, 1986.

-
- ²² E. Carrasco and I. R. Parry, "A Method for Determining the Focal Ratio Degradation Performance of Optical Fibers", A. S. P. Conference Series, v. 37, Fiber Optics in Astronomy II, ed. P. M. Gray, pp.392-408.
- ²³ S. C. Barden, "Fiber Evaluation for Gemini Design Parameters", 1991.
- ²⁴ D. J. Schroeder, *op. cit.*, p. 162.
- ²⁵ P. R. Yoder, Jr., Opto-Mechanical Systems Design, pp. 145-153, Marcel Dekker, Inc., New York, 1986.
- ²⁶ I. H. Maltison, "Interspecimen Comparison of the Refractive Index of Fused Silica", JOSA, v. 55, n. 10, pp. 1205-1209, 1965.
- ²⁷ B. Edlén, "The Dispersion of Standard Air", JOSA, v. 43, n. 5, pp. 339-344, 1953.
- ²⁸ F. Kohlrausch, Praktische Physik, p. 408, B. G. Teubner, Stuttgart, 1968.
- ²⁹ M. C. Hutley, Diffraction Gratings, p. 22, Academic Press Inc., London, 1982.
- ³⁰ E. Hecht and A. Zajac, Optics, p.352, Addison-Wesley Publishing Company, Inc., Reading, 1974.